UNIVERSITY OF MICHIGAN
MAY 22 1952
ENGINEERING LIBRARY

JOURNAL OF THE AERONAUTICAL SCIENCES

VOLUME 19 MAY, 1952 NUMBER 5

CONTENTS

An Investigation of the Effect of a Varying Tip-Weight Distribution on the Flutter Characteristics of a Straight Wing ..... WILLIAM H. GAYMAN 289

The Effect of Nonlinear Aerodynamic Characteristics on the Dynamic Response to a Sudden Change in Angle of Attack ..... TELFORD W. OSWALD 302

Aerodynamics of Blasts ..... L. TING AND H. F. LUDLOFF 317

The Measurement of Downwash and Sidewash Behind a Rectangular Wing at a Mach Number of 1.6 ..... THEODORE DAVIS 329

Supersonic Wing-Body-Tail Interference ..... GEORGE MORIKAWA 333

Heat Transfer to Constant-Property Laminar Boundary-Layer Flows with Power-Function Free-Stream Velocity and Wall-Temperature Variation ..... SOLOMON LEVY 341

Readers' Forum: "Extension of 'The Dynamic Effects in Rotor Blade Bending,'" by Robert A. Rogers; "Attachment of Rotor Blades by Laminated Elastic Straps," by Kurt H. Hohenemser; "The Shock Strength in a Two-Dimensional Nonsteady Flow," by Lu Ting; "The Reverse-Flow Theorem for Nonstationary Flows," by A. H. Flax; "Comments on 'Aerodynamic Coefficients of an Oscillating Airfoil in Two-Dimensional Subsonic Flow,'" by Henry E. Fettis; "Comments on 'Uniformly Loaded Semi-Infinite Wedge-Shaped Plates,'" by M. L. Williams, Jr.; "The Superposition of High-Intensity Periodic Waves on a Steady Flow," by J. C. Truman and N. J. Lipstein; "Recovery Factors for the Laminar 'Separation' and Stagnation Flows," by S. Levy and R. A. Seban; "Comments on 'Turbulent Boundary-Layer Characteristics . . .,'" by Marvin L. Luther; "Correction for Aspect Ratio of the Indicial Lift Functions of Wagner and Küssner," by R. H. Scanlan; "Design of Nozzles Having Continuous Wall Curvature," by J. C. Crown; "Further Comments on 'The Effect of Surface Cooling on Laminar Boundary-Layer Stability,'" by Martin Bloom 349–359

Published by the

INSTITUTE OF THE AERONAUTICAL SCIENCES, INC.

JOURNAL OF THE AERONAUTICAL SCIENCES

Editor: HUGH L. DRYDEN, *Director, N.A.C.A.*

Associate Editor: ROBERT R. DEXTER *Managing Editor:* BERNEICE H. JARCK

Editorial Committee

Aerodynamics

Francis Clauser
Howard Emmons
Alexander Flax
R. Paul Harrington
R. T. Jones
Carl Kaplan
H. W. Liepmann
C. C. Lin
H. P. Ludloff
Harold Luskin
John R. Markham
Clark B. Millikan
Shatswell Ober
W. Bailey Oswald
Allen E. Puckett
Elliott G. Reid
H. J. F. Reid
Russell Robinson
G. B. Schubauer
W. R. Sears
John Stack
Theodore von Kármán
Richard von Mises

Flight Testing

W. K. Ebel
R. R. Gilruth
Melvin N. Gough
E. G. Stout

Meteorology

C. F. Brooks
D. M. Little
E. J. Minser
F. W. Reichelderfer
H. C. Willett

Structures and Materials

W. B. Bleakney
E. W. Conlon
L. H. Donnell
E. C. Hartmann
N. J. Hoff
Samuel Levy
B. E. Lundquist
J. S. Newell
Alfred S. Niles
W. Ramberg
E. Reissner
F. R. Shanley
H. W. Sibert
C. R. Strang
S. Timoshenko
H. S. Tsien
Chi-Teh Wang

Rotating Wing Aircraft

F. B. Gustafson
K. H. Hohenemser
Bartram Kelley
R. B. Maloy
Ralph McClarren
R. H. Miller
R. H. Prewitt
Igor I. Sikorsky

Physiologic Problems

H. G. Armstrong
Louis H. Bauer
Eugene Du Bois
W. Randolph Lovelace, II
Ross A. MacFarland
A. D. Tuttle

Flight Propulsion

George W. Brady
Frank W. Caldwell
L. S. Hobbs
E. E. Johnson
Joseph Keenan
R. P. Kroon
Hans Reissner
Abe Silverstein
C. Fayette Taylor
E. S. Taylor
P. Taylor
E. S. Thompson
H. S. Tsien

Aircraft Design

W. E. Beall
W. K. Ebel
Hall L. Hibbard
Richard Hutton
C. L. Johnson
A. A. Kartveli
C. J. McCarthy
Fred E. Weick
Robert J. Woods

Air Transport

Charles Froesch
J. A. Herlihy
R. D. Kelly
Otto E. Kirchner
Jerome Lederer
John C. Leslie
R. Dixon Speas

Instruments

Allan C. Binnie
J. R. Bradburn
Charles H. Colvin
C. S. Draper
S. G. Eskin
O. B. Eswal
H. W. Holzapfel
W. L. Howland
George H. Purcell
C. F. Savage
O. Hugo Schuck
C. L. Seward, Jr.
L. D. Statham
R. C. Sylvander
D. K. Warner

Vibration and Flutter

Lee Arnold
M. A. Biot
R. L. Bisplinghoff
William Bollay
Chieh-Chien Chang
I. E. Garrick
Martin Goland
J. P. Den Hartog

Fuels and Oils

D. P. Barnard
J. H. Doolittle
Graham Edgar
R. T. Goodwin
S. D. Heron
A. M. Rothrock

SUBSCRIPTION RATES

JOURNAL OF THE AERONAUTICAL SCIENCES, Published Monthly.—United States and Possessions: 1 Year, $12.00; Single Copies $1.50. Foreign Countries Including Canada (American Currency Rates): 1 Year, $13.00; Single Copies, $1.50.

AERONAUTICAL ENGINEERING REVIEW, Published Monthly.—United States and Possessions: 1 Year, $3.00; Single Copies, $0.50. Foreign Countries Including Canada (American Currency Rates): 1 Year, $3.50; Single Copies, $0.50.

Notices of change of address should be sent to the Institute at least 30 days prior to actual change of address.

Manuscripts for publication, proofs, and all correspondence should be addressed to the Editorial Office of the JOURNAL.

Correspondence regarding subscriptions may be addressed to Publication Office, 20th and Northampton Sts., Easton, Pa., or to the Editorial Office of the JOURNAL OF THE AERONAUTICAL SCIENCES, 2 East 64th Street, New York 21, New York.

Copyright, 1952, by the Institute of the Aeronautical Sciences, Inc.

Entered as Second Class Matter at the Post Office, Easton, Pa., May 1, 1937. Acceptance for mailing at a special rate of Postage provided for in the Act of August 24, 1912. Authorized April 29, 1937.

JOURNAL OF THE AERONAUTICAL SCIENCES

VOLUME 19 MAY, 1952 NUMBER 5

An Investigation of the Effect of a Varying Tip-Weight Distribution on the Flutter Characteristics of a Straight Wing*

WILLIAM H. GAYMAN†

Northrop Aircraft, Inc.

ABSTRACT

Experimental and theoretical investigations into the antisymmetric flutter characteristics of a straight wing having a number of tip-pod mass, size, and shape configurations are summarized. The experimental phase, conducted with a low-speed flutter model of the U.S.A.F.'s Northrop Scorpion F-89 wing, is discussed from the standpoint of a design development study. Model design features, testing techniques, and test results are described, with emphasis on an observed need for considering small variations of mass distribution within a pod having expendable content.

Methods and results of theoretical flutter analyses of several tested pod configurations are discussed. Computations from parallel analyses using different assumptions of pod aerodynamic effectiveness are compared with test data.

It is concluded from these investigations that the aerodynamically effective tip pod may be small in comparison with the pod geometric plan form but, further, that an accurate representation of this effective tip pod may be essential to a successful flutter analysis. It is also indicated that analyses of wing-and-pod configurations having the pod center of gravity on or near the wing elastic axis are more adversely affected by errors in pod aerodynamic representation than are those analyses applying to cases of large pod overbalance.

Received September 5, 1951.

* The investigation described herein is the product of a team effort. Although it is not possible to acknowledge all individual contributions, particular recognition is due personnel of the Aircraft Laboratory, Wright Air Development Center. The basic model was designed and instrumented by L. A. Tolve and R. P. Peloubet and was constructed by F. F. Hense. These and other Aircraft Laboratory personnel, notably W. J. Mykytow, are thanked for their generous cooperation with Northrop personnel during the transition of test operations. Within the Dynamics Section of Northrop Aircraft, Inc., the major part of the theoretical investigation has been carried out by J. K. Latzer, who also has conceived the inverse solution of the flutter determinant as a possible means of establishing the aerodynamic effectiveness of a tip pod from measured flutter data. D. R. Branchflower has made this approach practical from a computational standpoint by a problem formulation amenable to solution by IBM computing facilities. D. T. Egbert has directed the course of much of the theoretical work. Finally, W. E. Cox, in his supervision of all phases of the Northrop-conducted investigations, has given invaluable aid through his many suggestions and his encouragement.

† Dynamics Engineer.

NOTATION

M = wing-element weight, lbs.
S_α = wing-element unbalance about wing elastic axis, in. lbs.
I_α = wing-element moment of inertia about wing elastic axis, lb. in.^{2}
M_T = tip-pod weight, lbs.
S_{α_T} = tip-pod unbalance about wing elastic axis, in.lbs.
I_{α_T} = tip-pod moment of inertia about wing elastic axis, lb. in.^{2}
EI = wing flexural rigidity, lb. in.^{2}
GJ = wing torsional rigidity, lb. in.^{2}
ω_h = frequency of first antisymmetric uncoupled bending mode, cycles per min.
ω_α = frequency of first antisymmetric uncoupled torsion mode, cycles per min.
ω_1, ω_2 = frequencies of first two antisymmetric coupled modes
θ = normalized wing deflection in the rolling degree of freedom
h = normalized wing deflection in the first antisymmetric uncoupled bending mode
h_r = a reference h
α, α_1 = normalized wing deflection in the first antisymmetric uncoupled torsion mode
α_2 = normalized wing deflection in the second antisymmetric uncoupled torsion mode
g = flutter-mode damping coefficient
ω_f = flutter frequency, cycles per min.
v_f = critical flutter speed, m.p.h.
b = wing semichord, in.
b_T = tip-pod semichord, in.
s_T = tip-pod span, in.
$[(1/2)+a]$ = location of the wing elastic axis measured from the lifting-surface quarter-chord, as a fraction of the local semichord; positive when aft of the quarter-chord

Introduction

Theoretical flutter analyses of wings carrying tip pods have not been consistently successful in giving reliable predictions of flutter speed. A few cases are known wherein, contrary to expectations based on analyses, aircraft with tip fuel tanks have experienced wing flutter. More numerous instances are known of disagreement between results of analysis and of flutter-model tests, in which the incidence of flutter has been observed much more often than in flight.

The inadequacy of analytical treatment is believed to lie primarily in the absence of a rational accounting for the aerodynamic forces on a tip pod oscillating in translation and in pitch. Furthermore, in the case of tip tanks, the effective pitching moment of inertia of the fuel at the flutter condition is not predictable to the degree of accuracy that may be demanded in a given situation. Indeed, it is in recognition of these and other related limitations in the flutter analysis of wings with tip pods that the Aircraft Research and Testing Committee of the Aircraft Industries Association is favoring a research program aimed at meeting the specific needs of the problem.

Some of the spade work has already been done by various investigators. The N.A.C.A., for example, has conducted both theoretical and experimental investigations into the flutter characteristics of straight uniform cantilevered wings having variable placement of a concentrated mass. However, it is not attempted here to review the progress in this particular field, nor is it attempted to assess the relation between other investigations and that of the subject discussion.

About a year ago the Dynamics Branch of the Wright Air Development Center's Aircraft Laboratory initiated a series of wind-tunnel tests of a flutter model of the F-89 wing, which has an integral tip fuel pod. Several months later Northrop Aircraft acquired the model for use in a tip-pod design development study. To date about 300 pod mass configurations have been tested among six tip pods differing in size and shape. The purpose of this paper is to summarize the salient features and results of these test programs and to report on the progress of a complementary analytical approach to this flutter problem.

Scope of the Investigation

The flutter-model test programs described herein were begun by the W.A.D.C. with a specific objective of determining the flutter safety of an existing wing-aileron design. This program was extended by the W.A.D.C. to include preliminary series of tests of tip-pod installations. These tests, and other tip-pod investigations subsequently conducted by Northrop Aircraft, have had a similar motivation, with the result that the entire experimental phase has assumed the aspect of a design development study rather than a research program.

This philosophy of approach is emphasized because of its dominant influence on flutter-model construction, on the establishment of test configurations, and, for reasons to be discussed presently, on the quest for acceptable methods of theoretical analysis.

At the outset it was considered that preliminary confirmation of the flutter safety of specific wing-and-pod design configurations should rest entirely on model tests, with final confirmation of the safety of any chosen configuration depending on flight flutter testing judiciously based on model experience. Therefore, the basic requirements to be met in a flutter-model test program so directed are as follows: (1) attainment of dynamic similarity between the model and its prototype and (2) coverage of critical weight configurations of wing and tip pod.

In general, the critical weight régimes cannot be foreordained. Therefore the test objectives, shifting as the program progresses, may pursue such a chronological course as follows:

(1) The initial objective is the definition of flutter characteristics as functions of specific wing-and-pod weight configurations that follow the expendable-load sequencing to be preferred from aircraft design and operational considerations.

(2) In the event that an unsafe flutter condition is indicated by the foregoing, avoidance of major design changes might be sought by any of the following expedients: (a) repetition of (1) with alternate usage sequences that are feasible from a design standpoint and, at the same time, that do not penalize the operational utility of the aircraft; or (b) investigation of the effects of incorporating ballast weights in the pod; or (c) imposition of tentative aircraft operational restrictions, to be evaluated by subsequent flight flutter testing, provided that such limitations, again, constitute no serious sacrifice to the operational utility.

(3) If none of the alternatives of (2) is acceptable from a design or a flutter standpoint, further testing may be directed toward examination of more drastic remedial measures, such as a change in the pod-wing geometric configuration, addition of pod fins, relocation of pod fuel bulkheads, added or revised fuel compartmentization within the pod, or elastic mounting of the pod on the wing tip.

The experimental investigations to be described have pursued this chain of objectives to the extent required with each of several proposed design configurations. However, certain limitations in the scope of the tests have been imposed by the practical considerations of model design and of available test facilities. These considerations have dictated the choice of a low-speed flutter model, leaving the evaluation of high Mach Number effects on flutter characteristics to a delicate blend of theory, experience, and judgment. Moreover, use of a single model in constant-density wind tunnels has precluded investigation of altitude as a flutter

parameter. Therefore the test results apply directly to only a subsonic sea-level environment.

The Experimental Investigation

Description of the Flutter Model

Wing.—The design criteria for attainment of dynamic similarity between a low-speed flutter model and its equivalent prototype are rather basic and therefore are not restated here. It is noted, however, that in the design of the F-89 wing flutter model, scale factors applying to geometry and to air speed were selected by the W.A.D.C. to permit use of the 5-Ft. Wind Tunnel at Wright Field. These choices fixed the relationship between the frequencies of corresponding oscillation modes of model and prototype. Attainment of the frequency scale factor was sought by appropriate reductions of airplane-wing mass and rigidity distributions.

The F-89 wing flutter model is a semiwing, designed for vertical support from a faired structure that may be mounted against the ceiling of a wind-tunnel working section, as shown in Fig. 1. The wing root is attached to a hinged plate provided with a locking arrangement such that, optionally, the wing may be cantilevered or may be freed in roll. This provision permits investigation of both symmetric and antisymmetric flutter characteristics, although it excludes from the former those contributions by the rigid-body symmetric modes of translation and pitch that exist in free flight. For the antisymmetric case, however, free-flight simulation is adequate, inasmuch as the rolling frequency of the wing, as a pendulous rigid body, is much lower than the frequency of the first elastic mode.

The basic model semiwing consists of nine balsa-and-fabric-covered skeletal wooden sections, each independently attached at its bounding ribs, to an aluminum-alloy spar. The covering between the closely spaced ribs of adjacent sections has been cut around the entire

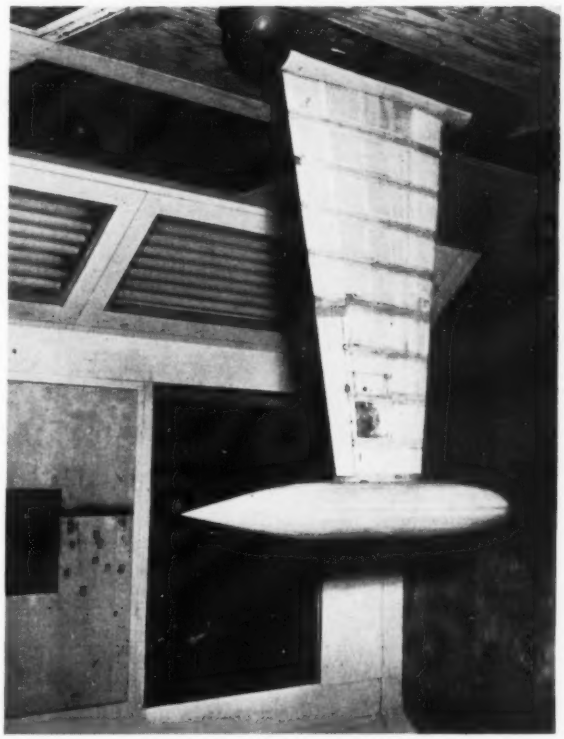

Fig. 1. Installation of flutter model in Convair Wind Tunnel.

airfoil, and the resulting gaps are sealed by thin latex strips. This type of construction has been used to minimize contributions of the wooden sections to the flexural and torsional rigidity distributions of the assembled wing. Thereby, the structural design of the wing was simplified considerably; the centerline of the spar was located to approximate the elastic axis location of the prototype wing, and the spar was designed to provide nearly all of the required rigidity. The W.A.D.C. conducted static tests on the assembled wing in order to

Table 1
Model-Wing Data

(a) Geometric:

Semispan (less tip pod)	:	35.3 in.
Aspect ratio	:	4.43
Taper ratio	:	0.51
Airfoil	:	NACA 0009-64
Sweepback of 30 per cent chord	:	0°

(b) Inertial and Structural:

Wing Section: Number	Wing Section: Midspan station	M (Lbs.)	S_α (In.Lbs.)	I_α (Lb. In.²)	$EI \times 10^{-5}$ (Lb. In.²)	$GJ \times 10^{-5}$ (Lb. In.²)
1	2.0	0.679	0.872	10.3	0.98	0.98
2	6.0	1.482	2.038	27.9	0.98	0.98
3	10.0	1.511	1.332	18.4	0.98	0.98
4	14.0	1.642	2.198	14.9	0.90	0.89
5	18.0	1.484	1.922	21.1	0.76	0.77
6	22.0	1.217	1.773	14.9	0.61	0.59
7	26.0	1.268	1.930	14.5	0.40	0.40
8	30.0	1.022	1.192	9.1	0.23	0.22
9	33.7	0.377	0.433	3.7	0.11	0.08
		10.682	13.690	134.8		

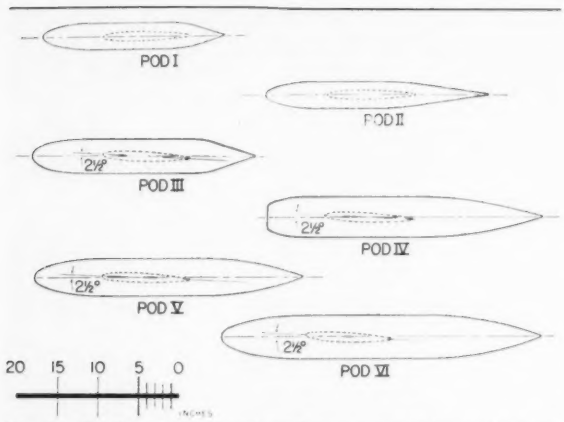

FIG. 2. Profiles of tested pod configurations relative to the wing tip chord.

indicate any final adjustments needed to realize adequate representation of design *EI* and *GJ* distributions.

Each of the nine wing sections was ballasted with lead weights in a manner to simulate a lumped distribution of prototype-wing weight, static unbalance about the elastic axis, and moment of inertia about the elastic axis. The mass parameters of each section were determined experimentally prior to wing assembly in order to assure reasonable agreement with design values.

Geometric, inertial, and structural data applying to the model wing are given in Table 1. The mass distribution shown corresponds to a condition with full wing fuel tanks; other distributions, not listed, were also used.

The model was fitted with an aileron, which was locked in its neutral position during the subject series of tests.

Tip Pods.—The geometric configurations of the tested tip pods are shown in relation to the tip wing section in Fig. 2. Pods V and VI were also tested in slightly forward positions, the displacements being about 13 per cent tip chord ahead of the positions shown.

Pod construction details were dictated by a consideration of test loading schedules simulating fuel usage. Several problems were presented. First, in a partially filled tank of an aircraft in flight, the instantaneous disposition of fuel is determined by a time history of airplane attitude and acceleration. Even if the dynamic effects of fuel sloshing are to be excluded from a flutter investigation, there still remain an infinite number of instantaneous configurations, several régimes of which may be of concern from a flutter standpoint. Therefore, it was sought to simulate a practical number of discrete configurations representing a liberal sampling of those possible.

The next problem was concerned with the means of such simulation. General use of a liquid was precluded by intolerable complications in model construction, inasmuch as the wind-tunnel working section could not be rotated in the gravity field. For example, use of a variable quantity of liquid in the nose or in the tail of a tip tank would require a rather elaborate system of bulkheads that were changeable during the course of the tests. Thus, as a general expedient, approximations of desired fuel conditions were effected by use of suitably disposed lead slugs that, in all but one of the pods so loaded, had centroidal pitching moments of inertia representing solid or "frozen" fuel.

Use of frozen fuel in flutter tests introduces errors that are not amenable to theoretical analysis. However, on the assumption that tip-pod-fuel sloshing frequencies will generally be far below any flutter frequency, the existence of a significant time-varying fuel inertia can be dismissed, together with the added degree of freedom of fuel motion. Therefore, the frozen-fuel errors may be assessed qualitatively as a conservative omission of energy dissipation within the pod and, of potentially greater importance, as an improper representation of pod moment of inertia. No general criteria have been evolved for determining whether such representation is conservative or unconservative from a flutter standpoint. However, in the correlation of data obtained in the subject tests, it has generally been possible to indicate whether the use of liquid fuel would raise or lower the flutter speed observed with frozen fuel. Such indications are predicated on a neglect of added damping and on a reduction of pod pitching moment of inertia. The order of magnitude of the reduction is bracketed by pod inertia values calculated on the extreme bases of solid fuel and of zero centroidal moment of inertia of the fuel within any one compartment.

Pods I and II represent airplane tip pods having single-compartment fuel tanks. For these tank shapes, errors accruing from the frozen fuel assumption may be expected to be large. In order to permit a direct evaluation of these errors as applying to a particular type of fuel disposition, the W.A.D.C. constructed a thin fiberglas model of Pod I having internal bulkheads corresponding with those of the prototype fuel tank. A liquid having the proper specific gravity was used for the loading medium. Pod II was made by attaching a paper tail cone to Pod I and ballasting as required to meet the "empty-pod" condition.

Model pods of each configuration, except that of Pod II, were made of balsa hollowed out and fitted with provisions for attaching the lead weights intended to simulate expendable load. For each pod, design mass parameters—weight, c.g. location, and centroidal pitching moment of inertia—were calculated for all chosen test configurations, and the pod ballasting arrangement was effected accordingly. Actual mass parameters of a representative number of pod configurations were determined experimentally to ascertain reasonable agreement with design values. Table 2 lists the model-pod

TABLE 2
Tip-Pod Mass Parameters for "Empty" and "Full" Conditions

Pod Designation	"Empty" Condition M_T (lbs.)	"Empty" Condition Sa_T (in.lbs.)	"Empty" Condition Ia_T (lb. in.²)	"Full" Condition M_T (lbs.)	"Full" Condition Sa_T (in.lbs.)	"Full" Condition Ia_T (lb. in.²)
I	0.261	−0.211	7.35	3.364	−2.677	69.77
II	0.457	0.765	13.67	3.560	−1.701	**
III	1.189	−2.154	37.62	5.285	−2.166	144.5
IV	1.825	−2.353	68.83	6.384	0.983	219.7
V (aft position)	1.835	−4.244	71.60	6.412	−2.113	230.7
(forward position)	1.835	−6.630	85.74	6.412	−10.45	247.0
VI (aft position)	2.495	−6.509	128.1	7.072	−6.028	316.3
(forward position)	2.495	−10.25	153.2	7.072	−16.67	350.5

** The moment of inertia of Pod II, filled with a liquid, was not measured.

mass parameters corresponding to "empty" and "full" conditions.

Pod attachment to the wing was made by three machine screws, one entering a tapped hole in the end of the spar and the other two engaging plate nuts at forward and aft locations on the tip rib. Pillow blocks placed between the pod and the rib served to stiffen the mounting in roll. Quantitative representation of the rigidity of the prototype pod attachment was not attempted; it was merely noted that such mounting would be sufficiently rigid to obviate the need of the added degree of freedom of pod motion relative to the wing tip.

Pods III through VI represent pod designs having several fuel compartments, and, therefore, frozen fuel errors could be shown to be less important than those applying to Pods I and II; the importance is governed to some extent by fuel sequencing.

The simulation of fuel in one of the tested pods was based on measured moments of inertia of a model cell containing water. This cell was a right cylinder with length equal to radius and with the rest position of its axis horizontal. Moments of inertia of the cell in several conditions between empty and full were measured about a horizontal centroidal diameter of the cell by the method of timed oscillations. The test results, as applying to the water only, are shown nondimensionally in Fig. 3 as the ratio of water I_c to the calculated I_c of a solid having the same density and the same volume disposition as the water.

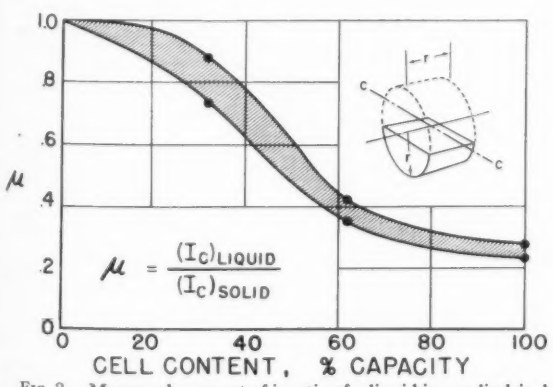

FIG. 3. Measured moment of inertia of a liquid in a cylindrical cell as a fraction of the moment of inertia of a solid having the same density and volume disposition.

These model tests are mentioned not for emphasis of a particular engineering result, but rather, because it is believed that such testing may be a generally useful means of determining effective moments of inertia of oscillating fuel tanks as functions of shape, frequency, and, perhaps, amplitude. Some question logically may be raised about scale effects, which are certainly subject to investigation. However, from the limited experiences obtained in the subject programs, it is anticipated that useful results may be had from model tests conducted with oscillation amplitudes sufficiently small to prevent sloshing.

Instrumentation and Test Techniques

The dynamic testing of the model was conducted in two phases: (1) vibration tests, to determine frequencies and node lines of the lowest natural modes of vibration in still air, and (2) wind-tunnel flutter tests, to determine flutter frequency, flutter speed, and mode damping as a function of air speed.

For the majority of the tests the wing instrumentation was simple. The outputs of two d.c. strain-gage bridges were fed through Brush amplifiers into a two-channel Brush recorder. The strain gages were located on the wing spar near the midspan of Wing Section 1. One two-gage bridge had gage placement selectively sensitive to spar bending; the other bridge, using four gages, was made responsive to spar torsion.

For the vibration tests excitation was provided by a motor-driven variable-speed mechanical oscillator attached to the model tip pod by a small elastic cord. Frequencies of coupled modes were obtained from the Brush recordings. Node lines were located by the sense of touch or by visual observation of relative amplitudes.

The wind-tunnel test phase involved relatively simple procedures. In testing each model configuration, the tunnel speed was increased in increments. During speed changes and at stabilized air speeds, small wires attached to the tip rib and extending through the tunnel wall were jerked manually to excite a transient response. The character of the damping indicated on the Brush tape served as a guide in estimating the proximity

TABLE 3
Geometric Shape Effects on Flutter Characteristics (Wing Free to Roll)

Pod Designation	Measured Pod Parameters M_T (lbs.)	Sa_T (in.lbs.)	Ia_T (lb. in.²)	Flutter Speed v_f (M.P.H.)	Flutter Frequency ω_f (Cycles per Min.)
III	3.441	−4.447	125.4	160	580
V (aft position)	3.477	−4.369	124.5	156	594
V (forward position)	3.469	−4.352	124.3	154	591
III	3.134	−6.255	114.5	143	624
V (aft position)	3.157	−6.256	111.1	139	630
V (forward position)	3.151	−6.280	112.5	141	628

NOTE: A wing weight distribution somewhat different from that shown in Table 1 was used in these tests.

to flutter and, hence, the magnitude of the succeeding speed increment.

The establishment of the critical flutter speed was inclined to be somewhat arbitrary, the sharpness of resolution varying with different pod loading conditions. This is, of course, to be expected, since flutter is qualitatively described in categories between "mild" and "explosive," these adjectives relating to the slope of the damping-air-speed curve in the region of marginal stability. With some of the tested configurations the tunnel speed could be varied over a 10-m.p.h. range with no appreciable change in flutter amplitude. With a few other configurations, a 1-m.p.h. air-speed increment produced a definite transition from stable to divergent oscillation. Whenever instability occurred, the control wires were tightened in an attempt to limit flutter amplitude while the tunnel speed was being reduced.

Generally, vibration tests of only a few of the preselected configurations were run prior to tunnel testing, inasmuch as the test program was continually subject to change. However, after each tunnel test program, natural mode data were measured with all model arrangements for which flutter data had been obtained. Thus the repetition of certain of these vibration tests served to indicate whether the model had suffered structural damage in any of the more violent cases of flutter.

Initial tests of Pods I and III were conducted in the 5-Ft. Wind Tunnel at Wright Field. All subsequent flutter tests were conducted in the Convair Wind Tunnel at San Diego. For the majority of the tests, the limiting air speed of interest was arbitrarily placed at 165 m.p.h.

Observations made during the earlier tests indicated that the lowest flutter speeds were to be expected with antisymmetric flutter modes. For this reason most of the subsequent testing was conducted with the wing free to roll. Limited testing with the wing cantilevered was programmed on the general observance that symmetric flutter had occurred with only certain of those tested pod configurations that had centers of gravity aft of the wing elastic axis. In these few cases flutter speeds were only slightly below the preselected maximum test speed. Consequently, the test results considered to be of greatest interest are those pertaining to antisymmetric flutter modes.

Test Results

No attempt is made herein to present a systematic review and interpretation of all test data. Rather, chosen results illustrating types of flutter behavior are offered primarily to emphasize a general need for thorough consideration of the quantity and the disposition of the expendable content within a tip pod.

Several tests were conducted to explore the efficacy of pod ballast weights in improving a marginal flutter situation. These tests give direct evidence of the potential sensitivity of flutter speed to minute changes in pod loading. Arbitrarily, a particular loading condition of Pod IV—one with which the observed flutter speed was 138 m.p.h.—was taken as the reference configuration. A weight equal to 1 per cent of this pod weight was located successively at different positions along the axis of the pod, and the flutter speeds corresponding thereto were noted to range between 134 m.p.h. and a speed above 165 m.p.h., as shown in Fig. 4.

Adherence to the objectives of the test programs precluded a systematic isolation of pod aerodynamic effects from the effects of mass distribution. However, four special tests were made as follows: Pod V, in each of its two positions on the wing, was loaded to reproduce the mass parameters of two arbitrarily chosen test configurations of Pod III, and flutter data were ob-

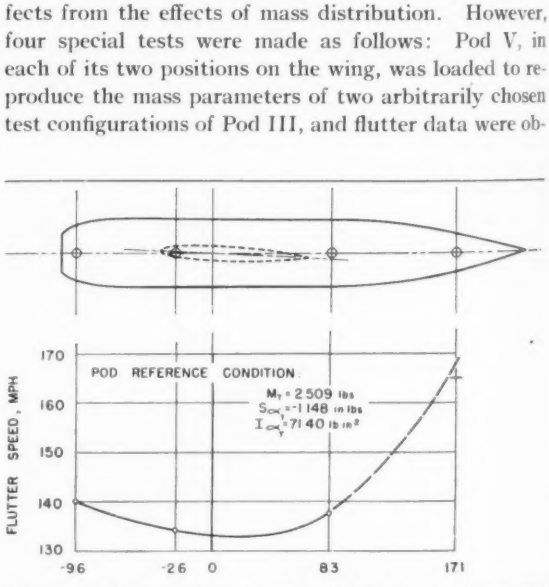

FIG. 4. Variation of flutter speed with location of a small movable weight in Tip Pod IV.

TABLE 4
Tip Pod IV Mass Parameters for Conditions Represented in Fig. 6

Test Number	Nominal Fuel Content, (Per Cent Capacity)	M_T (Lbs.)	Sa_T (In.Lbs.)	Ia_T (Lb. In.^{2})
9	0	1.825	−2.353	68.83
62	11	2.167	−1.845	69.93
61	22	2.509	−1.148	71.40
60	33	2.850	−0.189	74.16
59	44	3.192	1.054	78.74
57	56	3.533	2.570	85.53
56	67	3.874	4.352	94.89

NOTE: The wing mass parameters are given in Table 1.

tained for each condition. The test results, given in Table 3, show that the changes in pod geometry relative to the wing had small effects on flutter characteristics, the largest differences shown being only slightly greater than limits of test accuracy. While no general opinions can be based on these limited data, the results support the tentative conclusion of Sewall and Woolston[1] that changes in pod aerodynamic shape have little effect on flutter characteristics.

An unwanted by-product of the design-development type of approach pursued in the subject tests has proved to be a complication in correlation and interpretation of test data. Typically, a change in pod loading was accompanied by changes in all three pod mass parameters, masking a clear-cut relationship between cause and effect. For example, in interpreting the results of a series of tests involving changes only in pod loading, it was sought to correlate observed flutter speeds with the three independent variables, M_T, S_{a_T}, and I_{a_T}. Four-dimensional plots proved to be too bewildering to assimilate, even with the aid of notes and color coding. A three-dimensional plot using a contour representation of flutter speed in a planar coordinate system having I_{a_T}/S_{a_T} and S_{a_T}/M_T axes has not inspired confidence in either its applicability or its utility because of its resemblance to a topographical map of extremely rugged terrain. Had a research approach been used in these investigations, the trends in flutter behavior might have been made more apparent by the systematic control of one variable at a time. Even so, from the unproductive attempts at cross-correlation of data applying to each of several pods, it is contended that useful empirical flutter-speed relationships cannot be expressed in terms of pod mass parameters only and that insight into the theoretical aspects of the problem is needed to evolve suitable correlation bases.

This contention is supported by several cases of apparent discontinuity in flutter behavior. A case of this type was observed in the testing of Pod IV. For the purpose at hand it is sufficient to represent this pod as one containing two fuel compartments having a common bulkhead just aft of the wing elastic axis. One of the fuel sequencing programs of interest involved an empty forward compartment and various amounts of fuel disposed against the forward bulkhead of the aft compartment, such as would exist in an unaccelerated vertical dive. The pod mass parameters applying to this sequencing are given in Table 4. Fig. 5 shows the variation of observed flutter speed with aft-compartment fuel content. An abrupt reduction from a flutter speed above 165 to 99 m.p.h. accompanied a decrease from 67 to 56 per cent of tank capacity. Violent flutter occurred in the testing of the 56 per cent fuel condition because of an inadvertent overshooting of the flutter speed by 11 m.p.h.

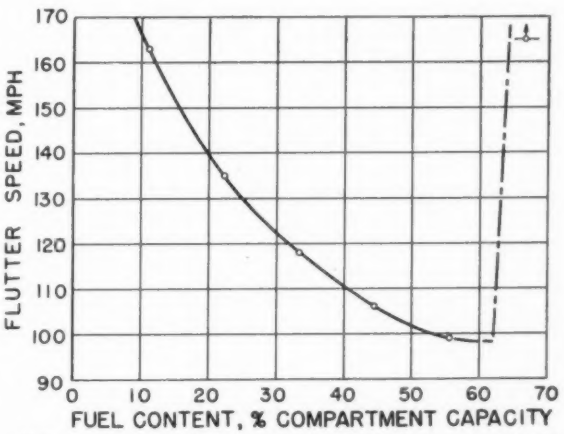

FIG. 5. Variation of flutter speed with the fuel content in the forward end of the aft fuel compartment of Pod IV; forward compartment empty.

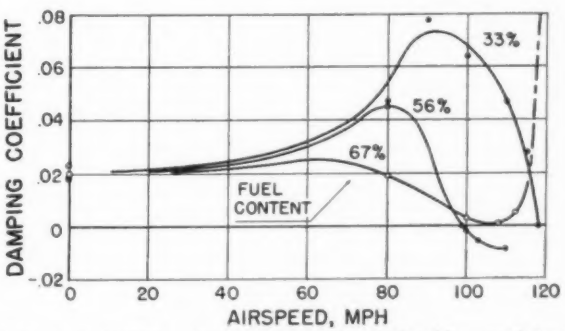

FIG. 6. Measured damping-air-speed relationships applying to several of the tested configurations represented in Fig. 5.

TABLE 5
Data Applying to Illustrative Test Conditions of Tip Pod IV

	Test No. 40	Test No. 62
M_T (lbs.)	5.019	2.167
Sa_T (in.lbs.)	−7.764	−1.845
I_{α_T} (lb. in.^{2})	162.4	69.93
ω_1 (cycles per min.)	510	675
ω_2 (cycles per min.)	670	830
ω_h (cycles per min.)	615	717
ω_α (cycles per min.)	536	765
v_f (m.p.h.)	158	163
ω_f (cycles per min.)	568	700

NOTE: The wing mass parameters are given in Table 1.

The damping records of three of the tests in this series have been analyzed. The results, plotted against air speed, are shown in Fig. 6, wherein the damping coefficient, g, is the measured logarithmic decrement divided by π. While some liberties have been taken in fairing curves through the test points, there nevertheless appears to be a family of curves having similar characteristics. In particular, the curves applying to the 56 and 67 per cent configurations show the same type of slope reversal in the region of small damping, and, in the sense of tendency to flutter, the differences in behavior can hardly be called discontinuous. However, since flutter stability is not regarded in a qualitative sense, a true point of discontinuity exists at that pod weight configuration having its damping curve tangent to the air-speed axis.

THE THEORETICAL INVESTIGATION

A theoretical investigation, complementary to the experimental investigation, has been directed toward evolving a method of flutter analysis applicable to wing-and-pod configurations similar to the F-89 flutter model. The criteria of acceptability are considered to be the practicability of examining a relatively large number of pod weight conditions and, of course, the reliability of flutter prediction.

This investigation is not completed as of this writing. Moreover, the results obtained to date are not sufficiently conclusive to establish the validity of the chosen approach. For this reason a formal mathematical presentation is deleted from this discussion, and, in its place, a qualitative summary of the studies is given with emphasis on correlations between results and assumptions.

The chosen method of analysis is conventional, conforming in all major respects with the three-dimensional treatment set forth by Smilg and Wasserman.[2] Only the antisymmetric case is examined. The analyses are based on uncoupled modes of vibration in bending and in torsion. It has been assumed that three properly chosen degrees of freedom are sufficient to determine the two lowest modes of free vibration, as well as any flutter mode of interest. These degrees of freedom are taken as follows:

θ: a zero-frequency, rigid-body rolling mode
h: the first uncoupled antisymmetric bending mode
α: the first uncoupled antisymmetric torsion mode

A few exploratory analyses have also been made with the added degree of freedom of the second torsional mode.

The discussion is presented in two parts. (1) the free vibration analyses and (2) the flutter analyses. Illustrations are focused on the analyses of two tested configurations of the model wing with Pod IV attached. These conditions are selected to represent considerably different régimes of pod mass parameters; data pertaining thereto are given in Table 5.

The Free-Vibration Analyses

Free-vibration analyses are made prior to flutter analyses to assure compatibility between uncoupled-mode representation and measured coupled-mode data. The uncoupled modes are defined in terms of frequencies and normalized mode shapes, which are established as follows:

Uncoupled-Mode Shapes.—The θ mode is represented by a wing rolling displacement giving unit deflection at the tip-pod centerline.

The α mode shapes applying to various wing-and-pod configurations may be obtained by independent Holzer analyses of each. However, in all analyses dealing with Pod IV, a reduction in labor has been effected by the general adoption of the particular shape calculated for the case of a mean moment of inertia of this pod. The justification of this approximation is supported by Holzer analyses of the cases with extreme pod inertias; the normalized α mode shapes do not change appreciably as I_{α_T} is varied from a mean value to either extreme.

The h and α modes are orthogonal by definition. The h mode is defined so as to be orthogonal with the θ mode. This definition is effected by approximations that permit relatively simple accounting for the change in tip-pod mass. Specifically, for a particular wing mass distribution containing a preselected reference tip mass, the normalized mode shape of the first antisymmetric bending mode is obtained as a reference mode shape, h_r, by any of the conventional iteration procedures using mass and rigidity distributions. Thereafter, with any other tip mass, the normalized mode shape is approximated by a linear combination of the h_r and θ modes in a manner to satisfy the orthogonality condition. As evidenced by special studies, this technique gives good agreement between approximate and exact mode shapes, particularly if the reference tip mass is about midway between the extremes to be considered with a given tip pod.

Fig. 7 shows the uncoupled-mode shapes used in analyses of Pod IV Test Conditions 40 and 62.

Uncoupled-Mode Frequencies.—Uncoupled-mode frequencies are obtained from a free-vibration analysis

using measured coupled frequencies and model mass parameters. This analysis gives a frequency equation containing ω_h^2, ω_α^2, and terms defining the inertia coupling between the h and α modes and the α and θ modes. This equation (a quadratic in ω^2) is solved for, say, ω_α^2 in terms of these same inertia coupling parameters and the roots, ω_1, and ω_2, measured in vibration tests. The solution yields two roots for ω_α^2. The ambiguity of which of these roots applies is eliminated statistically in the following manner: For each of a number of the tested configurations, both roots are used in calculating the effective torsional stiffness of the wing in the α mode. Examination of all of these stiffness values shows that half, represented by one from each test condition, are closely grouped, whereas the other half differ widely. The effective torsional stiffness is also obtainable from wing GJ and α distributions; therefore, if the use of a single α representation is accepted, this stiffness may be considered as a physical constant of the wing. Thus it is apparent that the small spread of the better grouped set of stiffness values obtained from the coupled-mode analyses is attributable to errors in measured coupled frequencies and mass parameters, to the adoption of an average α mode shape in place of the exact shape, and to neglected coupling with higher vibration modes. The cumulative errors from these sources are considered to be smaller than those incident to static measurements of torsional rigidity, and, hence, the coupled-mode approach to the determination of uncoupled frequencies is preferred. This preference follows from the belief that, in the subject application, at least, errors in frequency are more likely to have adverse effects on the flutter analyses than are errors in mode shape when both frequency and mode shape are determined by, say, a Holzer analysis using a measured GJ distribution.

The technique of stiffness calculation by coupled-mode analysis not only provides a basis for determining which of the roots of ω_α^2 applies to any one test configuration but also affords a means of spotting erroneous or inconsistent data applying to any configuration. In practice, an average torsional stiffness has been used in the determination of the ω_α value for each test condition. The uncoupled bending frequency, ω_h, is calculable as soon as ω_α is established.

This procedure has been followed with 30 of the tested conditions of Pod IV. The computing labor entailed has been kept relatively small by suitable tabular setup. Average stiffnesses in bending, as well as in torsion, have been used in the calculation of uncoupled frequencies.

Prior to flutter analysis, the adequacy of the treatment thus far is judged by the correspondence of calculated and measured node line locations in each of the coupled modes. Fig. 8 and Fig. 9 show the node-line plots for Test Conditions 40 and 62, respectively. In both cases the agreement is considered sufficiently close

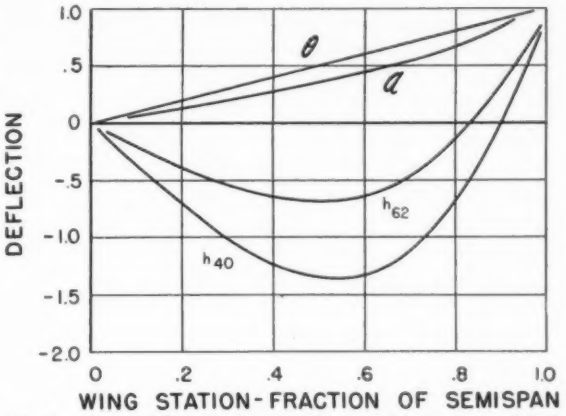

FIG. 7. Uncoupled-mode shapes, θ, h, α, used in analyses of Pod IV Test Conditions 40 and 62.

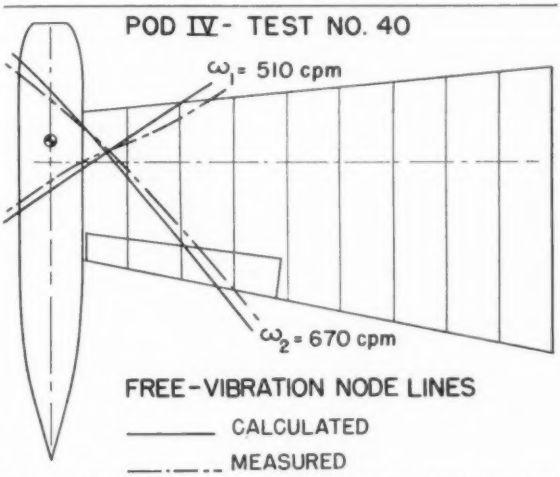

FIG. 8. Measured and calculated node-line locations, first coupled vibration modes of Test Condition 40.

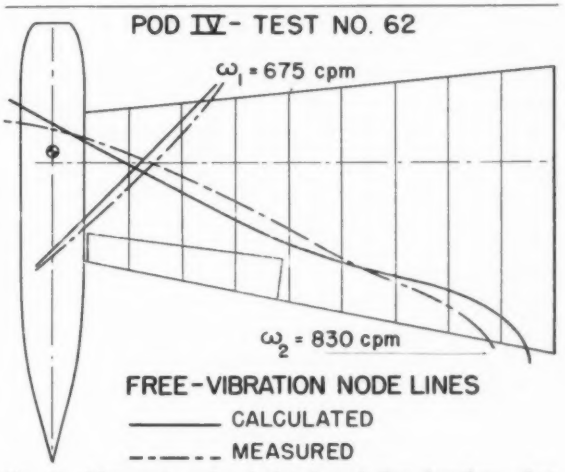

Fig. 9. Measured and calculated node-line locations, first coupled vibration modes of Test Condition 62.

to warrant confidence in the assumptions and the techniques of the free-vibration analyses.

The Flutter Analyses

The formulation of modal aerodynamic energies accounts for the effects of wing taper with the method recommended by Smilg and Wasserman. That is, a reference semichord is chosen, and the aerodynamic coefficients applying to tapered airfoils are used in the appropriate aerodynamic integrals. The contributions of wing and tip pod are evaluated independently and are subsequently combined in the flutter determinant.

The aerodynamic effects of an oscillating tip pod are not accounted for in available flutter theory. Therefore, as an expedient to permit the application of existing theory, it is sought to replace the tip pod with its flat-plate "aerodynamic equivalent." The term "aerodynamic equivalent" is defined herein as a rectangular wing extension having a semichord, a span extent, and a quarter-chord location relative to the wing elastic axis which give the same aerodynamic effect under analysis by the method of reference (2) as does the actual pod under wind-tunnel test conditions. It must be granted that pod effects may not be confined within the pod span but may extend over the outboard portion of the wing; a significant end-plate effect may exist in the oscillating case, as well as in the stationary case. At the same time, it is considered that the presence of the tip pod may strengthen the validity of the treatment accorded the wing, inasmuch as the method of reference (2) makes no rational provision for finite aspect-ratio effects.

The aerodynamic coefficients contained in reference (2) are given as functions of $v/b\omega$. Since all parts of the wing are operating at the same air speed and flutter-mode frequency, the coefficients applying to the aerodynamically equivalent tip pod are made compatible with those applying to the wing by use of $v/b\omega$ values consistent with the relation between pod semichord and wing reference semichord. It follows that the relationships between the moduli and the phase angles of the aerodynamic vectors associated with the pod and with the wing are sensitive to the choice of pod semichord.

One method of determining the parameters of the tip-pod aerodynamic equivalent is the method of direct substitution. That is, the semichord, the span, and the quarter-chord location are arbitrarily chosen, and flutter analyses are made in the conventional manner. A failure of this tip representation to give acceptable determination of flutter characteristics demands the choice of a new set of parameters and a repetition of the analyses. In principle, this process is repeated until a unique pod configuration is found to give reasonable correspondence between calculated and observed flutter behavior in each of the examined test cases.

TABLE 6
Assumed Flat-Plate Aerodynamic Equivalents of Tip Pod IV
(Pod Diameter at Maximum Section: 4.73 In.)

Case	Semichord b_T (In.)	Span s_T (In.)	Quarter-Chord Location $b_T[(1/2)+a]$ (In. Forward Elastic Axis)
1	5.5	4.73	0.88
2	16.5	2.77	6.33
3	16.5	3.60	0
4	5.5	4.73	6.33
5	8.7	3.00	6.27
6	5.5	4.73	3.63

This approach was adopted in preliminary flutter analysis directed at establishing the sensitivity of calculated flutter characteristics to the choice of widely different pod plan-form arrangements. Successively, six different aerodynamic equivalents were assumed to apply to Pod IV. The geometries of these tip cases are given in Table 6. Case 1 is merely an extension of the wing tip chord over the span of the pod. Case 2 is synthesized from estimates of the force and moment coefficients applying in the nonoscillatory condition. Case 3 is a modification of Case 2 in the sense that a fictitious horizontal fin is added to move the center of pressure aft to the wing elastic axis; however, the effective chord is unchanged, and the added lift is accounted for by an increase of pod span. Case 4 utilizes the plan form of Case 1 and the quarter-chord location in Case 2. Case 5 is essentially a modification of Case 4, having the same plan-form area and nominally the same quarter-chord location but an increased semichord. Case 6 reverts to the plan form of Cases 1 and 4 but adopts an intermediate quarter-chord position.

None of the six arbitrarily chosen tip-pod equivalents listed in Table 6 has given consistent agreement between calculated and observed flutter characteristics. This failure has prompted a re-evaluation of the choice of degrees of freedom to the end that a few supplementary analyses have been made with the addition of the second uncoupled torsion mode.

Some results of the flutter analyses are illustrated for Test Conditions 40 and 62. Only those calculations pertaining to the flutter mode of interest are examined. Fig. 10, applying to Test Condition 40, is a conventional plot of damping coefficient against air speed, where, in contrast to the connotation used in Fig. 6, the damping is that required to sustain simple harmonic motion in the flutter mode. The critical flutter speed is that at which the required damping is equal to the structural damping, taken, typically, as 0.02 on the basis of model measurements. Case 1, with either the three or the four degree of freedom analysis, gives acceptable agreement with the observed flutter speed. It may be conceded that the better agreement provided by the three degree of freedom analysis is virtually coincidental in view of the indicated sensitivity

of critical flutter speed to the assumption of pod effectiveness. Of equally important note, both analyses using Case 1 give flutter frequencies within 2 per cent of the observed flutter frequency, whereas the Cases 2 and 4 show a progressive reduction in the flutter-mode frequency with increasing air speed, pointing toward a substantially low flutter frequency at an excessively high flutter speed.

Fig. 11 shows damping-air speed plots calculated for each of five tip cases applied to Test Condition 62. Here, Case 1 fails to give agreement with observation, whereas Cases 2 and 5 give excellent correspondence with observed flutter speed. However, the flutter frequencies in these latter two cases are calculated as 320 and 400 cycles per min., respectively, as compared with a measured flutter frequency of 700 cycles per min. The flutter speed computed with Case 6 is only about 10 per cent high, but the corresponding flutter frequency is 450 cycles per min., reflecting only a slight improvement over Case 5. Thus none of the five aerodynamic tip cases tried with Test Condition 62 gives acceptable agreement between calculated and observed flutter characteristics.

In general, the results of the analyses of these and a few other test configurations indicate both that the tip-pod representation is an extremely important factor in the flutter analyses and that the number of degrees of freedom chosen is of considerably lesser importance. Further, it appears that (1) the aerodynamic equivalent of a pod is small as compared with the pod plan form and (2) the importance of accurate pod aerodynamic representation is greatest for those configurations having relatively small pod mass unbalance about the wing elastic axis.

In view of these indications, effort is currently being directed toward evolving a more positive means of determining the aerodynamically equivalent tip pod. The approach is as follows.

A "sensitive" test configuration—that is, one having a small pod-unbalance—is subjected to an analysis using the wing reference $v/b\omega$ agreeing with measured flutter speed and flutter frequency. The flutter determinant for the three degrees of freedom, θ, h, and α, is set up to retain the pod aerodynamic terms as dependent variables. The measured flutter frequency and the model structural-damping coefficient are used in forming a known characteristic complex root of this determinant. This root is then substituted in the determinant to leave the pod aerodynamic terms as the only unknowns. Arbitrary assignment of a trial value of equivalent-pod semichord permits evaluation of these aerodynamic terms as complex functions of span, s_T, and dimensionless quarter-chord location, $[(1/2) + a]$. Subsequent manipulation leads to a third-order determinant of rank two having characteristic roots, $1/s_T$. Mathematically, these roots are determined by the particular values of $1/s_T$ and $[(1/2) + a]$ that equate the determinant to zero. Physically, the roots are determined by the condition that they be positive real numbers of reasonable magnitude.

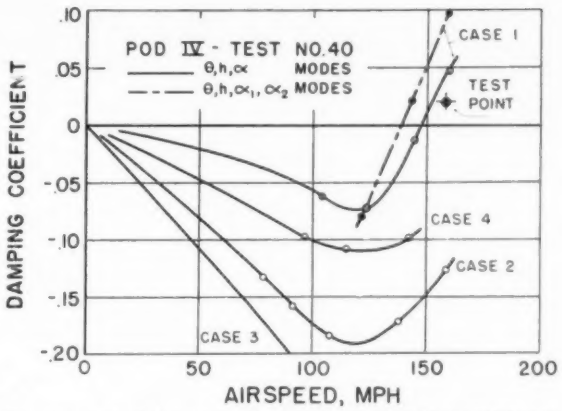

FIG. 10. Calculated damping-air-speed relationships applying to Test Condition 42 with several of the tip cases of Table 6.

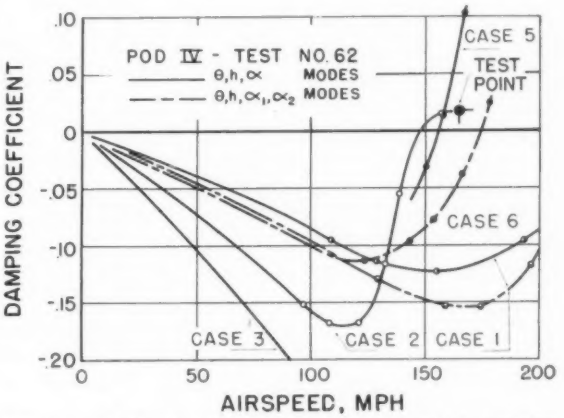

FIG. 11. Calculated damping-air-speed relationships applying to Test Condition 60 with several of the tip cases of Table 6.

With a preselected pod semichord, b_T, the solution for an applicable root, $1/s_T$, proceeds as follows. A trial value of $[(1/2) + a]$ is assigned. A series of physically reasonable $1/s_T$ values is used successively in evaluating the determinant as a complex number. Moduli of each determinantal value are plotted against $1/s_T$, and the minimum modulus is sought. This process is repeated with other values of $[(1/2) + a]$, and the minimum moduli so obtained are plotted against $[(1/2) + a]$. If a real solution exists, the minimum modulus of this plot will be zero or a value differing from zero only because of significant-figure limitations in the computation stages. If a real solution is not obtained with the preselected pod semichord, then a new value of b_T is assigned and the process is repeated. The values of s_T and $[(1/2) + a]$ which produce a zero modulus of the determinant complete the delineation of the aerodynamically equivalent tip pod applying with the chosen semichord.

It is to be expected that a range of b_T values, each associated with particular values of s_T and $[(1/2) + a]$,

can be found by this method to apply to any one test configuration. The particular set of these parameters that represents the tip pod is, in theory, determined by its satisfying the flutter-analysis requirements with other tested configurations. Further, if the assumptions of these flutter analyses are valid, the character of a damping-air-speed curve obtained by use of other $v/b\omega$ values should be consistent with the complementary damping relationship obtained by test.

This procedure is admittedly a brute-force method of ascertaining the existence of a tip-pod aerodynamic equivalent conforming with the definitions and hypotheses of the theoretical treatment. However, the labor entailed in the evaluation of the modified determinants has been made practical by the adoption of IBM computing facilities.

The present status of the investigation does not permit a prediction of the overall reliability and practicability of the method. It is to be hoped, however, that the calculations now in progress will lead to a positive evaluation of the validity of the chosen approach.

Some preliminary results of interest have been obtained by analyzing Test Condition 62 for its equivalent tip-pod parameters, s_T and $[(1/2) + a]$, as functions of measured flutter data and a selected pod semichord of 5.5 in. This value of b_T was chosen merely because it was a Case 1 parameter contributing to a prior success in calculating flutter frequency and critical flutter speed of Test Condition 40. The analysis shows that the observed flutter conditions are satisfied with a pod semichord of 5.5 in., a pod span of 1.5 in., and a quarter-chord location 5.0 in. forward of the wing elastic axis.

This aerodynamically equivalent plan form, called Case 7, has been subsequently applied in a reanalysis of Test Condition 40. The results show a calculated flutter speed of 132 m.p.h. as compared with an observed flutter speed of 158 m.p.h., both values applying with a structural-damping coefficient of 0.02. The calculated flutter frequency is within 1 per cent of the measured flutter frequency.

Results of a few other flutter analyses using the Case 7 pod plan form are as follows:

The three test conditions (60, 57, and 56), represented in Table 4 and Fig. 6, have been analyzed. For Test Condition 60, the calculated flutter speed of 109 m.p.h. compares favorably with the observed speed, 118 m.p.h.; corresponding flutter frequencies are 699 and 700 cycles per min. However, the analyses of Test Condition 56 and 57 have failed to show agreement with the observed flutter behavior. Yet, for the latter of these conditions, the shape of the calculated relationship between damping coefficient and air speed is consistent with the measured relationship of Fig. 6 in the respect that a point of minimum stability is shown at 108 m.p.h.; the damping coefficient is computed to be -0.001 at this speed, or incrementally, about 0.021 more negative than that indicated by test.

Test Condition 37 has pod mass parameters, $M_T = 3.995$ lbs., $S_{a_T} = -11.48$ in.lbs., $I_{a_T} = 148.3$ lb. in.^{2} The calculated flutter speed obtained with the Case 7 plan form is 11 m.p.h. below the observed flutter speed of 157 m.p.h.; the calculated flutter frequency is 3 per cent higher than the measured frequency, 630 cycles per min.

Two of the test conditions represented in Fig. 4 also have been subjected to flutter analysis. The condition having the incremental weight located 8.3 in. aft of the wing elastic axis has a calculated flutter speed 15 m.p.h. below the observed speed of 138 m.p.h.; agreement between computed and measured flutter frequencies is good. Calculations for the condition having the incremental weight 17.1 in. aft of the elastic axis show a flutter speed in excess of 165 m.p.h. but a point of minimum stability ($g = +0.016$) at 130 m.p.h. Significantly, the damping records obtained during the wind-tunnel test of this condition show behavior of a similar character, with minimum damping occurring somewhere in the range between 135 and 145 m.p.h.

The Case 7 tip-pod equivalent appears to be far superior to any of the wholly arbitrary Cases 1 through 6 because of its leading to reasonably good agreement between calculated and observed flutter characteristics in six of the eight analyses made to date. Moreover, it is considered unlikely that this plan form is the best representation that may be made, since the semichord was selected more or less arbitrarily. Therefore, it may be expected that an extension of the treatment could lead to a somewhat different set of parameters, b_T, s_T, and $[(1/2) + a]$ giving an overall improvement in analytical results.

The limited test results presented in Table 3 are not inconsistent with the results of the flutter analyses described herein. For these test cases of moderately large pod overbalance, the inertia coupling among modes apparently predominates over the changes in aerodynamic coupling to reflect a relative insensitivity of flutter characteristics to the imposed changes in pod shape or pod location on the wing. Had this type of behavior been sensed at the time of these tests, additional tests of the same nature would have been conducted with pod configurations having centers of gravity close to the wing elastic axis. It is surmised that such tests might reveal a greater sensitivity of flutter speed to the changes in pod geometry. Sewall and Woolston have made limited comparison tests of this type on a straight cantilever wing. Their data, covering two cases of large and small unbalance of the concentrated tip weight, indicate that the flutter speeds and frequencies are relatively unaffected by radical changes in the aerodynamic shape of the tip weight. However, they do not conclude that such is generally the case. Indeed, it is contended herein that entirely different degrees of importance of pod aerodynamic effects may be anticipated in different régimes of pod weight distribution

and, for that matter, in symmetric and antisymmetric flutter cases.

Conclusion

The potential sensitivity of wing-and-pod flutter characteristics to relatively small changes in pod mass parameters has been demonstrated by test.

The theoretical studies indicate that, while the aerodynamically effective tip pod may be small in comparison with pod geometric plan form, an accurate representation of this effective tip pod may be essential to a successful flutter analysis. Further, it is indicated that analyses of wing-and-pod configurations having the pod center of gravity on or near the wing elastic axis are more adversely affected by errors in pod aerodynamic representation than are those analyses applying to cases of large pod overbalance.

Conclusions on the general reliability and the practicability of the investigated methods of flutter analysis are deemed premature in consideration of the fluid status of the development. From a positive point of view, there is some basis for expecting an improvement in analytical predictions of flutter speeds, although the embryonic method of analysis requires the use of applicable test data.

Accordingly, the view is currently held that flutter-model testing offers the more certain and the more direct method of evaluating the flutter safety of wing-and-tip pod configurations prior to flight test of the aircraft. Adoption of this view forces attention on the problems incident to attainment of dynamic similarity between model and prototype not only with respect to simulation of elastic behavior but also with respect to simulation or conservative representation of fuel inertia properties.

References

[1] Sewall, John L., and Woolston, Donald S., *Preliminary Experimental Investigation of Effects of Aerodynamic Shape of Concentrated Weights on Flutter of a Straight Cantilever Wing*, N.A.C.A. R.M. L9E17, July, 1949.

[2] Smilg, B., and Wasserman, L. S., *Application of Three-Dimensional Flutter Theory to Aircraft Structures*, Technical Report No. 4798, Air Materiel Command, U.S.A.F., Dayton, Ohio, July, 1942.

Eighth International Congress for Applied Mechanics

The Eighth International Congress for Applied Mechanics is to be held at the University of Istanbul, Istanbul, Turkey, on August 20 to 28, 1952. American participation in the Congress is being organized by the U.S. National Committee on Theoretical and Applied Mechanics, which is a Joint Committee of the A.S.M.E., A.I.Ch.E., S.E.S.A., A.S.C.E., I.A.S., A.M.S., and A.P.S.

Five sessions are to be held, as follows: (1) Elasticity, Plasticity, and Rheology; (2) Fluid Mechanics (Aerodynamics and Hydrodynamics); (3) Mechanics of Solids (Ballistics, Vibrations, Friction, and Lubrication); (4) Statistical Mechanics, Thermodynamics, and Heat Transfer; (5) Mathematics of Physics and Mechanics—Methods of Computation.

Membership in the Congress is open to all individuals interested in Applied Mechanics. Each member may present two 15-minute papers. Abstracts (not to exceed 400 words) must be submitted not later than June 1, 1952, on forms that may be secured from the Secretary of the Congress (**Sekizinci Enternasyonal Teorik ve Tatbiki Mekanik Kongresi, P. K. 245, Istanbul, Turkey**).

The American Express Company is the official travel agency for the Congress. For details of the groups tours being planned, write to: **American Express Company, 624 Fourteenth St., N.W., Washington, D.C.** Individual tours to meet special requirements may also be arranged through this agency.

The Effect of Nonlinear Aerodynamic Characteristics on the Dynamic Response to a Sudden Change in Angle of Attack

TELFORD W. OSWALD*

Douglas Aircraft Company, Inc.

ABSTRACT

The effect of nonlinear pitching moment and lift variations with angle of attack on the dynamic response to a sudden change in angle of attack is considered. An approximate solution to the nonlinear equation of motion is developed. Several numerical examples are considered, and the results of the approximate solution are compared with the accurate results of numerical integration, as well as the classical linearized solution. The effect of a nonlinear moment curve on the determination of stability derivatives from flight-test data is discussed in the light of these examples.

(I) INTRODUCTION

THE SOLUTIONS TO THE EQUATIONS OF MOTION of an airplane when subjected to small disturbances from steady flight have been well known to aeronautical engineers for the past several years. The classical treatment of the problem is due largely to G. H. Bryan, who applied the theory of small oscillations previously developed by Routh. Bryan assumed that the forces and moments due to a slight disturbance from a state of equilibrium depend linearly on the disturbance. The solution is then shown to depend on a number of constants called stability derivatives. Until recently, there has been little or no change in the theory, and it is in use today essentially in the form developed by Bryan.

It should be noted that the classical theory applies strictly only in the case of infinitesimal disturbances. However, the results have been found to apply with reasonable accuracy to finite disturbances of the magnitude experienced in the flight of conventional subsonic airplanes. In other words, the second-order terms neglected in the theory do not have any appreciable effect on the motion.

However, in the case of high-speed airplanes and missiles, serious deviations from the conditions of the classical theory occur when one attempts to extend the results to the case of finite disturbances. In most missile configurations, small aspect ratio wings are mounted in tandem on proportionately large diameter bodies. This exaggerates the aerodynamic interference effects, and such missiles exhibit markedly nonlinear dependence of the aerodynamic forces and moments on the angle of attack. Consequently, the amplitude of disturbances for which one would expect the classical theory to be valid is considerably reduced. At the same time, in the normal operation of such missiles, large sudden changes in the angle of attack are frequently required. Hence, it would appear that, in the case of supersonic missiles, the extension of the theory of small oscillations to finite disturbances is questionable.

In the present paper, the effect of nonlinear variation of lift and pitching moment with angle of attack on the dynamic response to a step function input in angle of attack is investigated. The missile is assumed to be flying at constant speed and altitude. The problem is reduced to an ordinary second-order nonlinear differential equation that cannot be solved exactly by methods known today. However, approximate solutions may be obtained, and, by the method of numerical integration, a solution to any desired degree of accuracy can be obtained.

The stability of the nonlinear system is determined from considerations of the solution in the neighborhood of the critical points of the differential equation, and the investigation of the dynamic response is confined to systems that have been previously determined to be stable.

In its application to a guided missile the problem of dynamic response properly involves the combination of the missile as an aerodynamic body and the control system. But since ultimately any motion of the missile must be brought about by aerodynamic forces, it is desirable to know the dynamic behavior of the missile alone. In particular, the "overshoot" characteristic of the response to a sudden change in trim position is important in the design of the control system, since it indicates the amount of "feedback" necessary to provide satisfactory steering of the missile.

In the present analysis, an attempt is made to approximate this overshoot without resorting to the tedious method of numerical integration. A comparison of this approximation with the numerical solution and the linearized solution is presented.

An important problem confronting the aerodynamicist working in the field of guided missiles is the reduction of flight-test data in order to evaluate the stability derivatives. One of the procedures followed is to

Presented at the Annual Summer Meeting, I.A.S., Los Angeles, June 27–29, 1951.

* Research Engineer, Santa Monica, Calif.

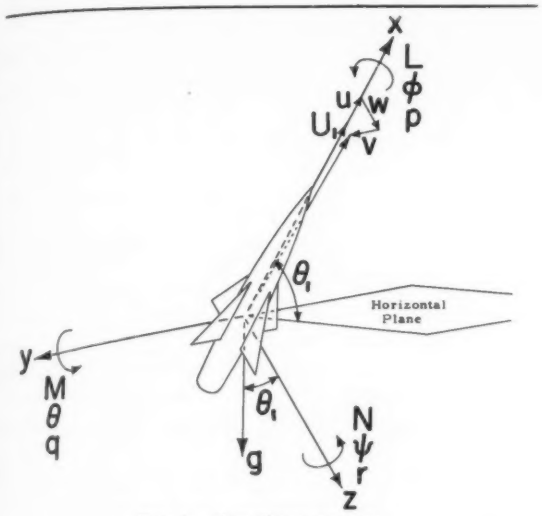

FIG. 1. Coordinate system.

analyze the transient response of the missile to a step-function input in the control-surface deflection. This is equivalent to a step-function input in the angle of attack. In Appendix (II) of this paper the effect of a nonlinear moment curve on this procedure is discussed.

(II) Coordinates, Notation, and Symbols

The equations of motion for a missile can be referred to a set of body axes that are fixed in the missile and move with it. An orthogonal set of principal body axes with origin in the missile center of gravity (the x-axis the longitudinal centerline, the y-axis in the normally horizontal plane, and the z-axis in the normally vertical plane) is selected. This coordinate system is shown in Fig. 1. The velocities, moments, angular velocities, displacements, and angular displacements are all defined in accordance with the right-hand rule.

Throughout the text, the usual convention of placing a dot over a quantity to denote differentiation with respect to time is used. Whenever a fractional power of a quantity is involved, the positive real branch of the multivalued function is taken. For the inverse trigonometric functions, the principal branch is taken. In the following list the principal quantities used in this paper are defined:

A, B, C, D, E, F = coefficients of nonlinear equation of motion—defined in text

a = speed of sound, ft. per sec.

c = reference chord for moment coefficients, ft.

C_L = $L/(1/2)\rho\bar{V}^2S$ = lift coefficient

C_M = $M/(1/2)\rho\bar{V}^2Sc$ = pitching moment coefficient

$C_{L_{\alpha_t}}$ = $\partial C_L/\partial\alpha$, evaluated at trim position

$C_{M_{\alpha_t}}$ = $\partial C_M/\partial\alpha$, evaluated at trim position

$C_{M_{\dot{\alpha}}}$ = $\partial C_M/\partial(\dot{\alpha}c/2\bar{V})$, evaluated at $\dot{\alpha} = 0$

C_{M_q} = $\partial C_M/\partial(qc/2\bar{V})$, evaluated at $q = 0$

$\mathfrak{F}(\psi, \phi)$ = incomplete elliptic integral of first kind

g = acceleration of gravity, ft./sec.^{2}

I_x = $\int(y^2 + z^2)dm$ = moment of inertia about x-axis (roll), lbs. sec.^{2}/ft.

I_y = $\int(x^2 + z^2)dm$ = moment of inertia about y-axis (pitch), lbs. sec.^{2}/ft.

I_z = $\int(x^2 + y^2)dm$ = moment of inertia about z-axis (yaw), lbs. sec.^{2}/ft.

$k_{1,2,3}$ = constants used to define nonlinear lift curve

$K_{1,2,3}$ = constants used to define nonlinear moment curve

$K(\psi)$ = complete elliptic integral of first kind

L = lift, lbs.; rolling moment, lb. ft.

m = mass, lbs. sec.^{2}/ft.

M = pitching moment, lb. ft.; Mach Number

n = accelerometer reading

N = yawing moment, lb. ft.

p = $\dot{\phi} = \partial\phi/\partial t$ = perturbation in roll rate (angular velocity about x-axis), rad. per sec.

P = $\dot{\Phi} = \partial/\partial t$ = roll rate, rad. per sec.

P_1 = steady-state value of P

q = $\dot{\theta} = \partial\theta/\partial t$ = perturbation in pitch rate (angular velocity about y-axis), rad. per sec.

Q = $\dot{\Theta} = \partial\Theta/\partial t$ = pitch rate, rad. per sec.

Q_1 = steady-state value of Q

q' = $(1/2)\rho\bar{V}^2$ = dynamic pressure, lbs. per sq.ft.

r = $\dot{\psi} = \partial\psi/\partial t$ perturbation in yaw rate (angular velocity about z-axis), rad. per sec.

R = $\dot{\Psi} = \partial\dot{\Psi}/\partial t$ = yaw rate, rad. per sec.

R_1 = steady-state value of R, rad. per sec.

R_c = radius of curvature of flight path, ft.

S = reference area for aerodynamic coefficients, sq.ft.

t = time, sec.

u = velocity perturbation in x-direction, ft. per sec.

U = velocity component in x-direction, ft. per sec.

U_1 = steady-state value of U, ft. per sec.

v = velocity perturbation in y-direction, ft. per sec.

V = velocity component in y-direction, ft. per sec.

V_1 = steady-state value of V, ft. per sec.

$\bar{V}$ = missile velocity, ft. per sec.

w = velocity perturbation in z-direction, ft. per sec.

W = velocity component in z-direction, ft. per sec.

W_1 = steady-state value of W

x, y, z = coordinate axis, right-handed principal body axes (roll, pitch, yaw axis, respectively)

X = force in x-direction, lbs.

Y = force in y-direction, lbs.

Z = force in z-direction, lbs.

X_μ = $\partial X/\partial\mu$ = resistance derivative, rate of change of force in x-direction with velocity in x-direction, lbs. sec./ft.

$(X, Z)_{u, w, \dot{w}, q}$; $(Y)_{p, v, \dot{v}, r}$ = resistance derivatives, lbs. sec./ft.

$(M)_{u, w, \dot{w}, q}$; $(L, N)_{p, v, \dot{v}, r}$ = rotary derivatives, lbs. sec.

$(M')_{w, \dot{w}, q}$ = $(M)_{w, \dot{w}, q}/I_y$

α = angle of attack, rad.

η = damping constant, 1/time

ϑ = w/U_1 = incremental angle of attack, rad.

θ = perturbation angular displacement in pitch, rad.

Θ = angular displacement in pitch measured from horizontal, rad.
Θ_1 = steady-state value of Θ
ρ = mass density of air, lbs. sec.^{2}/ft.
τ = time, sec.
ω = circular frequency, rad. per sec.
ω_n = natural undamped circular frequency, rad. per sec.
Ω = phase angle, rad.

(III) Equations of Motion

The equations of motion are referred to a set of principal body axes; hence, all product of inertia terms vanish. It is assumed that the missile is initially in a state of steady flight, that the linear and angular velocities and displacements can be represented as

$$\left.\begin{aligned} U &= U_1 + u, \quad P = P_1 + p, \quad \Theta = \Theta_1 + \theta \\ V &= V_1 + v, \quad Q = Q_1 + q, \quad \Phi = \Phi_1 + \varphi \\ W &= W_1 + w, \quad R = R_1 + r, \quad \Psi = \Psi_1 + \psi \end{aligned}\right\} \quad (1)$$

and that $P_1 = R_1 = \Phi_1 = \Psi = 0$. It is also assumed that θ is sufficiently small that $\sin\theta$ may be taken equal to θ and $\cos\theta$ may be taken equal to 1 and that u, v, w, p, q, r are sufficiently small that their squares and products may be neglected. The equations of motion are, then,

$$\left.\begin{aligned} m[\dot{u} - V_1 r + W_1(Q_1 + q)] &= X - mg\sin\Theta_1 - mg\cos\Theta_1\theta \\ m(\dot{v} - W_1 p + U_1 r) &= Y + mg\cos\Theta_1\varphi \\ m[\dot{w} - U_1(Q_1 + q) + V_1 p] &= Z + mg\cos\Theta_1 \\ I_x\dot{P} = L;\quad I_y\dot{q} = M;\quad I_z\dot{r} &= N \end{aligned}\right\} \quad (2)$$

If the motion is confined to infinitesimals, each of the air reactions can be expressed in the form

$$X = X_1 + \frac{\partial X}{\partial U}dU + \frac{\partial X}{\partial W}dW + \frac{\partial X}{\partial V}dV + \frac{\partial X}{\partial Q}dQ + \frac{\partial X}{\partial P}dP + \frac{\partial X}{\partial R}dR$$

where the second-order terms are neglected. The partial derivatives are then written in the form $\partial X/\partial U = X_u$ and are known as "stability derivatives." To investigate the effect of the nonlinear variation of pitching moment and lift with angle of attack on the dynamic behavior of a missile, the second- and third-order terms in dW are included in the expressions for M and Z. Accordingly, instead of the usual notation $M_w w$, $Z_w w$, these terms are written $M(w)$, $Z(w)$, respectively.

If the missile has a longitudinal plane of symmetry (which is usually the case) and if it is flying at zero yaw, many of the stability derivatives are zero, and the set of six simultaneous equations [Eqs. (2)] reduce to two sets of three equations each,

$$m(\dot{u} + W_1 q + g\cos\Theta_1\theta) = X_u u + X_w w + X_q q + X_1 - mg\sin\Theta_1 - mW_1 Q_1 \quad (3.1)$$

$$m(\dot{w} - U_1 q + g\sin\Theta_1\theta) = Z_u u + Z(w) + Z_q q + Z_{\dot{w}}\dot{w} + Z_1 + mg\cos\Theta_1 + mU_1 Q_1 \quad (3.2)$$

$$I_y\dot{q} = M_u u + M(w) + M_q q + M_{\dot{w}}\dot{w} + M_1 \quad (3.3)$$

$$m(\dot{v} + U_1 r - W_1 P - g\cos\Theta_1\varphi) = Y_v v + Y_p p + Y_r r + Y_{\dot{v}}\dot{v} + Y_1 \quad (4.1)$$

$$I_x\dot{p} = L_v v + L_p p + L_r r + L_1 \quad (4.2)$$

$$I_z\dot{r} = N_v v + N_P P + N_r r + N_{\dot{v}}\dot{v} + N_1 \quad (4.3)$$

It is to be emphasized that these equations are referred to principal body axes instead of the more commonly used "wind" axes or so-called "stability" axes and that the appropriate expressions for the stability derivatives must be used.

Considering the longitudinal Eqs. (3), it is observed that, if $Z_u = M_u = 0$, Eqs. (3.2) and (3.3) become independent of Eq. (3.1), and the pitch motion can be described by a two degree of freedom system. For a missile that is symmetrical with respect to the yaw plane and which is trimmed at zero angle of attack, it is apparent that the lift and moment on the missile are zero and that their derivatives with respect to u will be identically equal to zero. Hence, it is to be expected that at small angles of attack the coupling of u with w and θ is small and that the system can be adequately treated as a two degree of freedom system. This means that the influence of the long-period motion on the short-period motion is negligible. Calculations for representative missiles have been carried out, and this is indeed found to be the case. The results of these calculations are presented in Table 1.

Table 1
Effects of Long-Period Oscillation and Gravity on the Characteristics of the Short-Period Oscillation for a Representative Missile

Mach Number	2.45	1.42
Altitude (ft.)	40,000	70,000
Angle of climb	83°	15°
Three degrees of freedom including gravity		
Damping constant	0.76	0.12
Circular frequency	4.78	1.38
Two degrees of freedom including gravity		
Damping constant	0.76	0.12
Circular frequency	4.77	1.38
Two degrees of freedom neglecting gravity		
Damping constant	0.75	0.12
Circular frequency	4.78	1.38

It is noted that the long period for a supersonic missile is of the order of 100 sec., whereas the short period is of the order of 1 sec. Therefore it is to be expected that the long period should have no appreciable effect on the short period. Furthermore, it is obvious that the short-period motion is the one that is important for steering and control. The long-period motion would appear to be of little practical importance, since the assumptions made will certainly be violated during the course of the long period.

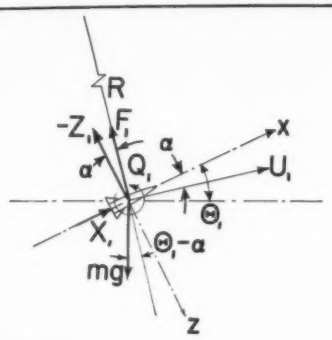

For equilibrium:

$$F_1 = -Z_1 \cos\alpha + X_1 \sin\alpha - mg\cos(\Theta_1 - \alpha)$$
$$X_1 \cos\alpha = mg \sin(\Theta_1 - \alpha)$$

For small values of α, neglecting squares

$$F_1 = -Z_1 - mg\cos\Theta_1$$

FIG. 2. Forces acting on missile turning in vertical plane.

If it is assumed that the missile is stabilized in roll, the lateral Eqs. (4) reduce to exactly the same form as the longitudinal equations except for the gravity terms.

Returning to the longitudinal equations, dividing Eq. (3.2) by m and Eq. (3.3) by I_y and designating by primes the quantities so divided, the equations become

$$(1 - Z_{\dot{w}}')\dot{w} - Z'(w) - (U_1 + Z_q')q = Z_1' - g\sin\Theta_1\theta + g\cos\theta_1 + U_1Q_1 \quad (5.1)$$

$$-M_{\dot{w}}'\dot{w} - M'(w) - M_q'q + \dot{q} = M_1' \quad (5.2)$$

There remains a bothersome term in these equations—namely, $g \sin \Theta_1\theta$. If the missile is flying at a small angle of climb, $\sin \Theta_1 = 0$ and this term may be neglected. However, as is often the case, if the missile is flying in a nearly vertical direction, it is not apparent that this term may properly be neglected. Furthermore, its presence gives rise to an additional root to the characteristic equation, and this additional root is divergent. The divergence is slow, however, and it can be shown that it represents the curvature of the flight path due to gravity. This curvature will have a negligible effect on the oscillations about the flight path during the time interval for which the motion is being studied. Computations for representative cases have been made, and the results are shown in Table 1. These results indicate that there is no appreciable error involved in neglecting gravity.

Noting that $Z_q' \ll U_1$ and $Z_{\dot{w}}' \ll 1$, hence Z_q' and $Z_{\dot{w}}'$ can be neglected and Eqs. (5) are written

$$\dot{w} - Z'(w) - U_1q = Z_1' + U_1Q_1 + g\cos\Theta_1 \quad (6.1)$$

$$-M_{\dot{w}}'\dot{w} - M'(w) - M_q'q + \dot{q} = M_1' \quad (6.2)$$

Solving Eq. (6.1) for q and substituting into Eq. (6.2), the system is reduced to the one equation of motion,

$$\frac{\ddot{w}}{U_1} - \frac{Z'(\dot{w})}{U_1} - M'(w) - M'q\left(\frac{\dot{w}}{U_1} - \frac{Z'(w)}{U_1}\right) - M_{\dot{w}}'\dot{w} = M_1' - \frac{M_q'}{U_1}(Z_1' + U_1Q_1 + g\cos\Theta_1) \quad (7)$$

If it is desired to compute the response to a step function input in control-surface deflection, the forcing functions, M_1' and Z_1' can be written as step functions and the response computed directly from Eq. (7). The incremental velocity, w, is measured from the original trim position, and Q_1 and Θ_1 correspond to the steady-state values at the original trim position. Alternatively, a linear transformation in w can be made such that $w = 0$ corresponds to the trim position at the new control-surface deflection, whence Q_1 and Θ_1 are referred to the new trim position. The solution of the transformed equation is found subject to the initial conditions, $w(0) = w_0$ and $\dot{w}(0) = 0$, where w_0 corresponds to the old trim position measured in the new coordinate system. If this latter point of view is adopted, $M_1' = 0$, Z_1' is the aerodynamic force in the z-direction, and Q_1 is the angular velocity for the steady-state motion in the new trim position. For the steady-state motion of the missile in a vertical plane, equilibrium of forces in the z-direction, neglecting squares of the angle of attack (Fig. 2), requires

$$-Z_1 - mg\cos\Theta_1 = mR_0Q_1^2$$

where R_0 is the radius of curvature of the flight path. But $U_1 = Q_1R_0$, hence

$$-Z_1 - mg\cos\Theta_1 = mU_1Q_1 \text{ or } -Z' - g\cos\Theta_1 = U_1Q_1$$

and the right-hand side of Eq. (7) is zero. The problem is now reduced to finding a solution to the homogeneous equation,

$$\frac{\ddot{w}}{U_1} - \frac{Z'(\dot{w})}{U} - M'(w) - M_q'\left(\frac{\dot{w}}{U_1} - \frac{Z'(w)}{U_1}\right) - M_{\dot{w}}'\dot{w} = 0 \quad (8)$$

with the initial conditions

$$w(0) = w_0, \quad \dot{w}(0) = 0$$

In order to formulate the problem in a manner amenable to solution by analytical means, the pitching moment and normal force as functions of the angle of attack are approximated by polynomials. It is convenient to use cubic polynomials of the form

$$M(\vartheta) = M_{\alpha_i}\vartheta + K_1\vartheta^2 + K_2\vartheta^3$$
$$Z(\vartheta) = Z_{\alpha_i}\vartheta + k_1\vartheta^2 + k_2\vartheta^3$$

where ϑ is the increment in angle of attack measured from the trim position. Since w is a small quantity compared with U_1, $\vartheta = w/U$, neglecting higher order terms. Substituting these relations into Eq. (8) and collecting terms,

$$\ddot{\vartheta} + (A + B\vartheta + E\vartheta^2)\dot{\vartheta} + (C + D\vartheta + F\vartheta^2)\vartheta = 0 \quad (9)$$

and the initial conditions are

$$\vartheta(0) = \alpha_0 = w_0/U_1, \quad \dot{\vartheta}(0) = 0$$

where

$$A = -M_q' - \frac{Z_{\alpha_t}'}{U_1} - U_1 M_{\dot{w}}' = \frac{q'Sc^2}{2I_y U_1} \times \left(-C_{M_q} - C_{M_{\dot{\alpha}}} + \frac{2I_y}{mc^2} C_{L_{\alpha_t}}\right)$$

$$B = \frac{-2k_1'}{U_1} = \frac{q'S}{mU_1}\frac{\partial^2 C_L}{\partial \alpha_t^2}$$

$$E = \frac{-3k_2'}{U_1} = \frac{q'S}{2mU_1}\frac{\partial^3 C_L}{\partial \alpha_t^3}$$

$$C = -M_{\alpha_t}' + \frac{M_q' Z_{\alpha_t}'}{U_1} = \frac{q'Sc}{I_y}(-C_{M_{\alpha_t}}) + \left(\frac{q'Sc}{U_1}\right)^2 \frac{C_{L_{\alpha_t}}(-C_{M_q})}{2I_y m}$$

$$D = -K_1' + \frac{k_1' M_q'}{U_1} = \frac{q'Sc}{2I_y}\left(-\frac{\partial^2 C_M}{\partial \alpha_t^2}\right) + \left(\frac{q'Sc}{U_1}\right)^2 \frac{(1/2)(\partial^2 C_L/\partial \alpha_t^2)(-C_{M_q})}{2I_y m}$$

$$F = -K_2' + \frac{k_2' M_q'}{U_1} = \frac{q'Sc}{I_y}\left(\frac{-1}{3!}\frac{\partial^3 (C_M)}{\partial \alpha_t^3}\right) + \left(\frac{q'Sc}{U_1}\right)^2 \frac{(1/3!)(\partial^3 C_L/\partial \alpha_t^3)(-C_{M_q})}{2I_y m}$$

Before proceeding with the solution of Eq. (9), it is desirable to establish the stability of the system. This is done in the usual manner by considering the solution in the neighborhood of the critical points of the equation and identifying the type of the critical points. Assuming a stable system, it is desired to find a solution to the equation

$$\ddot{\vartheta} + f(\vartheta)\dot{\vartheta} + g(\vartheta)\vartheta = 0 \tag{10}$$

subject to the initial conditions, $\vartheta(0) = \alpha_0$, $\dot{\vartheta}(0) = 0$, where, in particular

$$f(\vartheta) = A + B\vartheta + E\vartheta^2$$

$$g(\vartheta) = C + D\vartheta + F\vartheta^2$$

and without loss of generality, α_0 is taken < 0. Unfortunately, the exact solution to this equation cannot be expressed in terms of the known functions of mathematics (except in the cases $A = B = E = 0$ or $B = E = D = F = 0$). However, a solution to any desired degree of accuracy can be obtained by the methods of numerical integration. This procedure is tedious when done by hand and is best accomplished by means of automatic computing machines. The latter method is expensive and the additional cost cannot always be justified. It is therefore desirable to find an approximate solution in terms of the tabulated functions of mathematics.

An iteration or perturbation procedure would appear to be in order. However, because of the nature of the nonlinearities assumed, the first-order approximation is not sufficient. Furthermore, since $g(\vartheta)\vartheta$ is of the third power in ϑ and $f(\vartheta)$ is of the second power in ϑ, the differential equations for the second and higher approximations become increasingly complex, and the numerical application of the results to any specific example becomes even more tedious than numerical integration, while the results are less accurate. For these reasons, this approach has been abandoned.

A step-by-step approximating procedure has been resorted to. The equation is linearized over a closed interval of the amplitude of ϑ, the linearization being based on a time average of the response over the interval. The constants used in the linearization are changed for each step. In the following section, this method is developed and explained. The analysis is of necessity lacking in mathematical rigor and relies heavily on physical intuition and analogy to the well-known linear oscillator.

The solution to the equation

$$\ddot{\vartheta} + \eta\dot{\vartheta} + \omega_n^2\vartheta = 0 \tag{11}$$

where η and ω_n are constants, subject to the initial conditions,

$$\vartheta(0) = \alpha_0, \quad \dot{\vartheta}(0) = 0$$

is well known to be

$$\vartheta = \alpha_0(\omega_n/\omega)e^{-(\eta/2)t}\cos(\omega t - \Omega) \tag{12}$$

where

$$\omega = [\omega_n^2 - (\eta/2)^2]^{1/2}$$
$$\Omega = \tan^{-1}[(\eta/2)/\omega]$$

and the first derivative is given by

$$\dot{\vartheta} = -\alpha_0\omega_n(\omega_n/\omega)e^{-(\eta/2)t}\sin \omega t \tag{13}$$

If values of ω_n^2 and η are selected to replace $g(\vartheta)$ and $f(\vartheta)$, respectively, in Eq. (10), the approximate solution can be written as Eq. (11), which will be valid for sufficiently small values of time. It is noted that, in the theory of small oscillations, $\omega_n^2 = C$ and $\eta = A$, but this approximation is unsatisfactory for the magnitude of values of ϑ under consideration here.

Before selecting a value of ω_n^2, it is observed that in the linearized case, the damping factor, η, has a second-order effect on the frequency, ω. For example, if $(\eta/2)/\omega_n = 0.6$—i.e., the system is 60 per cent critically damped—$\omega = 0.80\omega_n$—i.e., the frequency is 80 per cent of the undamped natural frequency. If $(\eta/2)/\omega_n = 0.2$—i.e., the system is 20 per cent critically damped—$\omega = 0.98\omega_n$—i.e., the frequency is approximately 98 per cent of the undamped natural frequency. In the cases that arise in practice, the missile is considerably less than 60 per cent critically damped; in fact, it is usually of the order of 25 per cent or less. Since it is desired to find ϑ as a function of time, it would

seem reasonable to select a value of ω_n corresponding to the frequency of the undamped system.

Accordingly, consider for the moment $f(\vartheta) = \eta \equiv 0$. Now Eqs. (10) and (11) become, respectively,

$$\ddot{\vartheta} + g(\vartheta)\vartheta = 0, \quad \vartheta(0) = \alpha_0, \quad \dot{\vartheta}(0) = 0 \tag{14}$$

$$\ddot{\vartheta} + \omega_n^2\vartheta = 0, \quad \vartheta(0) = \alpha_0, \quad \dot{\vartheta}(0) = 0 \tag{15}$$

Eq. (14) can be solved as follows:

$$\ddot{\vartheta} = (d/d\vartheta)\,(\dot{\vartheta}^2/2) = -g(\vartheta)\vartheta$$

Integrating with respect to ϑ,

$$\frac{\dot{\vartheta}^2}{2} = -\int_{\alpha_0}^{\vartheta} g(x)x\,dx = G(\alpha_0) - G(\vartheta) \tag{16}$$

If $g(\vartheta)$ is a polynomial in ϑ, $G(\alpha_0) - G(\vartheta)$ will also be a polynomial in ϑ, and, hence, $\dot{\vartheta}^2 = P(\vartheta)$, where $P(\vartheta)$ is again a polynomial in ϑ. Writing

$$\dot{\vartheta} = d\vartheta/dt = [P(\vartheta)]^{1/2} \tag{17}$$

and integrating,

$$t = \int_{\alpha_0}^{\vartheta} dx/[P(x)]^{1/2} \tag{18}$$

which defines ϑ as a function of t.

Similarly, Eq. (15) can be solved, and its solution is

$$t = \int_{\alpha_0}^{\vartheta} \frac{dx}{\omega_n(\alpha_0^2 - x^2)^{1/2}} \tag{19}$$

Letting the interval under consideration be $\alpha_0 \leq \vartheta \leq \vartheta_1$ where $\alpha_0 < 0$, then from Eq. (18),

$$t_1 = \int_{\alpha_0}^{\vartheta_1} \frac{dx}{[P(x)]^{1/2}}$$

and from Eq. (19),

$$t_1' = \int_{\alpha_0}^{\vartheta_1} \frac{dx}{\omega_n(\alpha_0^2 - x^2)^{1/2}} = \frac{\left[\dfrac{\pi}{2} - \sin^{-1}\left(\dfrac{\vartheta_1}{\alpha_0}\right)\right]}{\omega_n}$$

Equating $t_1 = t_1'$ and solving for ω_n,

$$\omega_n = \frac{(\pi/2) - \sin^{-1}(\vartheta_1/\alpha_0)}{\displaystyle\int_{\alpha_0}^{\vartheta_1} \frac{dx}{[P(x)]^{1/2}}}$$

and the approximate solution to Eq. (12) can be written:

$$\vartheta = \alpha_0 \cos \omega_n t \tag{20}$$

for which

$$\dot{\vartheta} = \alpha_0\omega_n \sin \omega_n t \tag{21}$$

Consider now Eq. (10) with $f(\vartheta) \not\equiv 0$. Forming an energy balance,

$$\frac{\dot{\vartheta}^2}{2} + \int_{\alpha_0}^{\vartheta} g(x)x\,dx = -\int_{\alpha_0}^{\vartheta} f(\vartheta)\dot{\vartheta}\,d\vartheta$$

where the integral on the right-hand side represents the energy dissipated during the time ϑ varies from α_0 to ϑ. Letting $E_{\text{dis.}}$ represent this integral,

$$E_{\text{dis.}} = \int_{\alpha_0}^{\vartheta} f(\vartheta)\dot{\vartheta}\,d\vartheta = \int_0^t f[\vartheta(\tau)]\dot{\vartheta}^2(\tau)\,d\tau \tag{22}$$

Similarly, for the linearized system,

$$\frac{\dot{\vartheta}^2}{2} + \frac{\omega_n^2}{2}(\vartheta^2 - \alpha_0^2) = -\eta\int_{\alpha_0}^{\vartheta} \dot{\vartheta}\,d\vartheta$$

$$E_{\text{dis.}}' = \eta\int_0^t \dot{\vartheta}^2(\tau)\,d\tau \tag{23}$$

Substituting the approximate solution to Eq. (14) as given by Eqs. (20) and (21) into Eqs. (22) and (23),

$$E_{\text{dis.}} = \alpha_0^2\omega_n \int_0^{\omega_n t} f(\alpha_0 \cos x)\sin^2 x\,dx$$

$$E_{\text{dis.}}' = \alpha_0^2\omega_n\eta\left(\frac{\omega_n t}{2} - \frac{\sin 2\omega_n t}{4}\right)$$

Now at the end of time t_1, equating the energy dissipated in the two systems—i.e., $E_{\text{dis.}} = D_{\text{dis.}}'$—and solving for η,

$$\eta = \frac{\displaystyle\int_0^{\omega_n t_1} f(\alpha_0 \cos x)\sin^2 x\,dx}{(\omega_n t_1/2) - (\sin 2\omega_n t_1/4)}$$

The approximate solution to Eq. (10) valid in the time interval $0 \leq t \leq t_1$ for which $\alpha_0 \leq \vartheta \leq \vartheta_1$ is, then,

$$\vartheta = \alpha_0(\omega_n/\omega)e^{-(\eta/2)t}\cos(\omega t - \Omega) \tag{24}$$

where

$$\left.\begin{aligned}
\omega_n &= \frac{\sin^{-1}(\vartheta_1/\alpha_0)}{\displaystyle\int_{\alpha_0}^{\vartheta_1} \frac{dx}{[P(x)]^{1/2}}} \\
t_1 &= \sin^{-1}(\vartheta_1/\alpha_0)/\omega_n \\
\eta &= \frac{\displaystyle\int_0^{\omega_n t_1} f(\alpha_0 \cos x)\sin^2 x\,dx}{(\omega_n t_1/2) - (\sin 2\omega_n t_1/4)} \\
\omega &= [\omega_n^2 - (\eta/2)^2]^{1/2} \\
\Omega &= \tan^{-1}[(\eta/2)/\omega]
\end{aligned}\right\} \tag{25}$$

Differentiating Eq. (24), the value of $\dot{\vartheta}$ is found to be

$$\dot{\vartheta} = -\alpha_0\omega_n(\omega_n/\omega)e^{-(\eta/2)t}\sin \omega t \tag{26}$$

It is observed from Eqs. (16) for the linearized system that, as $\eta \to 0$, $\omega \to \omega_n$ and $\Omega \to 0$; hence, $\dot{\vartheta} \to -\alpha_0\omega_n \sin \omega_n t$, which agrees identically with Eq. (21). The quantity $|\alpha_0\omega_n|$ represents the maximum velocity of the undamped system.

For the nonlinear case with zero damping, the angular velocity is given by Eq. (17) as

$$\dot{\vartheta} = [P(\vartheta)]^{1/2}$$

However, letting $\eta \to 0$ in Eq. (26), the angular velocity is

$$\dot{\vartheta} = -\alpha_0\omega_n \sin \omega_n t$$

which in general will not equal $[P(\vartheta)]^{1/2}$. The maximum value of $\dot{\vartheta}$ for the undamped nonlinear system is obtained when ϑ is equal to zero in Eq. (17),

$$\dot{\vartheta}_{max.} = [G(\alpha_0)]^{1/2}$$

For the linear system, the maximum value of $\dot{\vartheta}$ is

$$\dot{\vartheta}_{max.} = |\alpha_0\omega_n|$$

Hence, if the quantity $-\alpha_0\omega_n$ in Eq. (26) is replaced by $[G(\alpha_0)]^{1/2}$, the approximate expression for $\dot{\vartheta}$ becomes

$$\dot{\vartheta} = [G(\alpha_0)]^{1/2}(\omega_n/\omega)e^{-(\eta/2)t} \sin \omega t \qquad (27)$$

which in the limit as $\eta \to 0$ becomes

$$\dot{\vartheta} = [G(\alpha_0)]^{1/2} \sin \omega_n t$$

It should be noted that the expression for $\dot{\vartheta}$ given by Eq. (27) is not the time derivative of the approximate solution for ϑ given by Eq. (24), but it has the same general character and gives the proper value of $\dot{\vartheta}_{max.}$ in the limit as $\eta \to 0$. Because the approximate value of $\dot{\vartheta}(t)$ obtained in this way is not the time derivative of the approximate value of $\vartheta(t)$, the functions $\dot{\vartheta}(t)$ and $\vartheta(t)$ should be treated as unrelated functions.

Since $g(\vartheta)$ is, in general, nonconstant, it is clear that the appropriate value of ω_n will be a function of the amplitude of the oscillation. If the system is not conservative—i.e., $f(\vartheta) \not\equiv 0$—this amplitude will change with time, and after time t_2 its magnitude is given by

$$|\vartheta_1'| = |\alpha_0(\omega_n/\omega)|\, e^{-(\eta/2)t}$$

The general procedure outlined above can be continued for another interval $\vartheta_1' \leq \vartheta \leq \vartheta_2$, using the reduced value of the oscillation amplitude to determine the value of ω_n and modifying the procedure to account for the different initial conditions for the second interval, since $\dot{\vartheta}(t_2)$ will, in general, not be zero. This solution will be valid for $t_2 \leq t \leq t_3$. Following this step-by-step process, the solution can be continued, and, by selecting the intervals of time sufficiently small, the approximate solution can presumably be made to differ from the exact solution by as little as desired. Furthermore, the approximate solution for the undamped case given by Eqs. (24) and (27) by letting $\eta \to 0$ and the exact solution in the undamped case given by Eqs. (17) and (18) agree at $t = 0$ and at $t = t_2$ irrespective of the magnitude of t_2. This suggests, by analogy to the damped linear system, that in the case of small damping the approximate solutions should be reasonably good for fairly large values of t_2.

It is convenient to select t_2 such that $\vartheta_1 = 0$, since this simplifies the initial conditions for the next interval. With this choice of t_2, the approximate solution can be written, for $0 \leq t \leq t_2$, $\alpha_0 \leq \vartheta \leq 0$,

$$\vartheta = \alpha_0 \left(\frac{\omega_n}{\omega}\right) e^{-(\eta/2)t} \cos(\omega t - \Omega) \qquad (28)$$

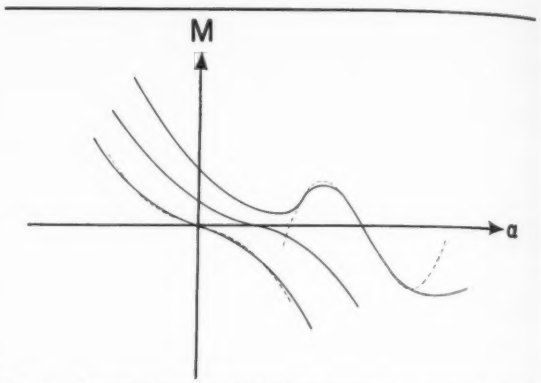

FIG. 3. General character of pitching moment vs. angle of attack for missile "A."

$$\vartheta = [G(\alpha_0)]^{1/2}\left(\frac{\omega_n}{\omega}\right) e^{-(\eta/2)t} \sin \omega t \qquad (29)$$

where

$$\omega_n = \frac{\pi/2}{\displaystyle\int_{\alpha_0}^{0} \frac{dx}{[P(x)]^{1/2}}} \qquad (30)$$

$$\eta = \frac{4}{\pi}\int_0^{\pi/2} f(\alpha_0 \cos y) \sin^2 y\, dy \qquad (31)$$

$$\omega = [\omega_n^2 - (\eta/2)^2]^{1/2} \qquad (32)$$

$$\Omega = \tan^{-1}(\eta/2\omega) \qquad (33)$$

and when

$$t = t_2 = [(\pi/2) + \Omega]/\omega$$

$$\dot{\vartheta}(t_2) = [G(\alpha_0)]^{1/2}\left(\frac{\omega_n}{\omega}\right)e^{-(\eta/2)\{[(\pi/2)+\Omega]/\omega\}} \sin\left(\frac{\pi}{2} + \Omega\right)$$

$$\alpha_1 = \alpha_0 e^{-(\eta/2)\{[(\pi/2)+\Omega]/\omega\}}$$

For the next interval, it is convenient to choose t_3 such that $\dot{\vartheta}$ varies from $\dot{\vartheta}(t_2)$ to 0. This gives the new values of ω_n and η,

$$\omega_{n_1} = \frac{\pi}{2}\Big/\int_0^{\delta_1} \frac{dx}{[P(x)]^{1/2}}$$

$$\eta_1 = \frac{4}{\pi}\int_0^{\pi/2} f(\alpha_1 \cos y) \sin^2 y\, dy$$

where δ_1 is the amplitude of the peak of the undamped oscillation on the opposite side of zero from α_1. Hence $G(\delta_1) = G(\alpha_1)$. If $g(\vartheta)\vartheta$ is an odd function of ϑ, then $\delta_1 = \alpha_1$.

Letting $\tau = t - t_2$, where $t = 0$ corresponds to $\vartheta = \alpha_0$, $\dot{\vartheta} = 0$, the second interval of the oscillation is given by

$$\vartheta = \delta_1\left(\frac{\omega_{n_1}}{\omega_1}\right) e^{-(\eta_1/2)\tau} \sin \omega_1\tau$$

$$\dot{\vartheta} = \dot{\vartheta}(t_2)\left(\frac{\omega_{n_1}}{\omega_1}\right) e^{-(\eta_1/2)\tau} \cos(\omega_1\tau + \Omega_1)$$

where

$$\omega_1 = [\omega_n^2 - (\eta_1/2)^2]^{1/2}$$

$$\Omega_1 = \tan^{-1}[(\eta_1/2)/\omega_1]$$

The process is then continued for a third interval such that ϑ varies from $\vartheta(t_3)$ to 0; hence, this interval is exactly similar to the first. The fourth interval is similar to the second, etc.

The procedure outlined above can be followed for any reasonable functions $f(\vartheta)$ and $g(\vartheta)$, provided the amplitude of the oscillations considered is such that the system is stable. It is found in practice that the pitching moment vs. angle of attack, which determines the function $g(\vartheta)\vartheta$, can be satisfactorily represented by a cubic polynomial. This has the advantage of leading to elliptic integrals of the first kind for the determination of ω_n, and these functions are tabulated. If higher order polynomials are used, the integrals will have to be computed.

Seven representative numerical examples have been worked out by the method outlined above. These were taken from actual missile configurations and include high- and low-altitude operation at different Mach Numbers and angles of attack. The initial conditions were chosen to correspond to step-function control-surface deflections necessary for turns of the order of from 1 to 5 g's. The general character of the moment and lift curves vs. angle of attack, together with their mathematical approximations by cubic polynomials, is presented in Figs. 3, 4, and 5.

The seven examples can be described by the values of the coefficients A, B, C, D, E, and F and the initial displacement α_0. These are presented in Table 2.

The details of the calculations for these cases are presented in Appendix (I). The results of the analysis in comparison with numerical integrations obtained by IBM punched card techniques and the classical linearized solution are presented in two ways. The responses in both ϑ and $\dot{\vartheta}$ are plotted against time and are presented alternately with the appropriate plots of the restoring moment $-g(\vartheta)\vartheta$ and the damping function $f(\vartheta)$ against displacement in Figs. 6a to 12b. Phase space diagrams on which the trajectories of the solutions are plotted are presented in Figs. 13 to 19.

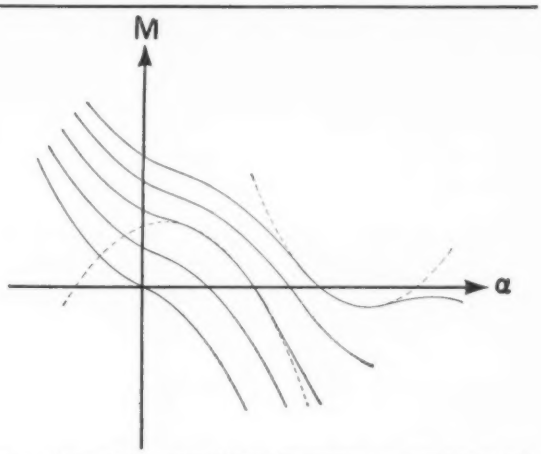

FIG. 4. General character of pitching moment vs. angle of attack for missile "B."

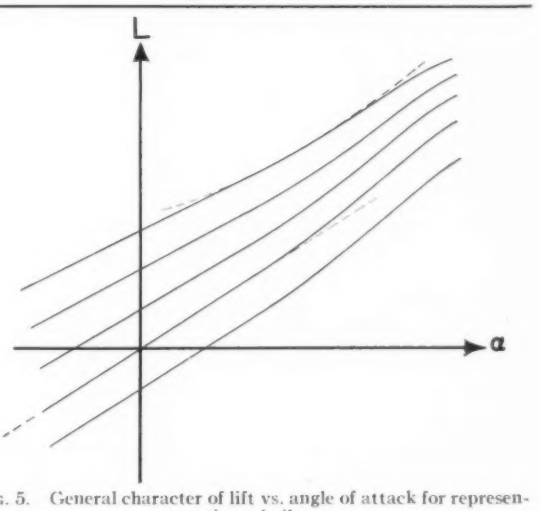

FIG. 5. General character of lift vs. angle of attack for representative missiles.

(IV) CONCLUSION

The response to a sudden angle of attack in the case of a nonlinear moment curve is found to be qualitatively similar to that for a linear moment curve, though quantitatively the difference is marked. This difference in the examples treated, which are considered to be representative, indicates that the classical linearized solution in such cases leads to large errors. The approximate solution derived gives results that are consider-

TABLE 2

Values of the Coefficients in the Nonlinear Equation of Motion [Eq. (39)] and Initial Displacement for the Seven Examples Considered

	Damping Function Coefficients			Restoring Moment Coefficients			Initial Displacement
	A	B	E	C	D	F	
Missile "A"							
Example I	10.0	0	17.0	120	0	17,000	−0.10
Example II	1.32	0	2.24	14	0	1,950	−0.10
Example III	9.0	3.5	0	700	1,300	−74,800	−0.08
Example IV	1.3	0.5	0	80	150	−8,600	−0.08
Missile "B"							
Example V	2.65	1.0	0	60	300	0	−0.10
Example VI	5.1	2.0	0	172	−1,580	0	−0.10
Example VII	0.37	0	0	11	−102	0	−0.05

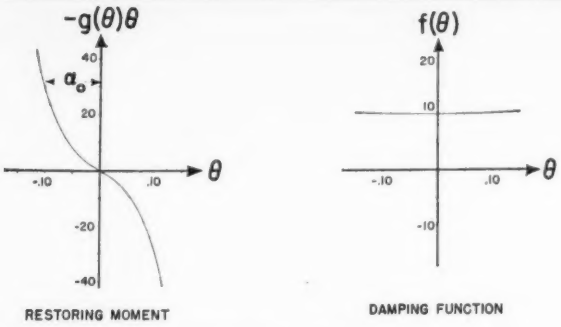

FIG. 6a. Restoring moment and damping function vs. incremental angle of attack. Example I.

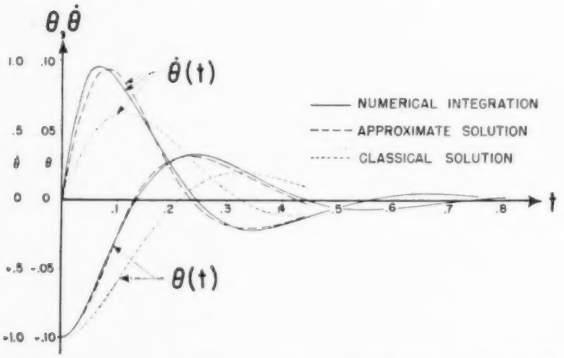

FIG. 6b. Dynamic response to step-function input in angle of attack. Example I.

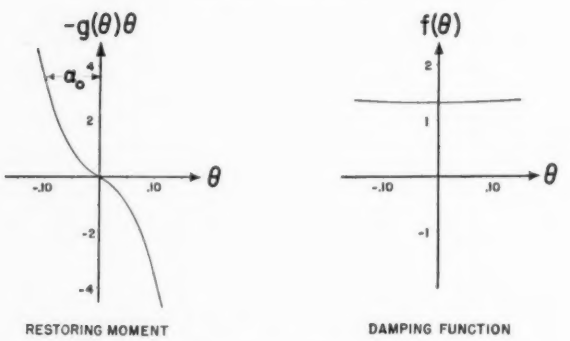

FIG. 7a. Restoring moment and damping function vs. incremental angle of attack. Example II.

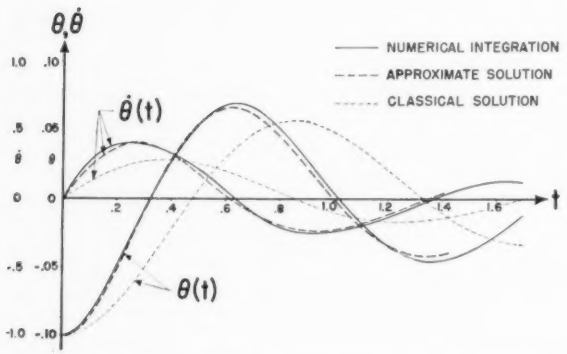

FIG. 7b. Dynamic response to step-function input in angle of attack. Example II.

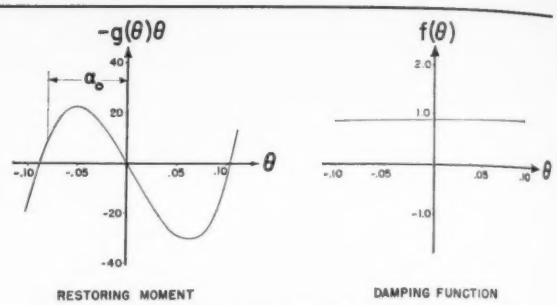

FIG. 8a. Restoring moment and damping function vs. incremental angle of attack. Example III.

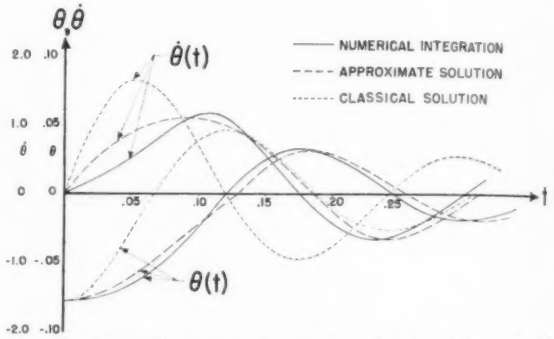

FIG. 8b. Dynamic response to step-function input in angle of attack. Example III.

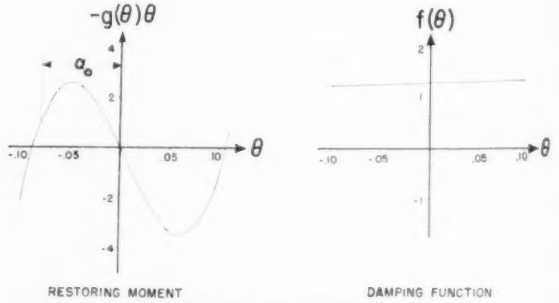

FIG. 9a. Restoring moment and damping function vs. incremental angle of attack. Example IV.

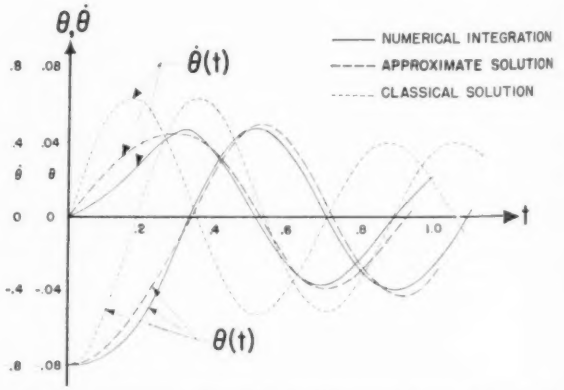

FIG. 9b. Dynamic response to step-function input in angle of attack. Example IV.

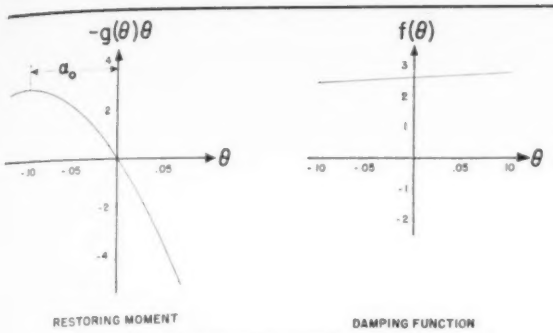

FIG. 10a. Restoring moment and damping function vs. incremental angle of attack. Example V.

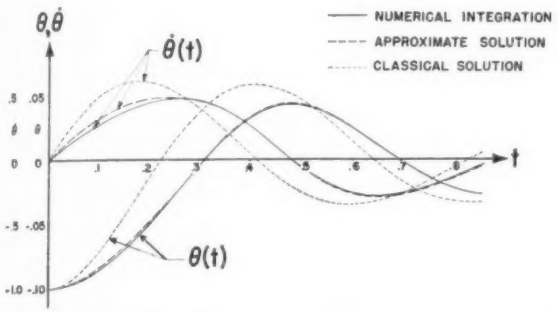

FIG. 10b. Dynamic response to step-function input in angle of attack. Example V.

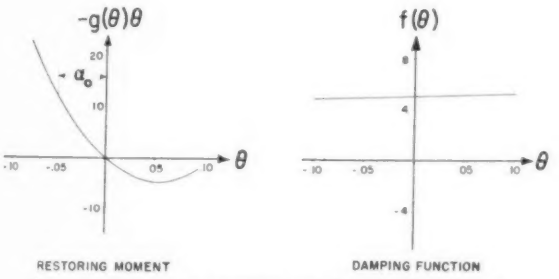

FIG. 11a. Restoring moment and damping function vs. incremental angle of attack. Example VI.

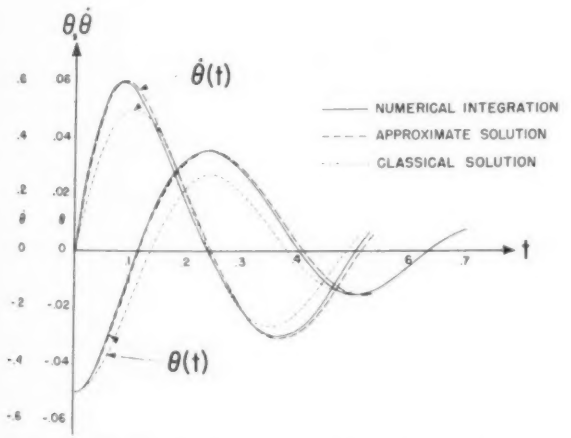

FIG. 11b. Dynamic response to step-function input in angle of attack. Example VI.

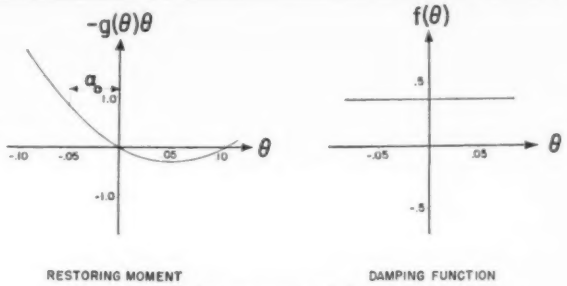

FIG. 12a. Restoring moment and damping function vs. incremental angle of attack. Example VII.

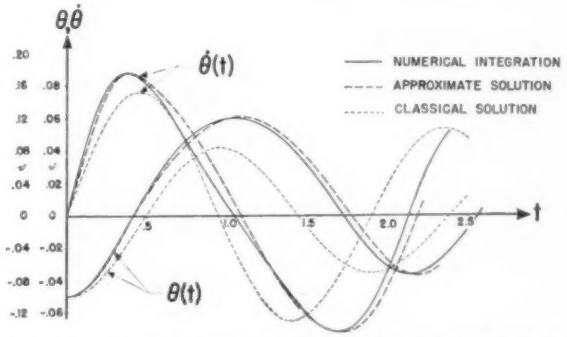

FIG. 12b. Dynamic response to step-function input in angle of attack. Example VII.

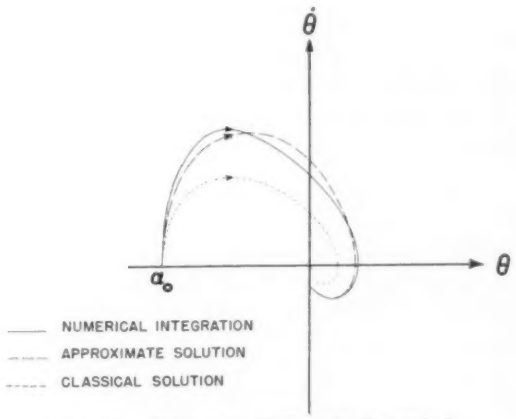

FIG. 13. Phase space diagram for Example I.

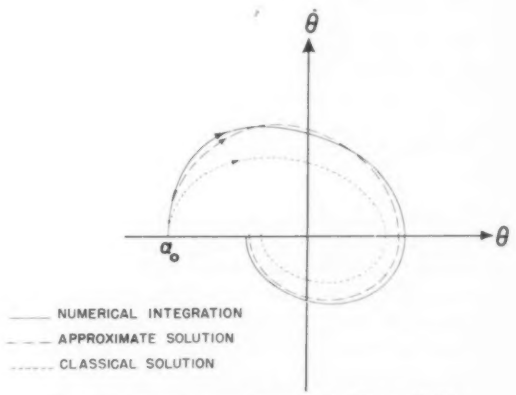

FIG. 14. Phase space diagram for Example II.

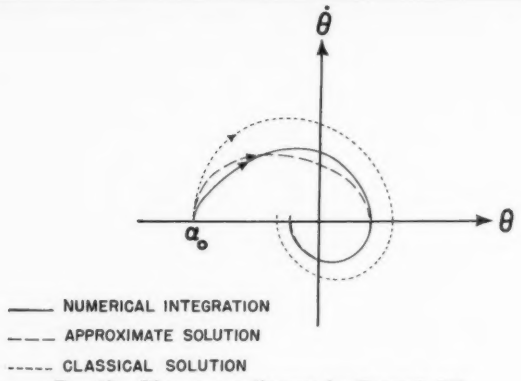

FIG. 15. Phase space diagram for Example III.

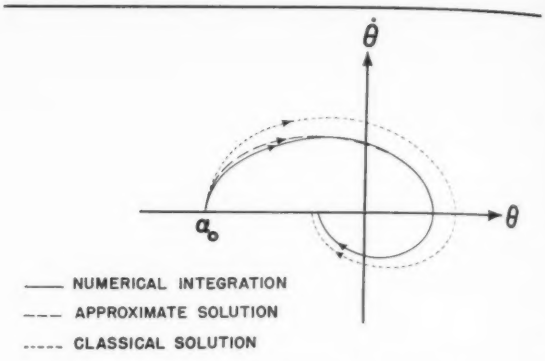

FIG. 17. Phase space diagram for Example V.

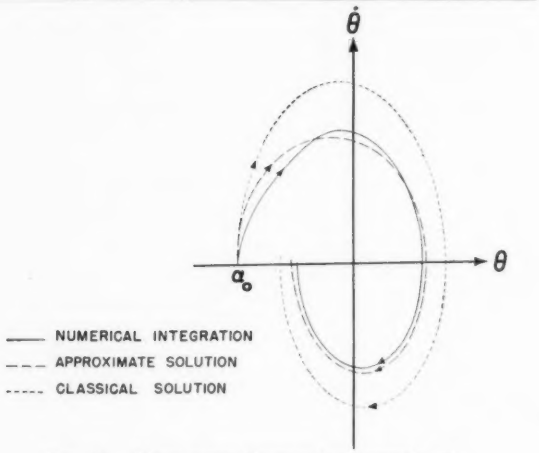

FIG. 16. Phase space diagram for Example IV.

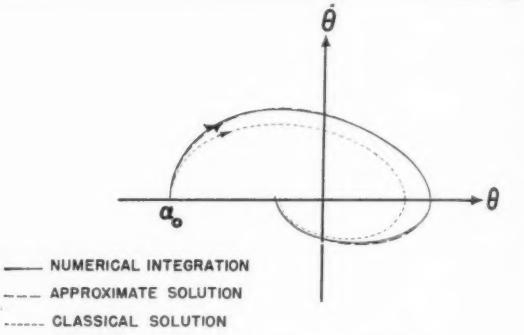

FIG. 18. Phase space diagram for Example VI.

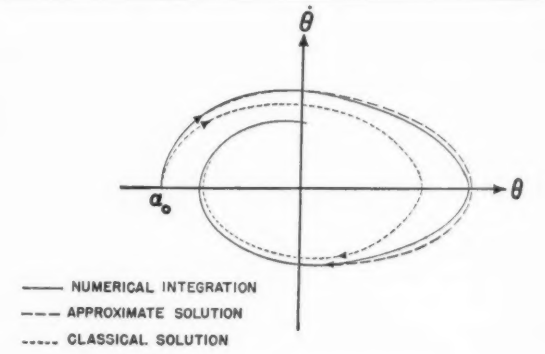

FIG. 19. Phase space diagram for Example VII.

ably more representative of the actual behavior and appears to be adequate for design purposes. If extreme accuracy is required, the methods of numerical integration should be used.

APPENDIX (I)

Application of Approximate Method of Solution to Specific Examples

In the application of the approximate method developed to actual cases it is assumed that $f(\vartheta) = A + B\vartheta + E\vartheta^2$ and that $g(\vartheta) = C + D\vartheta + F\vartheta^2$. The determination of the effective damping constant is straightforward by application of Eq. (31), and the result is

$$\eta = A + (4B/3\pi)\alpha_0 + (E/4)\alpha_0^2$$

The algebra in the determination of ω_n varies somewhat depending on the values of C, D, and F. The different cases encountered in the examples cited in this paper are treated separately below.

Case I.—(Examples I and II): $D = 0$; $C, F > 0$, $\alpha_0 < 0$; hence,

$$g(\vartheta) = C + F\vartheta^2 \tag{I.1}$$

From Eq. (16),

$$\left.\begin{aligned} P(\vartheta) = \dot{\vartheta}^2 &= -2\int_{\alpha_0}^{\vartheta} (Cx + Fx^3)\,dx \\ P(\vartheta) &= \frac{F}{2}(\alpha_0^2 - \vartheta^2)\left(\frac{2C}{F} + \alpha_0^2 + \vartheta^2\right) \end{aligned}\right\} \tag{I.2}$$

Let $\zeta = \vartheta/\alpha_0$ and $a^2 = \alpha_0^2/[\alpha_0^2 + (2C/F)]$, then $0 < a^2 < 1$. Now Eq. (I.2) becomes

$$P(\vartheta) = \alpha_0{}^2 P_1(\zeta) = \frac{\alpha_0{}^2 F}{2}\left(\alpha_0{}^2 + \frac{2C}{F}\right)(1-\zeta^2)(1+a^2\zeta^2)$$

and

$$\int_{\infty}^{0} \frac{dx}{[P(x)]^{1/2}} = \frac{1}{[(F/2)\alpha_0{}^2 + C]^{1/2}} \times \int_0^1 \frac{d\zeta}{[(1-\zeta^2)(1+a^2\zeta^2)]^{1/2}}$$

Let $\zeta = \cos\varphi$,

$$\int_{\infty}^{0} \frac{dx}{[P(x)]^{1/2}} = \frac{1}{(C + F\alpha_0{}^2)^{1/2}} \times \int_0^{\pi/2} \frac{d\varphi}{(1 - k^2\sin^2\varphi)^{1/2}} = \frac{K(\psi)}{(C + F\alpha_0{}^2)^{1/2}}$$

where

$$\psi = \sin^{-1} k = \sin^{-1}\left(\frac{F\alpha_0{}^2}{2F\alpha_0{}^2 + 2C}\right)^{1/2}$$

and $K(\psi)$ is the complete elliptic integral of the first kind. From Eq. (30),

$$\omega_n = (\pi/2)\,(C + F\alpha_0{}^2)^{1/2}/K(\psi)$$

The approximate solution for the first interval $0 \leq t \leq T_1$, $\alpha_0 \leq \vartheta \leq 0$ is given by

$$\varphi = \alpha_0\left(\frac{\omega_{n_0}}{\omega_0}\right) e^{-(\eta_0/2)t}\cos(\omega_0 t - \Omega_0) \qquad (I.3)$$

$$\dot{\vartheta} = \dot{\vartheta}_{M_0}\left(\frac{\omega_{n_0}}{\omega_0}\right) e^{-(\eta_0/2)t}\sin\omega_0 t \qquad (I.4)$$

where the constants are given by the following equations on setting $i = 0$:

$$\omega_{n_i} = (\pi/2)\,(C + F\alpha_i{}^2)^{1/2}/K(\psi_i) \qquad (I.5)$$

$$\psi_i = \sin^{-1}[F\alpha_i{}^2/(2F\alpha_i{}^2 + 2C)]^{1/2} \qquad (I.6)$$

$$\eta_i = A + (4B/3\pi)\alpha_i + (E/4)\alpha_i{}^2 \qquad (I.7)$$

$$\omega_i = [\omega_{n_i}{}^2 - (\eta_i/2)^2]^{1/2} \qquad (I.8)$$

$$\Omega_i = \tan^{-1}[(\eta_i/2)/\omega_i] \qquad (I.9)$$

$$\dot{\vartheta}_{M_i} = [C\alpha_i{}^2 + (2D/3)\alpha_i{}^3 + (F/2)\alpha_i{}^4]^{1/2} \qquad (I.10)$$

Now T_1 is the value of t when $\vartheta = 0$; hence,

$$T_1 = [(\pi/2) + \Omega_0]/\omega_0 \qquad (I.11)$$

$$\dot{\vartheta}(T_1) = \dot{\vartheta}_{M_0} e^{-(\eta_0/2)T_1} \qquad (I.12)$$

$$\alpha_1 = -\alpha_0 e^{-(\eta_0/2)T_1} \qquad (I.13)$$

Since $g(\vartheta)\vartheta = C\vartheta + F\vartheta^3$, which is an odd function of ϑ, the amplitude of oscillation for the undamped system is symmetrical with respect to $\vartheta = 0$. The solution for the second interval, $T_1 \leq t \leq T_2$, $\dot{\vartheta}(T_1) \geq \dot{\vartheta} \geq 0$, $0 \leq \vartheta \leq \alpha_2$, is given by the following equations, where $\tau = t - T_1$:

$$\vartheta = \alpha_1\left(\frac{\omega_{n_1}}{\omega_1}\right) e^{-(\eta_1/2)\tau}\sin\omega_1\tau \qquad (I.14)$$

$$\dot{\vartheta} = \dot{\vartheta}(T_1)\left(\frac{\omega_{n_1}}{\omega_1}\right) e^{-(\eta_1/2)\tau}\cos(\omega_1\tau + \Omega_1) \qquad (I.15)$$

The constants are given by Eqs. (I.5) through (I.9) on setting $i = 1$. Now T_2 is the value of t when $\vartheta = 0$; hence,

$$T_2 = T_1 + \{[(\pi/2) - \Omega_1]/\omega_1\} \qquad (I.16)$$

$$\alpha_2 = \alpha_1 e^{-\eta_1/2)(T_2 - T_1)} \qquad (I.17)$$

For the third interval, $T_2 \leq t \leq T_3$, $\alpha_2 \geq \vartheta \geq 0$, the solution is given by the following equations, where $\tau = t - T_2$:

$$\vartheta = \alpha_2[\omega_{n_2}/\omega_2)e^{-(\eta_2/2)\tau}\cos(\omega_2\tau - \Omega_2) \qquad (I.18)$$

$$\dot{\vartheta} = \dot{\vartheta}_{M_2}(\omega_{n_2}/\omega_2)e^{-(\eta_2/2)\tau}\sin\omega_2\tau \qquad (I.19)$$

the constants being given by Eqs. (I.5) through (I.10) on setting $i = 2$. Now T_3 is the value of t when $\vartheta = 0$; hence,

$$T_3 = T_2 + \{[(\pi/2) + \Omega_2]/\omega_2\} \qquad (I.20)$$

$$\dot{\vartheta}(T_3) = \dot{\vartheta}_{M_2} e^{-(\eta_2/2)(T_3 - T_2)} \qquad (I.21)$$

$$\alpha_3 = -\alpha_2 e^{-(\eta_2/2)(T_3 - T_2)} \qquad (I.22)$$

For the fourth interval, $T_3 \leq t \leq T_4$, $\dot{\vartheta}(T_3) \leq \dot{\vartheta} \leq 0$, $0 \geq \vartheta \geq \alpha_4$, the solution is given by the following equations, where $\tau = t - T_3$:

$$\vartheta = \alpha_3(\omega_{n_3}/\omega_3)e^{-(\eta_3/2)\tau}\sin\omega_3\tau \qquad (I.23)$$

$$\dot{\vartheta} = \dot{\vartheta}(T_3)\,(\omega_{n_3}/\omega_3)e^{-(\eta_3/2)\tau}\cos(\omega_3\tau + \Omega_3) \qquad (I.24)$$

the constants being given by Eqs. (I.5) through (I.9) on setting $i = 3$. Now T_4 is the value of t when $\dot{\vartheta} = 0$; hence,

$$T_4 = T_3 + \{[(\pi/2) + \Omega_3]/\omega_3\} \qquad (I.25)$$

$$\alpha_4 = \alpha_3 e^{-(\eta_3/2)(T_4 - T_3)} \qquad (I.26)$$

The solution for the next four intervals is obtained in exactly the same way as for the first four.

Case II.—(Examples III and IV): C, $D > 0$; F, $\alpha_0 < 0$; hence,

$$g(\vartheta) = C + D\vartheta + F\vartheta^2$$

From Eq. (16),

$$P(\vartheta) = -2\int_{\alpha_0}^{\vartheta}(Cx + Dx^2 + Fx^3)\,dx$$

$$P(\vartheta) = \frac{-F}{2}(\vartheta - \alpha_0)(\vartheta^3 + b\vartheta^2 + c\vartheta + d) \qquad (I.27)$$

where

$$b = \alpha_0 + (4D/3F)$$

$$c = \alpha_0{}^2 + (4D/3F)\alpha_0 + (2C/F)$$

$$d = \alpha_0{}^3 + (4D/3F)\alpha_0{}^2 + (2C/F)\alpha_0 \qquad (I.28)$$

Factoring,

$$P(\vartheta) = (-F/2)(\vartheta - \alpha_0)(\vartheta - \beta_0)(\vartheta - \gamma_0)(\vartheta - \delta_0)$$

where β_0, γ_0, δ_0 are the roots of the cubic,

$$\vartheta^3 + b\vartheta^2 + c\vartheta + d = 0$$

Since the system is stable under the given initial conditions, β_0, γ_0, δ_0 are real, $\beta_0 < \alpha_0 < 0 < \delta_0 < \gamma_0$, and the oscillation in ϑ is in the interval $\alpha_0 \leq \vartheta \leq \delta_0$. Now

$$\int_{\alpha_0}^{0} \frac{dx}{[P(x)]^{1/2}} = \frac{1}{(-F/2)^{1/2}} \times \int_{\alpha_0}^{0} \frac{dx}{[(x-\alpha_0)(x-\beta_0)(x-\gamma_0)(x-\delta_0)]^{1/2}} \tag{I.29}$$

$$= \frac{2}{[(-F/2)(\alpha_0-\gamma_0)(\beta_0-\delta_0)]^{1/2}} \times \int_0^{\varphi_0} \frac{d\varphi}{(1-k_0^2\sin^2\varphi)^{1/2}}$$

$$= \frac{2\mathfrak{F}\{\psi_0, \varphi_0\}}{[(-F/2)(\alpha_0-\gamma_0)(\beta_0-\delta_0)]^{1/2}} \tag{I.30}$$

where

$$\psi_0 = \sin^{-1} k_0 = \sin^{-1}\left[\frac{(\alpha_0-\delta_0)(\beta_0-\gamma_0)}{(\beta_0-\delta_0)(\alpha_0-\gamma_0)}\right]^{1/2} \tag{I.31}$$

$$\varphi_0 = \sin^{-1}\left[\frac{\alpha_0(\beta_0-\delta_0)}{\beta_0(\alpha_0-\delta_0)}\right]^{1/2} \tag{I.32}$$

and $\mathfrak{F}\{\psi_0, \varphi_0\}$ is the incomplete elliptic integral of the first kind of amplitude, φ_0.

By Equation (30),

$$\omega_{n_0} = \frac{(\pi/4)[(-F/2)(\alpha_0-\gamma_0)(\beta_0-\delta_0)]^{1/2}}{\mathfrak{F}\{\psi_0, \varphi_0\}} \tag{I.33}$$

For the first interval, $0 \leq t \leq T_1$, $\alpha_0 \leq \vartheta \leq 0$, the solution is given by Eqs. (I.3) and (I.4); the constants are determined by Eqs. (I.7) through (I.10) on setting $i = 0$ and Eqs. (I.31) through (I.33). T_1 and $\dot{\vartheta}(T_1)$ are obtained from Eqs. (I.11) and (I.12), respectively. Since $g(\vartheta)\vartheta$ is not an odd function of ϑ, the amplitude of oscillation of the undamped system is not symmetrical with respect to $\vartheta = 0$. Hence, for the second interval $0 \leq \vartheta \leq \delta_1$, where δ_1 is the lesser of the two positive roots of the equation,

$$\vartheta^3 + b_1\vartheta^2 + c_1\vartheta + d_1 = 0 = (\vartheta-\beta_1)(\vartheta-\delta_1)(\vartheta-\gamma_1)$$

$$\beta_0 < \alpha_1 < 0 < \delta_1 < \gamma_1$$

The quantities b, c, and d are obtained by substituting $\alpha = \alpha_0 e^{-(\eta/2)T_1}$ for α_0 in Eqs. (I.28). Hence, for the second interval, $T_1 \leq t \leq T_2$, $\dot{\vartheta}(T_1) \geq \dot{\vartheta} \geq 0$, $0 \leq \vartheta \leq \delta_2$; letting $\tau = t - T_1$, the solution is given by Eqs. (I.14) and (I.15) where, now,

$$\omega_{n_1} = \frac{(\pi/4)[(-F/2)(\alpha_1-\gamma_1)(\beta_1-\delta_1)]^{1/2}}{K(\psi_1) - \mathfrak{F}(\psi_1, \varphi_1)} \tag{I.34}$$

φ_1, ψ_1 are determined from Eqs. (I.31) and (I.32) upon replacing α_0, β_0, γ_0, δ_0 by α_1, β_1, γ_1, δ_1, respectively, and Eqs. (I.7) through (I.10) on setting $i = 1$ apply. T_2 is obtained from Eq. (I.16), and δ_2 is now given by

$$\delta_2 = \delta_1 e^{-(\eta_1/2)(T_2-T_1)} \tag{I.35}$$

For the third interval, $T_2 \leq t \leq T_3$, $\delta_2 \geq \vartheta \geq 0$, the solution is given by Eq. (I.18) on replacing α_2 by δ_2 and Eq. (I.19). The constants are obtained on setting $i = 2$ and replacing α_2 with δ_2 in Eqs. (I.7) through (I.10); ω_{n_2} is obtained from Eq. (I.34) on replacing α_1, β_1, γ_1, δ_1, ψ_1 and φ_1 with α_2, β_2, γ_2, δ_2, ψ_2, and φ_2, respectively, ψ_2 and φ_2 being determined from Eqs. (I.31) and (I.32) upon replacing α_0, β_0, γ_0, δ_0 with α_2, β_2, γ_2, δ_2, respectively. T_3 and $\dot{\vartheta}(T_3)$ are given by Eqs. (I.20) and (I.21). For the fourth interval, $T_3 \leq t \leq T_4$, $\dot{\vartheta}(T_3) \leq \dot{\vartheta} \leq 0$, $0 \geq \vartheta \geq \alpha_4$, the solution is given by Eqs. (I.23) and (I.24). α_3 is the numerically smaller of the two negative roots of the cubic

$$\vartheta^3 + b_3\vartheta^2 + c_3\vartheta + d_3 = 0 = (\vartheta-\alpha_3) \times (\vartheta-\beta_3)(\vartheta-\gamma_3)$$

where b_3, c_3, and d_3 are obtained from Eq. (I.28) on replacing α_0 by $\delta_3 = \delta_2 e^{-(\eta/2)(T_3-T_2)}$. The constants are determined by setting $i = 3$ in Eqs. (I.7) through (I.10) and by replacing α_0, β_0, δ_0, γ_0 with α_3, β_3, δ_3, γ_3, respectively, in Eqs. (I.31) through (I.33). T_4 and α_4 are given by Eqs. (I.25) and (I.26).

Case III.—$F = 0$, $g(\vartheta) = C + D\vartheta$. Now,

$$P(\vartheta) = -2\int_{\alpha_0}^{\vartheta} (Cx + Dx^2)\,dx = (-2D/3)(\vartheta-\alpha_0)(\vartheta-\beta_0)(\vartheta-\delta_0) \tag{I.36}$$

where

$$\left.\begin{aligned} \beta_0 &= \frac{-[\alpha_0 + (3C/2D)]}{2} \times \left\{1 + \left[1 - \frac{4\alpha_0}{\alpha_0 + (3C/2D)}\right]^{1/2}\right\} \\ \delta_0 &= \frac{-[\alpha_0 + (3C/2D)]}{2} \times \left\{1 - \left[1 - \frac{4\alpha_0}{\alpha_0 + (3C/2D)}\right]^{1/2}\right\} \end{aligned}\right\} \tag{I.37}$$

Since the system is stable under the chosen initial conditions, β_0 and δ_0 are real.

Case IIIa.—(Example V): If C, $D > 0$, $\beta_0 < \alpha_0 < 0$, $\delta_0 > 0$, the solution is obtained in the same way as in Case II with the exceptions that: Eq. (I.33) is replaced by

$$\omega_{n_0} = \frac{(\pi/4)[(2D/3)(\delta_0-\beta_0)]^{1/2}}{\mathfrak{F}\{\psi_0, \varphi_0\}} \tag{I.38}$$

Eq. (I.31) is replaced by

$$\psi_0 = \sin^{-1}[(\delta_0-\alpha_0)/(\delta_0-\beta_0)]^{1/2} \tag{I.39}$$

and Eq. (I.34) is replaced by

$$\omega_{n_1} = \frac{(\pi/4)\ [(2D/3)\ (\delta_1 - \beta_1)]^{1/2}}{\{K(\psi_1) - \mathfrak{F}\{\psi_1, \varphi_1\}} \tag{I.40}$$

Case IIIb.—(Examples VI and VII): If $C > 0$, $D < 0$, $\beta_0 > \delta_0 > 0$, $\alpha_0 < 0$, the solution is obtained in the same way as Case II with the exceptions that: Eq. (I.33) is replaced by

$$\omega_{n_0} = \frac{(\pi/4)\ [-(2D/3)\ (\beta_0 - \alpha_0)]^{1/2}}{\mathfrak{F}\{\psi_0, \varphi_0\}} \tag{I.41}$$

Eq. (I.31) is replaced by

$$\psi_0 = \sin^{-1}\left(\frac{\delta_0 - \alpha_0}{\beta_0 - \alpha_0}\right)^{1/2} \tag{I.42}$$

Eq. (I.32) is replaced by

$$\varphi_0 = \sin^{-1}\left(\frac{-\alpha_0}{\delta_0 - \alpha_0}\right)^{1/2} \tag{I.43}$$

and Eq. (I.34) is replaced by

$$\omega_{n_1} = \frac{(\pi/4)\ [-(2D/3)\ (\beta_1 - \alpha_1)]^{1/2}}{K(\psi_1) - \mathfrak{F}(\psi_1, \varphi_1)} \tag{I.44}$$

Appendix (II)

Effect of Nonlinear Pitching Moment Curves on the Determination of Stability Derivatives from Flight-Test Data

One of the techniques used for the determination of stability derivatives from flight-test data is the analysis of the transient response to a step-function input in control-surface deflection. It is customary to assume a linear system. From a measurement of the amplitude of the oscillation vs. time, the logarithmic decrement is determined. The zeros of the oscillation determine the damped natural frequency. The combination of these two then defines the undamped natural frequency, which to all practical purposes determines the quantity

$$M_w' = (q'Sc/I_y)\ (dC_M/d\alpha)$$

If the moment curve is a nonlinear function of the angle of attack, the "frequency" of the oscillation varies with the amplitude. In this case, the usual procedure of measuring the zeros of the oscillation and averaging them will not determine the value of $dC_M/d\alpha$ at the trim position but some sort of average value. The comparison of the classical linearized solution with the numerical integration for the seven examples considered in this paper clearly indicates that the value of $dC_M/d\alpha$ obtained in the usual way will not be very meaningful if the nonlinearity is at all severe.

Alternatively, an attempt to determine the nonlinear moment curve, using the approximate solution for the response, may be made. The procedure to be outlined requires that angle of attack, normal acceleration in the pitch plane, and pitch rate be measured as functions of time and assumes, of course, a knowledge of Mach Number, velocity, and dynamic pressure in order that the moment curve may be reduced to coefficient form. In addition, it is necessary to assume the general shape of the moment curve. (This is analogous to the assumption of linearity usually made.)

Consider first a moment curve of the form

$$-g(\vartheta)\vartheta = -(C + F\vartheta^2)\vartheta; \quad C, F > 0$$

Assume also that the damping function is constant, $f(\vartheta) = \eta$. From the records of angle of attack vs. time, normal acceleration vs. time, and pitch rate vs. time, the damping constant can be determined. The initial amplitude, α_0, of the oscillation in angle of attack is also measured. Designating T_1 as the first zero of ϑ and using Eq. (I.11),

$$\omega_0 = [(\pi/2) + \Omega_0]/T_1$$

where $\Omega_0 = \tan^{-1}[(\eta/2)/\omega_0]$. If the damping is small compared to critical damping, Ω_0 may be determined as $\Omega_0 = (\eta/2)/\omega_{n_0}$, and ω_{n_0} can then be determined from

$$\omega_{n_0} = \frac{\pi}{4T_1} + \left[\left(\frac{\pi}{4T_1}\right)^2 + \frac{\eta/2}{T_1} + \frac{(\eta/2)^2}{2}\right]^{1/2}$$

η, ω_{n_0} and α_0 are determined and can be substituted in Eq. (I.5),

$$\omega_{n_0} = (\pi/2)\ (F\alpha_0^2 + C)^{1/2}/K(\psi_0)$$

where

$$\psi_0 = \sin^{-1}[F\alpha_0^2/(2F\alpha_0^2 + 2C)]^{1/2}$$

which determines a relation between F and C.

Now the normal accelerometer measures the quantity

$$n = \dot{w} - U_1\dot{\theta} - g\cos\Theta_1$$

where $\dot{\theta}$ is the pitch rate. Hence, from the normal acceleration and pitch rate records, the quantity

$$\dot{\vartheta} = (n/U) + \dot{\theta} + (g/U)\cos\Theta_1$$

is determined as a function of time. Designating T_2 as the first zero of $\dot{\vartheta}$ and proceeding in the same manner as before, using now Eq. (I.16) instead of Eq. (I.11),

$$\omega_{n_1} = \frac{\pi}{4(T_2 - T_1)} + \left[\left(\frac{\pi}{4(T_2 - T_1)}\right)^2 - \frac{\eta/2}{(T_2 - T_1)} + \frac{(\eta/2)^2}{2}\right]^{1/2}$$

and a second relation between F and C is determined from the equations

$$\omega_{n_1} = (\pi/2)\ (F\alpha_1^2 + C)^{1/2}/K\psi_1$$

$$\psi_1 = \sin^{-1}[F\alpha_1^2/(2F\alpha_1^2 + 2C)]^{1/2}$$

$$\alpha_1 = \alpha_0 e^{-(\eta/2)T_1}$$

Following this same procedure for the subsequent zeros of the oscillations in ϑ and $\dot{\vartheta}$, additional relations between C and F can be obtained. If C is plotted

against F, these various curves will intersect each other. Since the equations used to obtain the relations between C and F are only approximate, it cannot be expected that all of the curves will intersect in a common point. However, depending on the accuracy of the data, they should define a small closed region in the F, C plane, and any point (F, C) in this region may be used for the approximate values of F and C.

As a second example of the application of the approximate solution to the determination of the moment curve, assume the curve to be of the form

$$-g(\vartheta)\vartheta = -(C\vartheta + D\vartheta^2), \quad C, D > 0$$

and assume that the damping is constant.

From the envelope of the angle of attack vs. time record, α_0 and δ_0 are determined as the initial values of the amplitude on opposite sides of $\vartheta = 0$. Proceeding as before, using now Eq. (I.38),

$$\omega_{n_0} = \frac{(\pi/4)\,[(2D/3)\,(\delta_0 - \beta_0)]^{1/2}}{\mathfrak{F}\{\psi_0, \varphi_0\}}$$

$$\psi_0 = \sin^{-1}\,[(\delta_0 - \alpha_0)/(\delta_0 - \beta_0)]^{1/2}$$

$$\varphi_0 = \sin^{-1}\left(\frac{\alpha_0(\beta_0 - \delta_0)}{\beta_0(\alpha_0 - \delta_0)}\right)^{1/2}$$

Observing that

$$P(\vartheta) = \frac{-2D}{3}\,(\vartheta - \alpha_0)\,(\vartheta - \beta_0)\,(\vartheta - \delta_0) = \frac{-2D}{3}\left(\vartheta^3 + \frac{3C}{2D}\,\vartheta^2 - \alpha_0{}^3 - \frac{3C}{2D}\,\alpha_0{}^2\right)$$

and comparing coefficients $\beta_0 = \alpha_0\delta_0/(\alpha_0 - \delta_0)$ and $3C/2D = \alpha_0 + \beta_0 - \delta_0$. This determines D and C. Repeating the procedure for the other zeros of ϑ and $\dot{\vartheta}$, additional determination of C and D may be made. An average of the different values may then be used as the correct values of C and D.

Obviously, a similar procedure can be used for other assumptions of the moment curve shape.

It is to be emphasized that the above procedure applied to a nonlinear system, since it is based on an approximate solution, cannot be expected to give results so accurate as those obtained for a linear system where the exact solution is known. However, it should yield a more useful result for a nonlinear system than that obtained from an assumption of linearity, since it accounts, in part at least, for the nonlinearity. Furthermore, this method has the advantage in actual application that large amplitude oscillations may be used; hence, the effect of instrument errors is reduced. In the application of the proposed method, there are several sources of error which are to be guarded against. The first case discussed, where the moment curve was assumed to be symmetric with respect to the origin, applies to the case of a symmetric missile trimmed at zero angle of attack. Consequently, the abscissa of the various instrument records is accurately known (after correction of $\dot{\theta}$ and $\dot{w}$ records for effect of gravity, which is small). Furthermore, after η is determined, the envelope can be faired through the peaks of the oscillation and the zero should bisect the envelope. This affords a check. Hence, the major source of error will be in the amplitudes of oscillation. Since the records from all three instruments will exhibit the same damping, all three should be used in the determination of η. The determination of $\dot{\vartheta}(t)$ requires the sum of the two instrument readings, $n(t)$ and $\dot{\theta}(t)$; hence, it cannot be expected to be so accurate as that of $\vartheta(t)$.

The case of a moment curve that is not symmetrical about the origin arises where a symmetrical missile is trimmed at a finite angle of attack. In this case, the oscillation has different amplitudes on the opposite sides from zero. The abscissa of the oscillations cannot be measured in this case and must be obtained from an extrapolation back from the steady state following the transient. This is, of course, an extremely inaccurate procedure and will undoubtedly introduce large errors.

An attempt has been made to apply the above method to the numerical solution of a case with a moment curve of the type

$$g(\vartheta)\,\vartheta = C\vartheta + D\vartheta^2$$

Errors of 10 per cent were assumed in the measured quantities, and it was found that such errors could reverse the curvature of the moment curve, though the slope of the moment curve at trim was virtually unchanged. Hence, it would appear that, in order to determine a nonlinear moment curve from flight-test data, extremely accurate instrumentation will be necessary.

References

[1] Jones, B. Melvill, *Dynamics of the Airplane;* W. F. Durand, Ed., *Aerodynamics of the Airplane,* Vol. V, Section N, 1935.

[2] Den Hartog, J. P., *Mechanical Vibrations,* 3rd Ed.; McGraw-Hill Book Company, Inc., New York, 1947.

[3] von Kármán, Theodore, and Biot, Maurice A., *Mathematical Methods in Engineering;* McGraw-Hill Book Company, Inc., New York, 1940.

[4] Kryloff, N., and Bogolinhoff, N., *Introduction to Non-Linear Mechanics;* Princeton University Press, Princeton, N.J., 1943.

[5] Stoker, J. J., *Non-Linear Vibrations in Mechnical and Electrical Systems;* Interscience Publishers, Inc., New York, 1950.

[6] Pierce, B. O., *A Short Table of Integrals,* 3rd Rev. Ed. The Athenaeum Press, Ginn and Company, Boston, 1929.

Aerodynamics of Blasts*

L. TING† AND H. F. LUDLOFF‡
New York University

ABSTRACT

The problem of a blast passing over the surface of an arbitrary flat structure is investigated. The pressure and density fields in the whole domain behind the advancing blast are obtained in explicit analytic form. As a simple example, the constant pressure lines (isobars) and the constant density lines (isopycnics) are plotted for a strong blast of pressure ratio 7.308, passing over a wedge surface. Comparison with the interferograms taken in Bleakney's laboratory shows surprising agreement. The "slip stream" connected with the Mach reflection of the shock comes out as a thin strip, in which the density gradient is steep but finite.

To obtain an analytic solution, no cone field transformations are used as previously, because they restrict the generality of the results. Instead, (a) a Lorentz transformation of the coordinates is introduced, (b) the solution is given in terms of a Possio integral, (c) a "reflection" of the boundary condition is carried out, (d) a "lost boundary condition" is taken into consideration.

SYMBOLS

A_0, A_1, A_2, A_3 = constants defined in Eq. (5.1)
$a, \bar{a}$ = constants defined in Eq. (5.1) and (6.4)
c, c_0 = sound speeds of the undisturbed flow behind and in front of the shock, respectively
$D, \bar{D}$ = differential operators defined in Eqs. (3.16) and (4.5)
f = the wall surface
M, M_0 = Mach Numbers of the undisturbed flow behind and in front of the shock
P, P_0 = the pressures of the undisturbed flow behind and in front of the shock
p = the disturbed pressure
Q = the reflected shock front (Mach circle)
S = the "separation line"
T = the triple point
t = time
$\bar{t}$ = time in the system of Lorentz coordinates
U, U_0 = the velocity of the undisturbed flow behind and in front of the shock
u = the x-component of the disturbed velocity
v = the y-component of the disturbed velocity
(x, y) = coordinates fixed on the undisturbed flow behind the shock
(x', y) = coordinates fixed on the wall
$(\bar{x}, \bar{y})$ = Lorentz coordinates
γ = 1.4 for air
θ = angle between the normal of the diffracted shock and the x-axis
$\bar{\lambda}_0, \bar{\lambda}_1, \bar{\lambda}_2, \bar{\lambda}_3$ = constants defined in Eq. (5.1)
$\lambda_0, \lambda_1, \lambda_2, \lambda_3$ = constants defined in Eq. (6.4)
R, ρ_0 = densities of the undisturbed flow behind and in front of the shock
ρ = the disturbed density
ψ = the form of the diffracted shock
$\Omega_0, \Omega_1, \Omega_2$ = constants defined in Eq. (3.15)

Received May 28, 1951.

* Thesis submitted to the Graduate Division of the College of Engineering in partial fulfillment of the requirements for the degree of Doctor of Engineering Science at New York University. Investigation was supported by the Mechanics Branch of the Office of Naval Research.

† Doctoral Candidate, Department of Aeronautical Engineering.

‡ Doctoral Adviser. Associate Professor of Aeronautical Engineering.

(I) INTRODUCTION

IN THE FOLLOWING, the pressure and density fields that develop behind blasts advancing over arbitrary flat surfaces have been investigated. Computations along similar lines have been carried out previously by Bargmann[1] (who assumed the flow field to be irrotational) and by Lighthill[2] (who took the rotationality of the flow into account). The method to be presented here is more direct, and the results obtained are more general than in the previous investigations. Shocks passing over flat surfaces of arbitrary shape can be dealt with in such a manner that explicit analytic expressions result for the pressure and density fields in the whole domain behind the advancing shock front. In this way, comparison with shock-tube experiments can be readily carried out, and interesting details about the nature of the "slip stream" occurring with the Mach reflection of the shock can be determined. [See Sections (V, 2) and (VI).]

Assume that an originally plane shock front of given intensity (strong or weak) advances over the surface $f(x')$ of a given flat structure (or a given thin airfoil) into still air of density ρ_0 and pressure P_0 (see Fig. 1). The velocity of the shock may be U_0, the speed of the air behind the shock is $(U_0 - U)$, and its density and pressure there are ρ and p. The length of the wall disturbance (or the chord of the airfoil) may be l. If the inclination of the body surface $f'(x')$ with regard to the direction of propagation of the shock is small, the shock front will end perpendicularly on the surface at any instant so that a curved shock front results, as well as a shock configuration that may be interpreted as Mach[3]

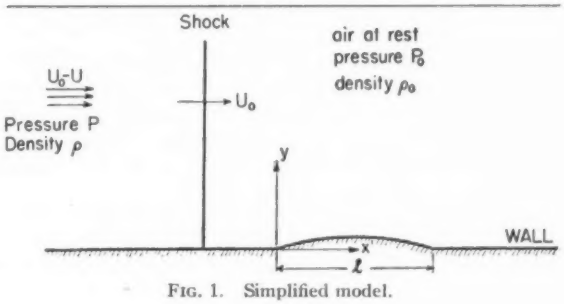

FIG. 1. Simplified model.

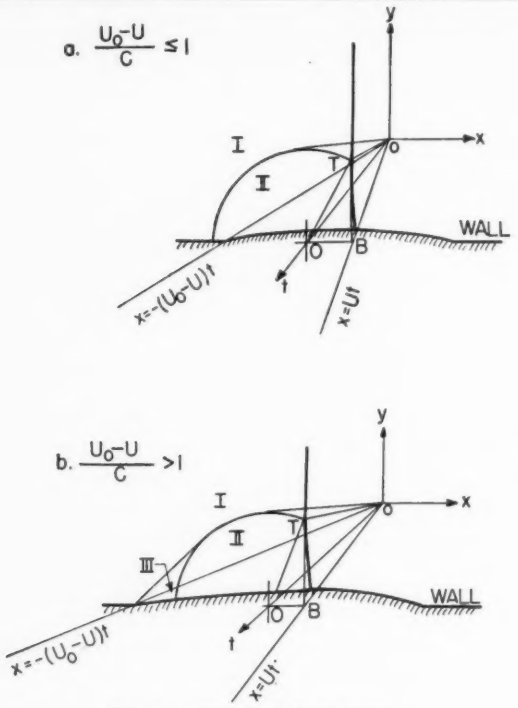

FIG. 2. Domains of disturbance.

reflection. Because of the curvature of the shock, the flow behind the diffracted part of the shock will be rotational and, for sufficiently strong blasts, supersonic with regard to the body surface. Figs. 2a and 2b represent conditions behind the advancing shock front depending on whether the airflow behind the shock is subsonic or supersonic relative to the obstacle. In either case, the time history of the diffraction is depicted in an x-y-t-space, so that every cross section of the figure represents the domain of disturbance at a given instant t, after the incident shock has hit the leading edge of the obstacle and a disturbance has spread with sound speed throughout domain II up to the circular reflected shock. The coordinate system, x, y, t, is to be fixed in the undisturbed flow behind the shock—i.e., in the flow occurring in domain I. With regard to this system, the leading edge and the whole body surface $f(x')$ are moving to the left, and the shock is moving to the right. In the subsonic case (a), the leading edge of the disturbance moves slower, and in the supersonic case (b) faster, than the perturbation produced by the shock diffraction. Therefore, in the latter case, domain III has been disturbed by the leading edge only, but it has not been reached by the shock disturbance. Hence, here Ackeret's formulas of stationary supersonic flow apply.

Conditions in domain II are clearly nonstationary. The pressure in the vicinity of the body surface must be expected to influence the speed and inclination of the shock front, and this, in turn, will affect the pressure on the body surface, so that it differs from the stationary pressure distribution. Hence, the field in domain II may be treated as a time-dependent perturbation away from the state of (relative) rest existing in domain I. A linearized theory can be derived by a formal perturbation procedure consisting essentially of an expansion in terms of a parameter ϵ, which can be interpreted as thickness ratio of the wall disturbance (or of the airfoil).

(II) The Linearized Differential Equations

Fixing the coordinates in the undisturbed flow behind the shock, the x-axis coinciding with the plane wall and the y-axis being parallel to the undisturbed shock front, the origin is so chosen that, at $t = 0$, the shock front hits the leading edge of the bump. Then, the differential equations determining the two-dimensional unsteady rotational flow behind the shock are

$$\left.\begin{aligned} &\text{the continuity equation:} && \rho_t + (\rho u)_x + (\rho v)_y = 0 \\ &\text{the equations of motion:} && \frac{Du}{Dt} = -\frac{1}{\rho} p_x; \\ & && \frac{Dv}{Dt} = -\frac{1}{\rho} p_y \\ &\text{the adiabatic relation:} && \frac{D}{Dt}(p/\rho^\gamma) = 0 \end{aligned}\right\} \quad (2.1)$$

resulting from the assumption that both viscosity and heat conduction are negligible.

Now expand p, ρ, u, and v in terms of ϵ,

$$\left.\begin{aligned} p &= P + \epsilon \cdot p^{(1)}(x, y, t) + \epsilon^2 \cdot p^{(2)}(x, y, t) + \dots \\ \rho &= R + \epsilon \cdot \rho^{(1)}(x, y, t) + \epsilon^2 \cdot \rho^{(2)}(x, y, t) + \dots \\ u &= \epsilon \cdot u^{(1)}(x, y, t) + \epsilon^2 \cdot u^{(2)}(x, y, t) + \dots \\ v &= \epsilon \cdot v^{(1)}(x, y, t) + \epsilon^2 \cdot v^{(2)}(x, y, t) + \dots \end{aligned}\right\} \quad (2.2)$$

Inserting Eqs. (2.2) into Eqs. (2.1) and equating the coefficients of like powers of ϵ, one obtains, in first approximation,

$$\rho_t^{(1)} + R \cdot u_x^{(1)} + R \cdot v_y^{(1)} = 0 \quad (2.3)$$

$$R \cdot u_t^{(1)} = -p_x^{(1)} \quad (2.4)$$

$$R \cdot v_t^{(1)} = -p_y^{(1)} \quad (2.5)$$

$$p_t^{(1)} = c^2 \cdot \rho_t^{(1)} \quad (2.6)$$

Eliminating from the above equations three out of the four unknown functions yields

$$\Box p^{(1)} = \left(\frac{\partial^2}{\partial x^2} + \frac{\partial^2}{\partial y^2} - \frac{1}{c^2}\frac{\partial^2}{\partial t^2}\right) p^{(1)} = 0 \quad (2.7)$$

and

$$(\partial/\partial t)\,(\Box g) = 0 \quad (2.8)$$

where g denotes either $u^{(1)}$, $v^{(1)}$ or $\rho^{(1)}$.

It is now necessary to find two initial conditions and one boundary condition for $p^{(1)}$ to uniquely satisfy the wave equation [Eq. (2.7)].

(III) The Boundary and Initial Conditions

(1) *On the Incident Shock Front*

Relative to the undisturbed flow behind the shock the air in front of the shock and the wall are moving with the constant velocity $-(U_0 - U)$, while the undisturbed shock front moves with the velocity $+U$.

The disturbed shock front can be expressed by the equation

$$x = Ut + \epsilon\cdot\psi^{(1)}(y, t) + 0(\epsilon^2) \tag{3.1}$$

Then, the shock inclination is given by

$$\theta = -\frac{\partial x}{\partial y} = -\epsilon\cdot\psi_y^{(1)}(y, t) + 0(\epsilon^2) \tag{3.2}$$

$$= \epsilon\cdot\theta^{(1)} + 0(\epsilon^2) \tag{3.3}$$

The complete shock velocity, which is directed normal to the shock front at any point, may be split into an x-component U_s and a y-component v_S, where[4] (see Fig. 3)

$$U_S = \frac{dx}{dt} = \frac{\partial x}{\partial t} + 0(\epsilon^2) = U + \epsilon\cdot\psi_t^{(1)}(y, t) + 0(\epsilon^2) \tag{3.4}$$

and

$$v_S = U_S\cdot tg\theta = U\cdot\theta^{(1)} + 0(\epsilon^2) \tag{3.5}$$

The oblique shock conditions on the shock front

$$x = Ut + \epsilon\cdot\psi_t^{(1)} + 0(\epsilon^2)$$

are

$$\left.\begin{aligned} \rho q_n &= \rho_0 q_{n0} \\ p + \rho q_n^2 &= p_0 + \rho_0 q_{n0}^2 \\ \frac{1}{2}q_n^2 + \frac{\gamma}{\gamma-1}\left(\frac{p}{\rho}\right) &= \frac{1}{2}q_{n0}^2 + \frac{\gamma}{\gamma-1}\frac{P_0}{\rho_0} \\ q_\tau &= q_{\tau 0} \end{aligned}\right\} \tag{3.6}$$

where

q_n = normal component of velocity of flow behind, relative to the shock

$$q_n = (v - v_S)\sin\theta + (u - U_S)\cos\theta = -U - \epsilon\cdot\psi_t^{(1)} + \epsilon\cdot u^{(1)} + 0(\epsilon^2) \tag{3.7}$$

q_τ = tangential component of velocity of flow behind, relative to the shock

$$q_\tau = (v - v_S)\cos\theta - (u - U_S)\sin\theta = \epsilon\cdot v^{(1)} + 0(\epsilon^2) \tag{3.8}$$

q_{n0} = normal component of velocity of flow in front, relative to the shock

$$q_{n0} = -v_S\sin\theta - [(U_0 - U) + U_S]\cos\theta = -U_0 - \epsilon\psi_t^{(1)} + 0(\epsilon^2) \tag{3.9}$$

$q_{\tau 0}$ = tangential component of velocity of flow in front, relative to the shock

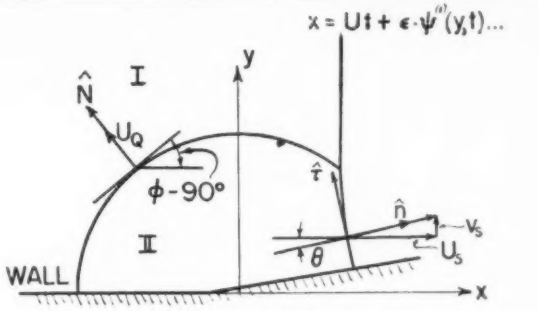

FIG. 3. Geometry of curved shocks.

$$q_{\tau 0} = -v_S\cos\theta + [(U_0 - U) + U_S]\sin\theta = -(U_0 - U)\cdot\epsilon\cdot\psi_y^{(1)} + 0(\epsilon^2) \tag{3.10}$$

Inserting Eq. (3.7) into Eq. (3.10) and Eq. (2.2) into Eq. (3.6), the coefficients of like orders of ϵ may be equated. The relations between the coefficients of ϵ^0 are equivalent to the customary normal shock conditions.

The relations between the coefficients of ϵ^1 yield four equations between the first-order quantities that, in keeping with the approximation of the linearized theory, are to be fulfilled at $x = Ut$, $y \geq 0$. These four equations can be written in the form

$$c^2\cdot\rho^{(1)}(x = Ut, y \geq 0, t) = (1 + \Omega_0)p^{(1)}(x = Ut, y \geq 0, t) \tag{3.11}$$

$$u^{(1)}(x = Ut, y \geq 0, t) = \frac{\Omega_1}{Rc}p^{(1)}(x = Ut, y \geq 0, t) \tag{3.12}$$

$$-(U_0 - U)\psi_t^{(1)}(y, t) = \frac{\Omega_2}{R}p^{(1)}(x = Ut, y \geq 0, t) \tag{3.13}$$

$$-(U_0 - U)\psi_y^{(1)}(y, t) = v^{(1)}\ (x = Ut, y \geq 0, t) \tag{3.14}$$

where

$$\left.\begin{aligned} \Omega_0 &= \frac{(\gamma-1)(M^2-1)^2}{[M^2(\gamma-1)+2]M^2} \\ \Omega_1 &= -\frac{1}{2M}\frac{(3\gamma-1)M^2 + (3-\gamma)}{M^2(\gamma-1)+2} \\ \Omega_2 &= -(1 - M^2)/M^2 \end{aligned}\right\} \tag{3.15}$$

By using differential Eqs. (2.3), (2.4), (2.6), and (2.7), one can eliminate $u^{(1)}$, $v^{(1)}$, $\rho^{(1)}$, and $\psi^{(1)}$ from the preceding four equations. In this way a boundary condition for $p^{(1)}$ alone, to be applied at the shock front $x = Ut$, can be formulated.

$$\underline{D_{x,\,t}p^{(1)}(x = Ut, y > 0, t) = 0} \tag{3.16}$$

where $D_{x,\,t}$ is a linear differential operator defined as

$$D_{x,\,t} = (\Omega_1 + M + \Omega_2 M)\frac{\partial^2}{\partial t^2} + (1 + M^2 + 2M\Omega_1)\cdot c\cdot\frac{\partial^2}{\partial x\partial t} + (\Omega_1 M^2 + M - M\Omega_2)c^2\frac{\partial^2}{\partial x^2} \tag{3.17}$$

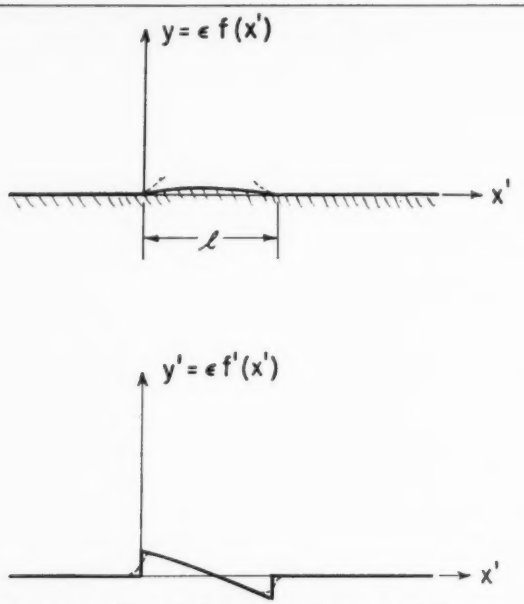

FIG. 4. The forms of $f(x')$ and $f'(x')$ for a shallow bump.

(2) *On the Wall*

The boundary condition on the wall is, in first approximation,

$$v^{(1)}(x \leq Ut, y = 0, t) = (U_0 - U)f'[x + (U_0 - U)t] \tag{3.18}$$

where the prime means differentiation with respect to the whole argument.

In general, $f'(x')$ is a bounded, sectionally continuous function of x' and has one-sided derivatives (see Fig. 4). Since it is possible to find a continuous function that is close to $f'(x')$, one may assume that $f'(x')$ is continuous and has continuous derivatives. This must be remembered if later on one tries to derive expression (4.11).

Using the differential Eq. (2.5), a boundary condition for $p^{(1)}$ at $y = 0$ can be derived from Eq. (3.18).

$$p_y^{(1)}(x < Ut, y = 0, t) = -R(U_0 - U)^2 f''[x + (U_0 - U)t] \tag{3.19}$$

(3) *The Point of Intersection of the Shock Front and the Wall*

In deriving the preceding two boundary conditions [Eqs. (3.16) and (3.19)], the special relation

$$v^{(1)}(x = Ut, y = 0, t) = (U_0 - U)f'(U_0 t) \tag{3.18a}$$

which can be applied at the intersection point of both surfaces, has not been really used. Additional information will be obtained if Eq. (3.18a) is combined, on the one hand, with the shock relations (3.13) and (3.14) and, on the other hand, with Eq. (3.18), which holds on the wall alone. From Eq. (3.14) it follows that

$$\psi_y^{(1)}(0, t) = -[1/(U_0 - U)]v^{(1)}(x = Ut, 0, t) = -f'(U_0 t)$$

$$\psi_{y't}^{(1)}(0, t) = -U_0 \cdot f''(U_0 t)$$

Differentiating Eq. (3.13) with respect to y, one obtains

$$\Omega_2 \cdot p_y^{(1)}(x = Ut, y > 0, t) = -R(U_0 - U)\psi_{yt}^{(1)}(y, t)$$

which implies

$$\left.\begin{aligned} \lim_{y \to 0} p_y^{(1)}(x = Ut, y > 0, t) &= \frac{RU_0(U_0 - U)}{\Omega_2} \cdot f''(U_0 t) \\ &= -\frac{4}{\gamma + 1} \cdot RUU_0 \cdot f''(U_0 t) \end{aligned}\right\} \tag{3.20}$$

Similarly, Eq. (3.19) implies

$$\lim_{x \to Ut} p_y^{(1)}(x < Ut, y = 0, t) = -R(U_0 - U)^2 \cdot f''(U_0 t) \tag{3.21}$$

One may note that the two limits for $p_y^{(1)}$ are equal if

$$[4/(\gamma + 1)] \cdot U \cdot U_0 = (U_0 - U)^2 \tag{3.22}$$

i.e., for a special shock strength $P/P_0 = 7.3076$ or $M = 0.5100$. In general, the above two limits for $p_y^{(1)}$ are unequal. This indicates that $p_y^{(1)}$ has a singularity at $x = Ut$, $y = 0$, as defined by Eqs. (3.20) and (3.21).

(4) *On the Reflected Shock (Mach Circle)*

Since the disturbance that spreads after the shock hit the leading edge is small, the boundary line separating the disturbed region II from the undisturbed region I (or from region III in case this region exists) is, except for terms of $0(\epsilon)$, the Mach circle; more explicitly, the curve

$$r = ct + \epsilon \cdot q^{(1)}(\varphi, t) + 0(\epsilon^2)$$

where $r = \sqrt{x^2 + y^2}$ and $\varphi = tg^{-1}y/x$ (see Fig. 3). However, in a consistent linearized scheme boundary conditions have to be prescribed at the undisturbed boundary—i.e., here at $r = ct$. Hence, one has to require that on the outer side of the Mach circle—i.e.,

at $r = (ct)^+$, $p^{(1)} = 0$ where domain II borders on domain I, and $p^{(1)} = p_{\text{Ackeret}}{}^{(1)}$ where domain II borders on domain III. It is shown in Appendix (I) that, under these conditions, $p^{(1)}$ varies continuously across the Mach circle; this means that, to the order ϵ', there is no discontinuity in $p^{(1)}$ across the Mach circle —i.e., the reflected shock is of $o(\epsilon)$.

Actually, it is not necessary to state the boundary condition in such detail. One may simply prescribe a condition at infinity.

$$p^{(1)} \to 0, \text{ as } \sqrt{x^2 + y^2} \to \infty \tag{3.23}$$

Then, the form of the solution of the wave equation, as assumed in Section (IV, 2), can be shown automatically to vanish in the whole domain I and to fulfill the above-stated conditions on the Mach circle. In this way, the domain of disturbance is, only formally, extended, the boundary now consisting of the full length of the incident shock, the x-axis from $-\infty$ to $x = Ut$, and the circular arc at infinity. The shifting of the circular boundary to infinity is an artifice that makes the solution procedure developed in Section (IV) more lucid.

(5) *Initial Conditions*

Obviously, the two initial conditions are

$$p^{(1)}(x \leq Ut, y \geq 0, t \leq 0) = 0 \tag{3.24}$$

$$p_t{}^{(1)}(x \leq Ut, y \geq 0, t \leq 0) = 0 \tag{3.25}$$

These conditions are actually implied by Eq. (3.19).

(IV) Derivation of the Analytic Solution* for $p^{(1)}$

(1) *The Lorentz Transformation*

The underlined equations [Eqs. (2.7), (3.16), (3.19) to (3.21), and (3.23) to (3.25)] summarize the formulation of the mathematical problem. The fact that the complicated boundary condition (3.16) is prescribed on the plane $x = Ut$ may suggest the introduction of new independent variables $(\bar{x}, \bar{y}, \bar{t})$ related to the old variables (x, y, t) by the well-known Lorentz transformation,

$$\left.\begin{aligned} \bar{x} &= (x - Ut)/\sqrt{1 - M^2}, \quad \bar{y} = y \\ \bar{t} &= (ct - Mx)/\sqrt{1 - M^2} \end{aligned}\right\} \tag{4.1}$$

The plane $\bar{x} = 0$ corresponds to the plane $x = Ut$, and the wave equation

$$p_{\bar{x}\bar{x}}{}^{(1)} + p_{\bar{y}\bar{y}}{}^{(1)} - p_{\bar{t}\bar{t}}{}^{(1)} = 0 \tag{4.2}$$

remains unchanged.

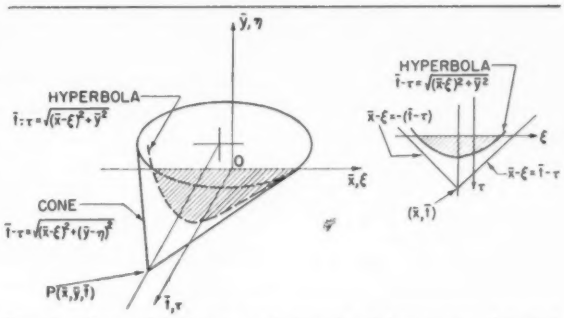

FIG. 5. Cone of influence and domain of integration (shaded area).

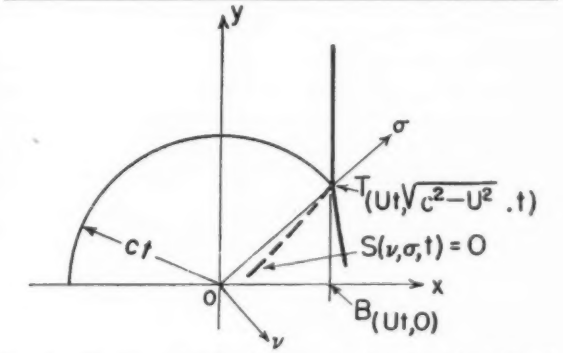

FIG. 6. The separation line between rotational and irrotational flow.

The boundary conditions become

$$p^{(1)} \to 0, \text{ as } \sqrt{\bar{x}^2 + \bar{y}^2} \to \infty \tag{4.3}$$

$$p_{\bar{y}}{}^{(1)}(\bar{x} < 0, \bar{y} = 0, \bar{t}) = Rc^2 A_0 f''[\bar{a}(\bar{\lambda}_0 \bar{x} + \bar{t})] \tag{4.4}$$

$$\bar{D}_{\bar{x},\bar{t}} p^{(1)}(\bar{x} = 0, \bar{y} > 0, \bar{t}) = 0 \tag{4.5}$$

and

$$\lim_{\bar{x} \to 0^-} p_{\bar{y}}{}^{(1)}(\bar{x}, 0, \bar{t}) = Rc^2 A_0 f''(\bar{a}\bar{t}) \tag{4.6}$$

$$\lim_{\bar{y} \to 0^+} p_{\bar{y}}{}^{(1)}(0, \bar{y}, \bar{t}) = Rc^2 \mu f''(\bar{a}\bar{t}) \tag{4.7}$$

where

$$\bar{a} = \frac{U_0}{c\sqrt{1 - M^2}}, \quad \bar{\lambda}_0 = \left(1 - M^2 + \frac{MU_0}{c}\right)\frac{c}{U}$$

$$A_0 = -\frac{(U_0 - U)^2}{c^2}, \quad \mu = -\frac{4}{\gamma + 1}\frac{U_0 M}{c}$$

and

$$\bar{D}_{\bar{x},\bar{t}} = \frac{1}{M_0{}^2}\frac{\partial^2}{\partial \bar{t}^2} + 2M\frac{\partial^2}{\partial \bar{x}\partial \bar{t}} + \frac{\partial^2}{\partial \bar{x}^2}$$

The initial conditions are now

$$p^{(1)} = p_{\bar{t}}{}^{(1)} = 0 \qquad (\text{for } \bar{t} \leq 0) \tag{4.8}$$

* The authors wish to express their appreciation to C. S. Gardner, Institute for Mathematics and Mechanics, New York University, for his valuable suggestions.

(2) *The Possio Integral*

In general, the solution of such boundary initial value problems as the one defined by Eqs. (4.2) to (4.8) can be solved in terms of what have been called "temporary sources" spread over a certain area in the x-t-plane characterizing the motion of the body (here, the motion of the wall relative to the air behind the shock). Such a solution can be written as Possio integral,[5]

$$p^{(1)}(\bar{x}, \bar{y}, \bar{t}) = -\frac{1}{\pi}\int_R\int \frac{p_{\bar{y}}{}^{(1)}(\xi, 0, \tau)}{\sqrt{(\bar{t}-\tau)^2 - (\bar{x}-\xi)^2 - \bar{y}^2}}\, d\xi\, d\tau \tag{4.9}$$

in which the numerator $p_{\bar{y}}{}^{(1)}$ of the integrand represents the "source strength" and the denominator represents the "pseudo distance" between "source point" ξ, τ and point x, y, t. The integration area R in the $\xi - \tau$-plane is confined by the hyperbola

$$\bar{t} - \tau = \sqrt{(\bar{x}-\xi)^2 + \bar{y}^2}$$

and the straight line $\tau = 0$. Looking at Fig. 5, it is obvious that the method is applicable only if $p_{\bar{y}}{}^{(1)}$ is prescribed on the entire plane $\bar{y} = 0$.

Actually, however, $p_{\bar{y}}{}^{(1)}$ is given for the left half of the plane $\bar{y} = 0$ ($\bar{x} < 0$), while it is unknown in the right half plane ($\bar{x} > 0$). Hence, the next step is to find an equation for $p_{\bar{y}}{}^{(1)}(\bar{x} > 0, \bar{y} = 0, \bar{t})$, which will replace condition (4.5) prescribed on the plane $\bar{x} = 0$ and also produce the correct type of singularity for $p_{\bar{y}}{}^{(1)}$ at the origin as defined by Eqs. (4.6) and (4.7).

Inserting the proper integration limits and using condition (4.4), the Possio integral (4.9) becomes

$$p^{(1)}(\bar{x} \leq 0, \bar{y}, \bar{t}) = -\frac{Rc^2A_0}{\pi}\int_0^{\bar{t}-\bar{y}} d\tau \int_{\bar{x}-\sqrt{(\bar{t}-\tau)^2-\bar{y}^2}}^{0} d\xi\, \frac{f''[\bar{a}(\tau + \bar{\lambda}_0\xi)]}{\sqrt{(\bar{t}-\tau)^2 - (\bar{x}-\xi)^2 - \bar{y}^2}} - \frac{1}{\pi}\int_0^{\bar{t}-\sqrt{\bar{x}^2+\bar{y}^2}} d\tau \int_0^{\bar{x}+\sqrt{(\bar{t}-\tau)^2-\bar{y}^2}} d\xi\, \frac{p_{\bar{y}}{}^{(1)}(\xi > 0, 0, \tau)}{\sqrt{(\bar{t}-\tau)^2 - (\bar{x}-\xi)^2 - \bar{y}^2}} \tag{4.10}$$

Substituting Eq. (4.10) into Eq. (4.5) will provide the desired equation for the unknown function $p_{\bar{y}}{}^{(1)}(\xi > 0, 0, \tau)$

(3) *Determination of* $p_{\bar{y}}{}^{(1)}(\xi > 0, 0, \tau)$

By carrying out the proper differentiations with regard to $\bar{x}$ and $\bar{t}$, one obtains

$$\bar{D}_{\bar{x},\bar{t}}\, p^{(1)}(\bar{x} = 0, \bar{y} > 0, \bar{t}) = \frac{-Rc^2A_0\bar{a}^2\cdot H(-\bar{\lambda}_0)}{\pi}\int_0^{\bar{t}-\bar{y}} d\tau \int_{-\sqrt{(\bar{t}-\tau)^2-\bar{y}^2}}^{0} d\xi\, \frac{f^{(IV)}[\bar{a}(\tau + \bar{\lambda}_0\xi)]}{\sqrt{(\bar{t}-\tau)^2 - \xi^2 - \bar{y}^2}} - \frac{1}{\pi}\int_0^{\bar{t}-\bar{y}} d\tau \int_0^{\sqrt{(\bar{t}-\tau)^2-\bar{y}^2}} d\xi\, \frac{\bar{D}_{\xi,\tau}\, p_{\bar{y}}{}^{(1)}(\xi > 0, 0, \tau)}{\sqrt{(\bar{t}-\tau)^2 - \xi^2 - \bar{y}^2}} - \frac{1}{\pi}\int_0^{\bar{t}-\bar{y}} d\tau\, \frac{\Delta_2(\tau) + 2M\cdot\Delta_1'(\tau)}{\sqrt{(\bar{t}-\tau)^2 - \bar{y}^2}} \tag{4.11}$$

where

$$H(\bar{\lambda}) = (1/M_0^2) - 2M\bar{\lambda} + \bar{\lambda}^2$$
$$\Delta_1(\bar{t}) = p_{\bar{y}}{}^{(1)}(\bar{x} = 0^+, \bar{y} = 0, \bar{t}) - p_{\bar{y}}{}^{(1)}(\bar{x} = 0^- \bar{y} = 0, \bar{t})$$
$$\Delta_1'(\bar{t}) = (d/d\bar{t})\Delta_1(\bar{t})$$
$$\Delta_2(\bar{t}) = p_{\bar{y}\bar{x}}{}^{(1)}(\bar{x} = 0^+, \bar{y} = 0, \bar{t}) - p_{\bar{y}\bar{x}}{}^{(1)}(\bar{x} = 0^-, \bar{y} = 0, \bar{t})$$

Since $p^{(1)}$ is a solution of the wave equation, it is seen that the identity

$$p_{\bar{y}}{}^{(1)}(\bar{x} = 0^+, \bar{y} = 0, \bar{t}) + p_{\bar{y}}{}^{(1)}(\bar{x} = 0^-, \bar{y} = 0, \bar{t}) = 2p_{\bar{y}}{}^{(1)}(\bar{x} = 0, \bar{y} = 0^+, \bar{t}) \tag{4.12}$$

holds true, which represents a kind of "mean value theorem" at the singularity. [For proof, see Appendix (2).]

This relation and the property of the singularity defined by Eqs. (4.6) and (4.7) yield

$$\Delta_1(\bar{t}) = 2Rc^2(\mu - A_0)f''(\bar{a}\bar{t}) \tag{4.13}$$

or

$$p_{\bar{y}}{}^{(1)}(\bar{x} = 0^+, \bar{y} = 0, \bar{t}) = Rc^2(2\mu - A_0)f''(\bar{a}\bar{t}) \tag{4.14}$$

According to Eq. (4.5), expression (4.11) is required to vanish. This will be the case, if

$$\bar{D}_{\bar{x},\bar{t}}[p_{\bar{y}}{}^{(1)}(\bar{x} > 0, \bar{y} = 0, \bar{t})] = -Rc^2A_0\bar{a}^2\cdot H(-\bar{\lambda}_0)\cdot f^{(IV)}[\bar{a}(\bar{t} - \bar{\lambda}_0\bar{x})] \tag{4.15}$$

and

$$\Delta_2(\bar{t}) = -2M\Delta_1'(\bar{t}) = -4MRc^2(\mu - A_0)\bar{a}f'''(\bar{a}\bar{t})$$

or

$$p_{\bar{y}\bar{x}}{}^{(1)}(\bar{x} = 0^+, \bar{y} = 0, \bar{t}) = \bar{a}Rc^2[A_0(\bar{\lambda}_0 + 4M) - 4M\mu]f'''(\bar{a}\bar{t}) \tag{4.16}$$

Hence, the problem is reduced to obtaining a function $p_{\bar{y}}{}^{(1)}(\bar{x} > 0, \bar{y} = 0, \bar{t})$, which satisfies differential Eq. (4.15) and boundary conditions (4.14) and (4.16). It is shown in Appendix (3) that the solution has the form

$$p_{\bar{y}}{}^{(1)}(\bar{x} > 0, \bar{y} = 0, \bar{t}) = Rc^2\{A_1f''[\bar{a}(\bar{t} - \bar{\lambda}_1\bar{x})] + A_2f''[\bar{a}(\bar{t} - \bar{\lambda}_2\bar{x})] + A_3f''[\bar{a}(\bar{t} - \bar{\lambda}_3\bar{x})]\} \tag{4.17}$$

where the expressions for $\bar{a}$, $\bar{\lambda}_i$, and A_i are listed in the next section.

(V) The Final Results

(1) *Expressions for* $p^{(1)}$, $\rho^{(1)}$, $u^{(1)}$, $v^{(1)}$, *and* $\psi^{(1)}$

The results obtained in the previous section can be summarized as follows:

$$p^{(1)}(\bar{x}, \bar{y}, \bar{t}) = -\frac{Rc^2A_0}{\pi}\int_0^{\bar{t}-\bar{y}} d\tau \int_{\bar{x}-\sqrt{(\bar{t}-\tau)^2-\bar{y}^2}}^{0} d\xi \frac{f''[\bar{a}(\tau + \bar{\lambda}_0\xi)]}{\sqrt{(\bar{t}-\tau)^2 - (\bar{x}-\xi)^2 - \bar{y}^2}} - \sum_{i=1,}^{2,3} \frac{Rc^2A_i}{\pi}\int_0^{\bar{t}-\sqrt{\bar{x}^2+\bar{y}^2}} d\tau \int_0^{\bar{x}+\sqrt{(\bar{t}-\tau)^2-\bar{y}^2}} d\xi \frac{f''[\bar{a}(\tau - \bar{\lambda}_i\xi)]}{\sqrt{(\bar{t}-\tau)^2 - (\bar{x}-\xi)^2 - \bar{y}^2}} \tag{5.1}$$

where

$$\bar{a} = \frac{U_0}{c\sqrt{1-M^2}}, \qquad \bar{\lambda}_0 = \left(1 - M^2 + \frac{MU_0}{c}\right)\frac{c}{U_0}$$

$$A_0 = -(U_0 - U)^2/c^2, \qquad \bar{\lambda}_1 = \bar{\lambda}_0$$

$$A_1 = -A_0\frac{\bar{\lambda}_0{}^2 + 2M\bar{\lambda}_0 + (1/M_0{}^2)}{\bar{\lambda}_0{}^2 - 2M\bar{\lambda}_0 + (1/M_0{}^2)}$$

$\bar{\lambda}_2$ and $\bar{\lambda}_3$ are the roots of the quadratic equation

$$\bar{\lambda}^2 - 2M\bar{\lambda} + (1/M_0)^2 = 0$$

and A_2 and A_3 are the solutions of the two simultaneous linear equations

$$A_2 + A_3 + A_1 + A_0 = -[8/(\gamma + 1)]/(MU_0/c)$$

$$\bar{\lambda}_2A_2 + \bar{\lambda}_3A_3 + \bar{\lambda}_1A_1 + \bar{\lambda}_0A_0 = 2M\left(\frac{8}{\gamma + 1}\frac{MU_0}{c} - A_0\right)$$

The above solution is unique and satisfies the wave equation and all the initial and boundary conditions.

By using the transformation (4.1), the disturbance pressure $p^{(1)}(x, y, t)$ can be obtained from $p^{(1)}(\bar{x}, \bar{y}, \bar{t})$.

From differential Eqs. (2.4) to (2.6) and the boundary conditions (3.11) to (3.14) the following expressions are obtained:

The density variation:

$$\begin{aligned}\rho^{(1)}(x, y, t) &= (1/c^2)p^{(1)}(x, y, t) + W(x, y) \\ &= (1/c^2)p^{(1)}(x, y, t) + (\Omega_0/c^2)p^{(1)}[x, y, t = (x/U)]\end{aligned} \tag{5.2}$$

The x-component of the disturbance velocity:

$$u^{(1)}(x, y, t) = -\frac{1}{R}\int_{x/U}^{t} d\tau \cdot p_x{}^{(1)}(x, y, \tau) - \frac{\Omega_1}{Rc}p^{(1)}\left(x, y, t = \frac{x}{U}\right) \tag{5.3}$$

The form of the shock front:

$$x = Ut - \epsilon\cdot\frac{\Omega_2}{R(U_0 - U)}\int_0^t p^0(x = U\tau, y, \tau)\, d\tau \tag{5.4}$$

The y-component of the disturbance velocity:

$$v^{(1)}(x, y, t) = -\frac{1}{R}\int_{x/U}^{t} p_{\bar{y}}{}^{(1)}(x, y, \tau)\, d\tau + \frac{\Omega_2}{R}\int_0^{x/U} p_y{}^{(1)}(U\tau, y, \tau)\, d\tau \tag{5.5}$$

(2) *The Separation Line Between Rotational and Irrotational Flow—Its Physical Significance*

From Appendix (1) it can be seen that (on the shock, outside $r = ct$)

$$p^{(1)}(x, y, t = x/U) = 0 \text{ for } x^2 + y^2 \geq x^2/M^2$$

hence, also,

$$\frac{\Omega_0}{c^2} \cdot p^{(1)}\left(x, y, t = \frac{x}{U}\right) = 0 \text{ for } x\sqrt{1 - M^2} \leq My$$

Taking this into account, it follows from Eq. (5.2) that the lines of constant density (isopycnics) coincide with the lines of constant pressure (isobars) for $x/y \leq M/\sqrt{1 - M^2}$, but deviate from the latter for $x/y \geq M/\sqrt{1 - M^2}$; i.e., inside the area OTB of Figs. 6 or 7.

In other words, looking at Fig. 7, the flow inside OTB is rotational, outside, it is irrotational. This is in accordance with Kelvin's theorem, since no particles cross the separation line OT. Since the reflected circular shock is of $o(\epsilon)$, in a first-order theory particles can acquire vorticity not by crossing the reflected shock but only by crossing the curved portion of the incident shock TB. These particles stay inside the area swept over by TB—i.e., inside the area OTB.

The form of this separation line can be represented by (see Fig. 6)

$$\nu = \epsilon \cdot S^{(1)}(\sigma, \tau) + 0(\epsilon^2)$$

where

$$\nu = x \cdot \sqrt{1 - M^2} - y \cdot M, \quad \sigma = x \cdot M + y \cdot \sqrt{1 - M^2}$$

$$S^{(1)}(\sigma, \tau) = \int_0^t [\sqrt{1 - M^2} \cdot u^{(1)}(x, y, \tau) - M \cdot v^{(1)}(x, y, \tau)]\, d\tau$$

$$x = \sigma M$$
$$y = \sigma\sqrt{1 - M^2}$$

Since

$$\lim_{x - y(M/\sqrt{1 - M^2}) = 0^+} p^{(1)}(x, y, x/U) = 0$$

there is no discontinuity of density—i.e., no slipstream in the mathematical sense, at least not in first approximation (perhaps in higher approximation). However, it will turn out that in a physical sense there is a slipstream of finite width, as explained in Section (VI).

(VI) Application of the Theory

The shape of the wall (or of the airfoil) $y = \epsilon \cdot f(x')$, $0 \leq x' \leq 1$, may be approximated by a polynomial

$$f_n(x') = c_1 \cdot x' + c_2 \cdot x'^2 + \ldots c_n \cdot x'^n \tag{6.1}$$

The accuracy of the approximation increases with the order of the polynomial. While the case of higher polynomials (a circular arc airfoil) is treated elsewhere,[6] one may here consider the simplest example,

$$f(x') = x' \tag{6.2}$$

representing a corner of inclination ϵ. Then,

$$f'(x') = 1 \text{ for } x' > 0 \text{ and } f'(x') = 0 \text{ for } x' < 0$$

Furthermore,

$$\left.\begin{aligned} f''(x') &= 0 \qquad (\text{for } x' \neq 0) \\ \int_{-}^{0^+} f''(x')\, dx' &= 1 \end{aligned}\right\} \tag{6.3}$$

Using Eqs. (6.3), the pressure integral (5.1) can be evaluated and yields

$$p^{(1)}(x, y, t) = -\frac{Rc^2}{\pi a}\left\{A_0 \cdot N(x, y, t, -\lambda_0) + \sum_{i=1}^{2,3} A_i N(x, y, t, \lambda_i)\right\} \tag{6.4}$$

where

$$N(x, y, t, \lambda) = \frac{1 - \lambda M}{\sqrt{\lambda^2 - 1}} \cdot \cosh^{-1} \frac{|\lambda t - x|}{\sqrt{(t - \lambda x)^2 + (\lambda^2 - 1)y^2}} \quad (\text{for } \lambda > 1)$$

$$= (1 - \lambda M)\,(\sqrt{t^2 - x^2 - y^2}/t - \lambda x) \quad (\text{for } \lambda = 1)$$

$$= \frac{1 - \lambda M}{\sqrt{1 - \lambda^2}} \cdot \cos^{-1} \frac{|\lambda t - x|}{\sqrt{(t - \lambda x)^2 + (\lambda^2 - 1)y^2}} \quad (\text{for } \lambda < 1),$$

and

$$\lambda_0 = \frac{\bar{\lambda}_0 - M}{1 - \bar{\lambda}_0 M}, \qquad a = \bar{a}\sqrt{1 - M^2} = \frac{U_0}{c}$$

$$\lambda_i = \frac{\bar{\lambda}_i + M}{1 + \bar{\lambda}_i M}, \qquad (\text{for } i = 1, 2, 3)$$

Substituting Eq. (6.4) into Eqs. (5.2), (5.3), (5.4), and (5.5), one obtains, respectively, the density variation:

$$\rho^{(1)}(x, y, t) = -\frac{R}{\pi}\left[A_0 N(x, y, t, -\lambda_0) + \sum_{i=1,}^{2,3} A_i N(x, y, t, \lambda_i)\right] + W(x, y) \tag{6.5}$$

where

$$W(x, y) = -\frac{\Omega_2 R}{\pi}\left[A_0 \cdot N\left(x, y, t = \frac{x}{U}, -\lambda_0\right) + \sum_{i=1,}^{2,3} A_i N\left(x, y, t = \frac{x}{U}, \lambda_i\right)\right]$$

and the form of the incident shock:

$$x = Ut + \epsilon \cdot \psi^{(1)}(y, t) + 0(\epsilon^2) \tag{6.6}$$

where

$$\psi^{(1)}(y, t) = -\frac{\gamma + 1}{4M\pi a}\left[A_0 CtN(x = Ut, y, t, -\lambda_0) + \sum_{i=1,}^{2,3} A_i C \cdot t \cdot N(Ut, y, t, \lambda_i) - \right.$$

$$\left. y \cdot A_0 L(Ut, y, t, -\lambda_0) - y. \sum_{i=1,}^{2,3} A_i L(Ut, y, t, \lambda_i)\right]$$

with

$$L(x, y, t, \lambda) = \tan^{-1} \frac{|t - \lambda x|}{|\lambda t - x|} \cdot \frac{\sqrt{t^2 - x^2 - y^2}}{y}$$

As a numerical example, the pressure and density fields have been computed for $P/p_0 = 7.3076$ or $(U_0 - U)/c = 1.21$ and $M = 0.5100$. The isopycnics and isobars, as well as the curved shock front, are plotted as shown in Fig. 7. It is interesting to note how strongly and suddenly each isopycnic splits off from the corresponding isobar after traversing the separation line OT between rotational and irrotational flow. Within a thin strip along OT, there is a steep density gradient, while there is no appreciable pressure gradient. This may be interpreted as a slipstream of finite width. This slipstream, which must be expected with every Mach reflexion, can be clearly seen in Bleakney's[7] interferograms; also, the characteristic shape of the isopycnics in the vicinity of OT has been recently[8] verified experimentally in all details.

Appendix (1)

Proof That Solution (4.10) for $p^{(1)}(x, y, t)$ Vanishes at Infinity and Fulfills the Conditions on the Mach Circle, as Stated in Section (III, 4)

Since $f''(x') = 0$ for $x' \leq 0$, the integrand of the Possio integral (4.10) vanishes when $\bar{\lambda}_0\xi + \tau \leq 0$. Expressing it in other words: "Sources of intensity $p_y{}^{(1)}$" are spread only over that part of the ξ-τ-plane which is to the right of the line $\bar{\lambda}_0\xi + \tau = 0$. (See Fig. 8, a, b, and c.) Now, the conical surface appearing in Figs. 2, a and b—namely $x^2 + y^2 = c^2t^2$, $x < Ut$—will, also in Lorentz coordinates, be a conical surface—namely $\bar{x}^2 + \bar{y}^2 = \bar{t}^2$, $\bar{x} < 0$. (See Fig. 9, a and b.) Any point $\bar{x}$, $\bar{y}$, $\bar{t}$, lying on this conical surface will be influenced only by sources in the $\xi - \tau$-plane which lie inside the area R bounded by the τ-axis and by the hyperbola $\tau^2 - \xi^2 - 2\bar{t}\tau + 2\bar{x}\xi = 0$, which passes through the origin ($\xi = 0$, $\tau = 0$). Since in that case the integration area R does not include sources with $p_y(\xi > 0)$,

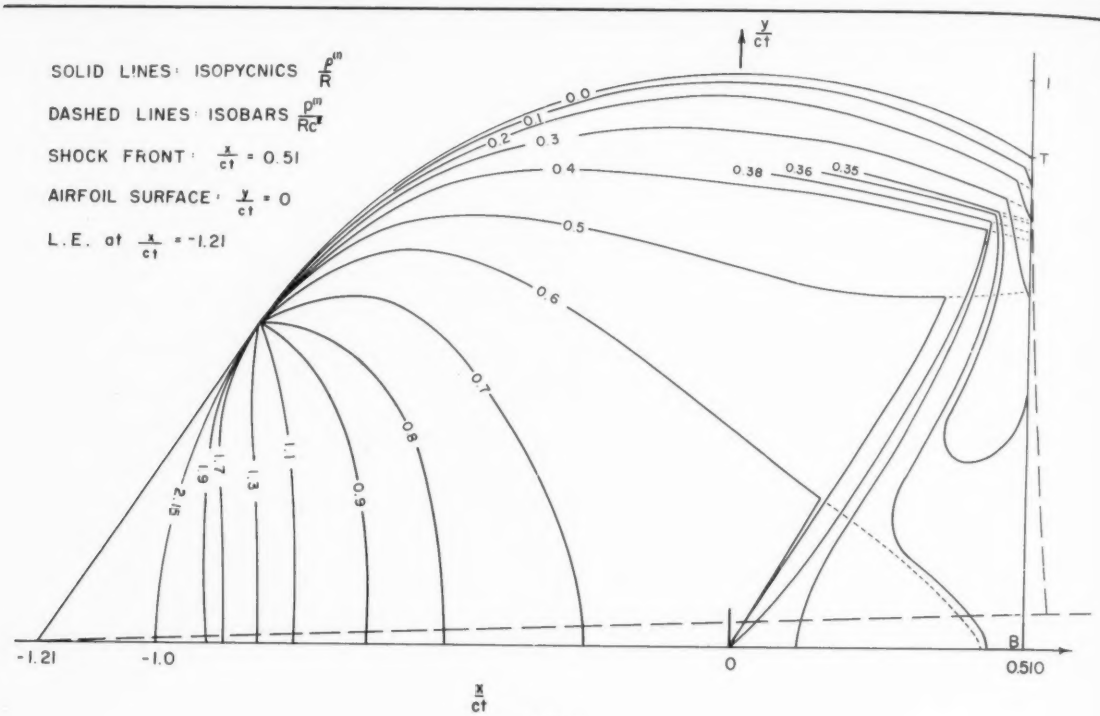

FIG. 7.

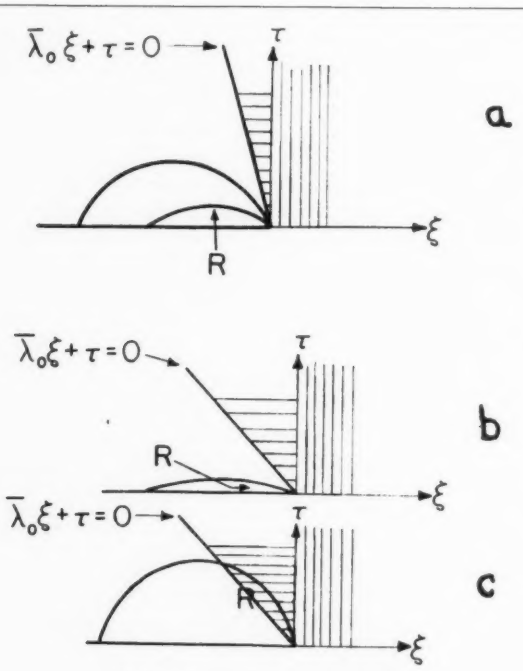

FIG. 8. Properties of the solution.

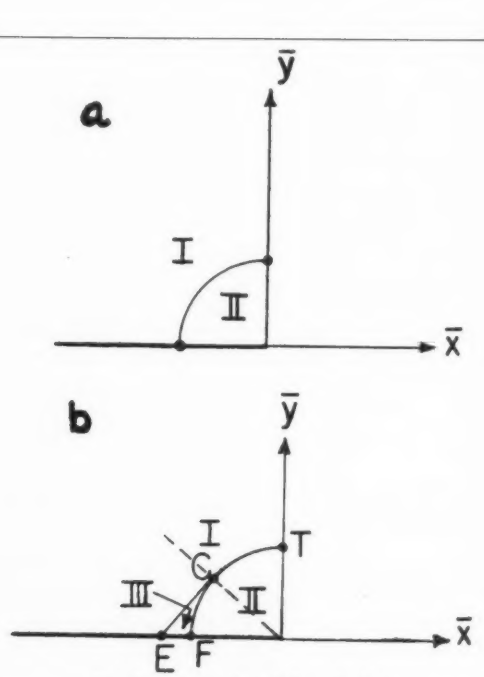

FIG. 9. Properties of the solution.

the second integral in Eq. (4.10) does not come into play, and

$$p^{(1)}(\bar{x}, \bar{y}, \bar{t}) = -\frac{Rc^2A_0}{\pi} \times \iint_{\xi<0} \frac{f''[\bar{a}(\bar{\lambda}_0\xi + \tau)]}{\sqrt{(\bar{t}-\tau)^2 - (\bar{x}-\xi)^2 - \bar{y}^2}}\, d\xi\, d\tau \quad (4.10a)$$

The same reasoning applies for points outside the Mach cone, for which $\bar{x}^2 + \bar{y}^2 - \bar{t}^2 > 0$ or $x^2 + y^2 - c^2t^2 > 0$. The corresponding hyperbola is shifted to the left.

(a) If $\bar{\lambda}_0 \geq 1$—i.e., $(U_0 - U)/c < 1$ (see Fig. 8a)—the bounding line (L.E.), $\bar{\lambda}_0\xi + \tau = 0$, is relatively steep and will not intersect the hyperbola of any point on or outside the cone, because

$$\left|d\tau/d\xi\right|_{\text{L.E.}} = \bar{\lambda}_0 \geq 1$$

but

$$\left|\frac{d\tau}{d\xi}\right|_{\text{hyp.}} = \frac{\bar{x}}{\sqrt{\bar{x} + \bar{y}^2}} < 1$$

Hence, inside R the integrand is identically zero. Thus, $p^{(1)} = o$.

(b) If $\bar{\lambda}_0 < 1$—i.e., $(U_0 - U)/c > 1$—the bounding line is less steep than in (a) and will or will not intersect the hyperbola depending on the location of point $(\bar{x}, \bar{y}, \bar{t})$. See Figs. 8, b and c. An intersection will occur if $\bar{x}/\sqrt{\bar{x}^2 + \bar{y}^2} > \bar{\lambda}_0$, which is now smaller than 1. The line $\bar{y}/\bar{x} = \sqrt{1/\bar{\lambda}_0^2 - 1}$, which separates the points $\bar{x}, \bar{y}, \bar{t}$ which furnish intersection from those that do not, hits the Mach circle at the point of tangency of the Mach line, as indicated in Fig. 9b. For any point lying between C and T, the hyperbola will be located as indicated in Fig. 8b—i.e., here again, $p^{(1)} = o$. However, for points lying between F and C, the hyperbola will be located as in Fig. 8c—i.e., now the "source intensity" is different from zero in part of the integration area R. However, the integrand depends only on $p_{\bar{y}}^{(1)}(\xi < 0)$ and not on $p_{\bar{y}}^{(1)}(\xi > 0)$. Only the latter expression is related to the shock diffraction by Eq. (4.15); the former is determined by the boundary condition on the body surface alone, so that the disturbance pressure agrees with that given by the Ackeret theory for steady supersonic flow, and Eq. (4.10a) yields

$$p^{(1)} = -\frac{Rc^2A_0}{\bar{a}\sqrt{1 - \bar{\lambda}_0^2}} \cdot f'[\bar{a}(\bar{t} + \bar{\lambda}_0 \cdot \bar{x} - \bar{y} \cdot \sqrt{1 - \bar{\lambda}_0^2})]$$

For points $\bar{x}, \bar{y}, \bar{t}$ inside the cone, the hyperbola will again be shifted in the direction of positive ξ and will enclose sources with $p_{\bar{y}}^{(1)}(\xi > 0, 0, \tau)$—i.e., $p^{(1)}$ will then be influenced by the shock diffraction.

It is evident that $p^{(1)} = 0$ for

$$\bar{t} + \bar{\lambda}_0 \cdot \bar{x} - \bar{y} \cdot \sqrt{1 - \bar{\lambda}_0^2} \leq 0$$

i.e., to the left of EC, which is tangent to the Mach cone.

Furthermore, it is obvious that the hyperbola corresponding to any point in domain I, with large coordinates $\bar{x}$ or $\bar{y}$, will be shifted considerably in the direction of negative ξ or negative τ. In other words: $p^{(1)}(\infty) = 0$, as stipulated in Section (III, 4).

From the preceding discussion it can be seen that in either case (a) or (b), if the point under consideration moves continuously from the outside to the inside across the Mach circle of Fig. 9a or 9b, the respective hyperbola moves continuously into the domain which is covered by sources of intensity $p_{\bar{y}}^{(1)}(\xi > 0)$. Since the source intensity is everywhere finite, it follows that $p^{(1)}$ will vary continuously across the Mach circle. Thus, to the order ϵ', there is no discontinuity of pressure; the reflected shock is of $o(\epsilon)$.

From the uniqueness of the solution follows that requiring the solution to vanish at infinity is equivalent with imposing the boundary condition on the Mach circle.

Appendix (2)

Proof of the Identity (4.12)

If $p_{\bar{y}}^{(1)}(\bar{x}, 0, \bar{t})$ has a discontinuity at $\bar{x} = 0$ and a right- and left-hand derivative with respect to $\bar{x}$, then the Possio integral (4.10) becomes

$$p^{(1)}(\bar{x} = 0, \bar{y}, \bar{t}) = -\frac{1}{\pi}\int_0^{\bar{t}-\bar{y}} d\tau \int_0^{\sqrt{(\bar{t}-\tau)^2-\bar{y}^2}} \frac{p_{\bar{y}}^{(1)}(\xi) > 0, 0, \tau)}{\sqrt{(\bar{t}-\tau)^2 - \xi^2 - \bar{y}^2}}\, d\xi + \frac{1}{\pi}\int_0^{\bar{t}-\bar{y}} d\tau \int_{+\sqrt{(\bar{t}-\tau)^2-\bar{y}^2}}^{0} \frac{p_{\bar{y}}^{(1)}(-\xi' < 0, 0, \tau)}{\sqrt{(\bar{t}-\tau)^2 - \xi'^2 - \bar{y}^2}}\, d\xi'$$

Integrating by parts, one obtains

$$p^{(1)}(\bar{x} = 0, \bar{y}, \bar{t}) = +\frac{1}{\pi}\int_0^{\bar{t}-\bar{y}} d\tau \left[p_{\bar{y}}(\xi > 0, 0, \tau) \cos^{-1}\frac{\xi}{\sqrt{(\bar{t}-\tau)^2 - \bar{y}^2}} \right|_{\xi=0^+}^{\xi=\sqrt{(\bar{t}-\tau)^2-\bar{y}^2}} -$$

(*Equation continued on page 328*)

$$p_{\bar{y}}(-\xi' < 0, 0, \tau) \cos^{-1} \frac{\xi'}{\sqrt{(\bar{t} - \tau)^2 - \bar{y}^2}} \Bigg|_{\xi' = +\sqrt{(\bar{t}-\tau)^2 - \bar{y}^2}}^{\xi' = 0^+} \Bigg] - \frac{1}{\pi} \int_0^{\bar{t}-\bar{y}} d\tau \Bigg[\int_0^{\sqrt{(\bar{t}-\tau)^2 - \bar{y}^2}} p_{\bar{y}\bar{x}}^{(1)}(\xi > 0, 0, \tau) \times$$

$$\cos^{-1} \frac{\xi}{\sqrt{(\bar{t} - \tau)^2 - \bar{y}^{2\prime}}} \, d\xi - \int_{+\sqrt{(\bar{t}-\tau)^2 - \bar{y}^2}}^{0} p_{\bar{y}\bar{x}}^{(1)}(-\xi' < 0, 0, \tau) \cos^{-1} \frac{\xi'}{\sqrt{(\bar{t} - \tau)^2 - \bar{y}^2}} \, d\xi' \Bigg]$$

$$p^{(1)}(\bar{x} = 0, \bar{y}, \bar{t}) = -\frac{1}{2} \int_0^{\bar{t}-\bar{y}} [p_{\bar{y}}^{(1)}(x = 0^+, 0, \tau) + p_{\bar{y}}^{(1)}(x = 0^-, 0, \tau)] \, d\tau -$$

$$\frac{1}{\pi} \int_0^{\bar{t}-\bar{y}} d\tau \Bigg[\int_0^{\sqrt{(\bar{t}-\tau)^2 - \bar{y}^2}} p^{(1)}(\xi > 0, 0, \tau) \cos^{-1} \frac{\xi}{\sqrt{(\bar{t} - \tau)^2 - \bar{y}^2}} \, d\xi -$$

$$\int_{+\sqrt{(\bar{t}-\tau)^2 - \bar{y}^2}}^{0} p_{\bar{y}\bar{x}}^{(1)}(-\xi' < 0, 0, \tau) \cos^{-1} \frac{\xi'}{\sqrt{(\bar{t} - \tau)^2 - \bar{y}^2}} \, d\xi' \Bigg]$$

Differentiating both sides with respect to y, and letting y approach zero, the terms due to the second integral approach zero. Therefore, one obtains Eq. (4.12),

$$\lim_{\bar{y} \to 0^+} p_{\bar{y}}^{(1)}(\bar{x} = 0, \bar{y}, \bar{t}) = \frac{1}{2} [p_{\bar{y}}^{(1)}(\bar{x} = 0^+, 0, \bar{t}) + p_{\bar{y}}^{(1)}(\bar{x} = 0^-, 0, \bar{t})]$$

Appendix (3)

Derivation of the Solution of Eqs. (4.14) to (4.16)

The partial differential equation (4.15) for $p^{(1)}(\bar{x} > 0, \bar{y} = 0, \bar{t})$ is always hyperbolic, since the discriminant

$$(2M)^2 - (4/M_0^2) = 2(\gamma + 1)(1 - M^2) \times \left(1 + \frac{\gamma - 1}{2} M^2\right)^{-1} > 0$$

for all values of p_0/P from 0 to 1.

The solution of the differential equation (4.15) is

$$p_{\bar{y}}^{(1)}(\bar{x} > 0, \bar{y} = 0, \bar{t}) = \Gamma_2(\bar{t} - \bar{\lambda}_2\bar{x}) + \Gamma_3(\bar{t} - \bar{\lambda}_3\bar{x}) + Rc^2 \frac{H(-\bar{\lambda}_0)}{H(\bar{\lambda}_0)} A_0 \cdot f''[\bar{a}(\bar{t} - \bar{\lambda}_0\bar{x})]$$

where $\bar{\lambda}_2$ and $\bar{\lambda}_3$ are the roots (distinct, real and positive) of the quadratic equation,

$$H(\bar{\lambda}) = \bar{\lambda}^2 - 2M\bar{\lambda} + (1/M_0^2) = 0$$

Γ_2 and Γ_3 are two arbitrary functions to be determined by the boundary conditions (4.14) and (4.16).

$$\Gamma_2(\bar{t}) + \Gamma_3(\bar{t}) + Rc^2 A_0 [H(-\bar{\lambda}_0)/H(\bar{\lambda}_0)] f''(a\bar{t}) = Rc^2(2\mu - A_0) f''(\bar{a}\bar{t})$$

$$\bar{\lambda}_2\Gamma_2'(\bar{t}) + \bar{\lambda}_3\Gamma_3'(\bar{t}) + \bar{\lambda}_0\bar{a}Rc^2A_0 [H(-\bar{\lambda}_0)/H(\bar{\lambda}_0)] f'''(\bar{a}\bar{t}) = -\bar{a}Rc^2[A_0(\bar{\lambda}_0 + 4M) - 4M\mu] f'''(\bar{a}\bar{t})$$

This leads directly to

$$\Gamma_2(\bar{t}) = Rc^2A_2f''(\bar{a}\bar{t})$$
$$\Gamma_3(\bar{t}) = Rc^2A_3f''(\bar{a}\bar{t})$$

The constants A_2 and A_3 are determined uniquely by the two simultaneous equations

$$A_2 + A_3 - [H(-\bar{\lambda}_0)/H(\bar{\lambda}_0)]A_0 = 2\mu - A_0$$

$$\bar{\lambda}_2A_2 + \bar{\lambda}_3A_3 - \bar{\lambda}_0A_0[H(-\bar{\lambda}_0)/H(\bar{\lambda}_0)] = -A_0(\bar{\lambda}_0 + 4M) + 4M\mu$$

since the determinant

$$\begin{vmatrix} 1 & 1 \\ \bar{\lambda}_2 & \bar{\lambda}_3 \end{vmatrix} \neq 0$$

References

[1] Bargmann, V., N.D.R.C., Report AMP 108.2R, 1945.

[2] Lighthill, M. J., Proc. Roy. Soc., Series A, Vol. 198, pp. 454-470.

[3] Courant, R., and Friedrichs, K. O., *Supersonic Flow and Shockwaves*, pp. 326, 341; Interscience Publishers, Inc., New York, 1948.

[4] Lamb, H., *Hydrodynamics*, 4th Ed., pp. 7, 8; Cambridge University Press, 1916.

[5] See, e.g., Gardner, C. S., and Ludloff, H. F., Journal of the Aeronautical Sciences, Vol. 17, No. 1, pp. 47–59, January, 1950.

[6] Ferdman, S., Master's Thesis, New York University, College of Engineering, 1951.

[7] Bleakney, W., and Taub, A. H., *Interaction of Shock Waves*, Review of Modern Physics, Vol. 21, No. 4, pp. 584–605, 1948.

[8] White, D. R., Doctoral Thesis, Princeton University, 1951.

The Measurement of Downwash and Sidewash Behind a Rectangular Wing at a Mach Number of 1.6

THEODORE DAVIS*

United Aircraft Corporation

Abstract

Downwash and sidewash angles were measured with a conical probe in vertical planes 0.5, 1.0, and 1.5 chord lengths downstream of a rectangular wing of biconvex section. Finely spaced measurements were taken to determine the downwash field in the region of steepest gradients, with the result that the rolling up of the vortex sheet was well defined. The experimental results are compared with the theoretical solutions calculated from the measured wing loading.

The Mach Number and dynamic pressure in the empty tunnel and behind the wing were also determined. The free-stream Mach Number was 1.60, and the Reynolds Number, based on wing chord, was 0.58×10^6.

List of Symbols

b	= span of wing including image; span of vortex line
q	= dynamic pressure
M	= Mach Number
s	= surface distance along wing in x direction
u_0	= stream velocity in x direction
u	= velocity perturbation in x direction
v	= velocity perturbation in y direction
w	= velocity perturbation in z direction
x, y, z	= coordinates of point at which downwash is wanted
x', y', z'	= coordinates of point expressed in per cent semispan of wing; as $x' = x/(b/2)$
α	= wing angle of attack
β	= $\sqrt{M^2 - 1}$
Γ	= vorticity $\oint u\, ds$

Introduction

Knowledge of the flow field behind the lifting surfaces of a supersonic airplane or missile is important in handling the various stability problems that arise. Several references are available which predict, by means of linearized theory, the downwash and sidewash behind wings of various plan forms. Each of these theories is subject to the limitations of small angles of attack and a nonviscous fluid, with the result that the downwash region directly behind the wing tip is shown as a discontinuity.

In order to provide basic experimental data on the subject, a program was established at the U.A.C. Research Department to measure the downwash and sidewash angles at various stations behind a straight rectangular wing.

Received December 12, 1950. Revised and received November 15, 1951.

* Aeronautical Research Engineer, Research Department.

The complete results of these investigations, which are too extensive for publication herein, are presented in reference 1. Representative results obtained from the test program and a discussion of the principal aspects of the instrumentation problems are presented in this paper.

Description of Test Equipment

Tunnel

The test program was conducted in the U.A.C. Research Department 8- by $9^1/_4$-in. supersonic wind tunnel at a nominal free-stream Mach Number of 1.60. This wind tunnel is a vacuum-type, continuous-operation channel powered by two turboblowers driven by two 300-hp. electric motors. Condensation control at this Mach Number was obtained by recirculating enough of the tunnel flow to raise the total temperature to approximately 200°F.

Models

The model and probe were mounted on the sidewall of the wind tunnel as shown in Fig. 1. The rectangular wing was 6 per cent thick with a 2.0-in. chord and a 2.7-in. semispan. The section was biconvex with the maximum thickness located at 50 per cent of the chord. The angle of attack was controlled to within 0.10° by means of a screw-driven protractor keyed to a shaft attached to the model.

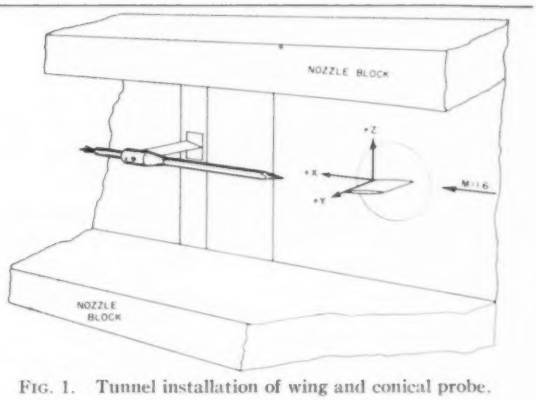

Fig. 1. Tunnel installation of wing and conical probe.

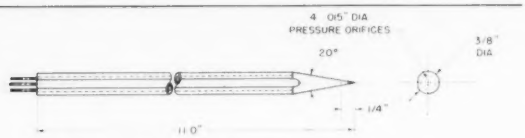

FIG. 2. Sketch of four-orifice conical probe.

Conical Probe

The conical probe shown in Figs. 1 and 2 had a total apex angle of 20° and was equipped with four 0.015-in. pressure orifices spaced 90° apart in a plane 0.25 in. from the apex of the cone. The leads from the orifices were connected to water U-tube manometers in diametric pairs and were also connected to a mercury manometer. The water manometer was used to indicate the pressure difference across the cone in the downwash and sidewash planes, and the mercury manometer was used to measure the average cone surface pressure. The cone was calibrated at Mach Numbers of 1.50, 1.60, and 1.70 over a range of yaw angles from $-5°$ to $+10°$. It was found that the slope of the calibration curves was essentially constant and independent of Mach Number over the range of interest.

TEST PROCEDURE AND ANALYSIS OF DATA

A survey of the flow in the empty tunnel at all the probe locations was made with both conical and total head probes. The wing was then installed, and the survey was repeated for wing angles of attack of 0°, 3°, and 6°. Finely spaced downwash measurements were taken in the region directly behind the wing tip.

The downwash and sidewash angles were determined from the probe readings and the probe calibration curves. The data were corrected for tare flow conditions by subtracting the angles for empty tunnel flow from those measured behind the wing.

The Mach Number at each test point was determined from a composite curve of the ratio of pitot pressure to cone surface pressure. With the Mach Number known, it was possible to determine the static pressure and the dynamic pressure.

DISCUSSION OF RESULTS

Conical Probe Calibration

Since total head readings were desired for use with the average cone pressure in the calculation of Mach Number, the feasibility of incorporating a total head tube into the cone was investigated. It was found that, for the 20° cone angle with the static orifices located close to the apex, the presence of the total head orifice caused a significant change in average cone surface pressure.*

* Conical probes that can be used to measure the true surface pressure and pitot pressure simultaneously have since been developed.

The validity of the average cone pressure and pitot pressure measurements may be questioned when the readings are taken in a stream having downwash and sidewash components. The effect of yaw on the reading of a pitot probe was checked in the supersonic wind tunnel, and it was found that 10° of yaw produced a change of 4 per cent in the measured pitot pressure. Similar calibrations of the cone indicated that the maximum change in average cone pressure was 2.85 per cent of the pressure measured with the probe aligned with the air stream. Since both changes at angle of attack were in the negative direction, the net change in the ratio of the pitot and static pressures was 1.3 per cent, which resulted in a difference of less than 0.001 in the calculated Mach Number. Subject to these limitations, the use of the total head pressure and the average cone pressure without correcting for the downwash and sidewash angles was justified for the measurement of Mach Number.

Downwash and Sidewash

The downwash data that best indicate the suitability of the test techniques were obtained in the x-y plane of Fig. 1 at $z = 0$ where the steepest gradients were encountered. The downwash angles measured in this plane at stations 0.5, 1.0, and 1.5 chord lengths down-

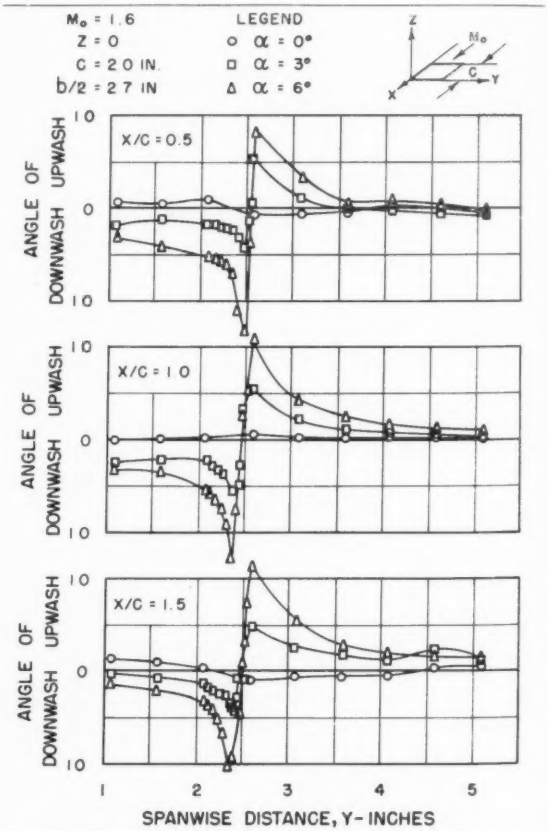

FIG. 3. Downwash distribution behind a rectangular wing.

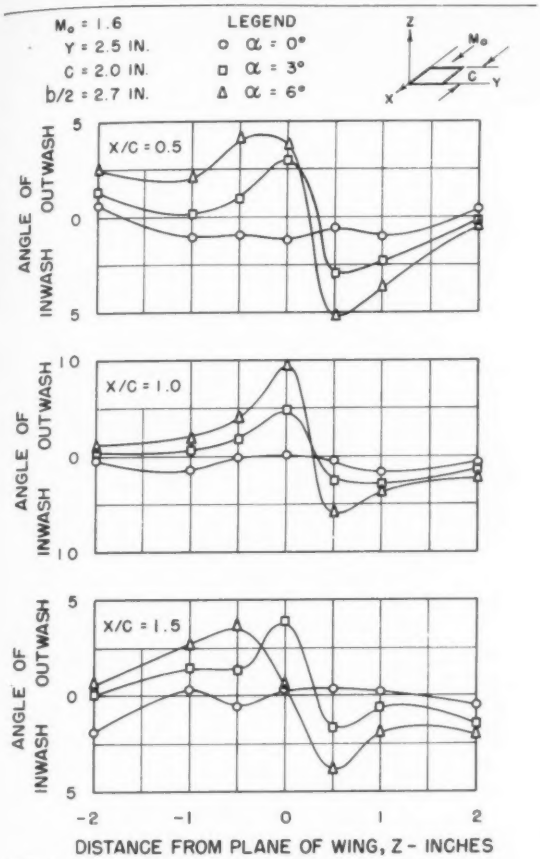

FIG. 4. Sidewash distribution behind a rectangular wing.

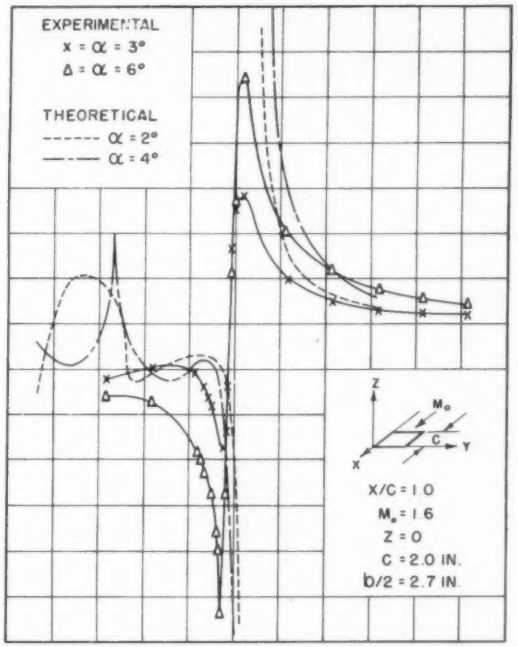

FIG. 6. Comparison of theoretical and experimental downwash distribution behind rectangular wing.

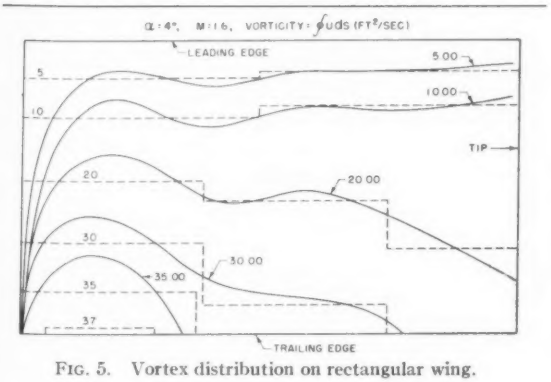

FIG. 5. Vortex distribution on rectangular wing.

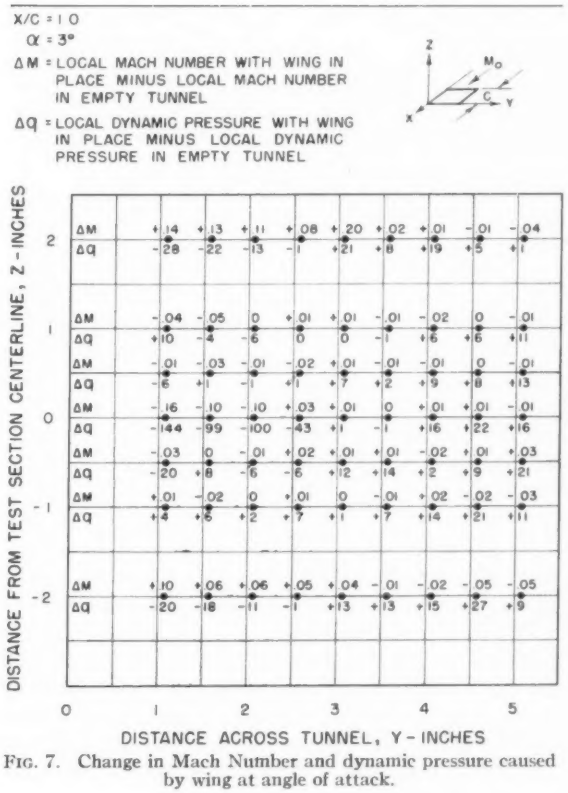
X/C = 1.0
α = 3°
ΔM = LOCAL MACH NUMBER WITH WING IN PLACE MINUS LOCAL MACH NUMBER IN EMPTY TUNNEL
ΔQ = LOCAL DYNAMIC PRESSURE WITH WING IN PLACE MINUS LOCAL DYNAMIC PRESSURE IN EMPTY TUNNEL
DISTANCE FROM TEST SECTION CENTERLINE, Z - INCHES
DISTANCE ACROSS TUNNEL, Y - INCHES

FIG. 7. Change in Mach Number and dynamic pressure caused by wing at angle of attack.

stream of the trailing edge are shown in Fig. 3. In order to define the transition region between downwash and upwash, the spacing between probe settings was reduced from $^1/_2$ in. to as little as $^1/_{32}$ in. Even with points so closely spaced, the absolute maximum values of the downwash and upwash angles were not established because there were regions less than a $^1/_{16}$ in. wide where the indicated angle varied as much as 7° or 8°.

The sidewash angles downstream of the wing are plotted against distance above and below the plane of the wing at the 92 per cent span station in Fig. 4. The closely spaced probe settings used for downwash were not repeated for these tests, but it is believed that sidewash gradients steeper than those shown did exist. It should be noted that the angle scale at the 1.0 chord station is twice that for the $^1/_2$ and $1^1/_2$ chord-length stations. In general, the sidewash angles are in agreement with what would be expected from consideration of the vortex pattern.

Theoretical Considerations

Most of the theoretical solutions for the downwash are based on the assumption of an ideal uniform distribution of lift on the wing. Since the experimental lift distribution is not in agreement with the theoretical loading as a consequence of nonuniform velocity distribution in the wind tunnel or interference flow from a body, the experimental values of downwash often differ from those predicted from theory. A method of calculating downwash from a known wing loading was developed by Smith in reference 2, and this method was used for the comparison with the experimental results presented in this paper. Reference 2 is a further development of Schlichting's work on this subject reported in reference 3.

The wing loading was determined experimentally from a field of pressure taps incorporated into the wing. This loading was then applied to the determination of the vorticity, as follows: On the basis of a linear approximation, the measured pressure coefficient, C_p, may be expressed in terms of the free-stream velocity, u_0, and the perturbation velocity, u, as

$$C_p = 2[1 - (u/u_0)] \tag{1}$$

Solving Eq. (1) for u,

$$u = u_0[1 - (C_p/2)] \tag{2}$$

The experimental pressure coefficients were substituted in Eq. (2), and the values of u at various chord stations were calculated. These velocities were then plotted against the chord, s, and the various line integrals, $\oint u\, ds = \Gamma$, were evaluated graphically. The path of integration was from the leading edge, over and through the wing, and back to the leading edge. The values of Γ for an angle of attack of 4° are plotted on a layout of the wing in Fig. 5. Lines of constant vorticity are drawn through points having equal values of Γ. Since the lift distribution was not constant, the lines were curved, and it was necessary to approximate them with straight-line segments parallel to the leading edge. A total of 28 horseshoe vortices were used in obtaining the solution for the downwash. The downwash was then calculated from the equation

$$w = \frac{\Gamma}{\pi b}\left[\frac{\sqrt{x'^2 - \beta^2(y'-1)^2}}{x'(y'-1)} - \frac{\sqrt{x'^2 - \beta^2(y'+1)^2}}{x'(y'+1)}\right] \tag{3}$$

A grid, giving the values inside the brackets for various points relative to the vortex line, was prepared for use with this problem.

An important advantage of this theoretical treatment is that it considers the effect of the mirror image of the wing at the tunnel wall and thus accounts for the root Mach cone. The method also gives a solution based on a measured, rather than an assumed, wing loading.

The theoretical downwash in the plane of the wing one chord length downstream from the trailing edge for angles of attack of 2° and 4° was calculated by the wing loading method and is plotted in Fig. 6. The lines of constant vorticity were carried straight to the wing tip because insufficient pressure measurements were available to justify fairing the data inboard of the tip. As a consequence of this assumed distribution of vorticity, the center of the vortex is shown directly downstream of the tip instead of slightly inboard as indicated by the experimental data also shown in Fig. 6 for angles of attack of 3° and 6°. The variations of theoretical downwash inboard of the tip are attributed to variations in wing loading. The pressure measurements indicated a dip in the spanwise loading curve at 45 per cent span which lead to an upwash in the calculated flow distribution behind this region. Unfortunately, it was impossible to check the points less than an inch from the wall because of the limitations imposed by the dimensions of the downwash probe.

Mach Number and Dynamic Pressure

The change in Mach Number and dynamic pressure distribution with the wing installed at 3° angle of attack is shown in Fig. 7, where a minus sign indicates a decrease from the empty tunnel condition. It is readily apparent from this plot that the primary disturbance is in the wake of the wing. The points along the horizontal tunnel centerline are actually slightly above the wake centerline and, hence, do not show the maximum variations existing in the wake.

Conclusions

On the basis of the overall results, some conclusions about the nature of supersonic downwash may be drawn. The flow field behind a wing is greatly influenced by the

(*Continued on page 340*)

Supersonic Wing-Body-Tail Interference*

GEORGE MORIKAWA†
Hughes Aircraft Company

Abstract

The study of wing-body-tail interference is generally complicated by nonlinear effects, particularly in the description of the flow field behind lifting surfaces. In this paper, these difficulties are avoided by restricting the study to angle of attack near zero for in-line configurations in which both wing and tail lie nominally in the same horizontal plane. Comparison of interference effects on the tail due to the two *limiting* representations of the flow field behind lifting wings—namely, the vortex sheet and line vortex—shows the same qualitative behavior for the limiting cases of the design parameters. Thus, the indications are that this analysis, which essentially yields the *maximum* interference, may be applied to predict the behavior of configurations in which the tail is not in the same plane as the wing—i.e., where the maximum interference occurs at nonzero angle of attack.

Notation

a = radius of body
A.R. = aspect ratio
i = $\sqrt{-1}$
$l(x)$ = spanwise lift distribution
L = lift
L_I = interference lift on tail-body for configuration and flow field given by (C) in Fig. 3
m = ratio of tangent of leading edge angle (measured from free-stream direction) to tangent of Mach angle
M = free-stream Mach Number
q = free-stream dynamic pressure
s = lifting surface semispan measured from body centerline
W = free-stream velocity
x = spanwise coordinate
y = vertical coordinate normal to plane of wing or tail
z = $x + iy$, cross-flow plane in complex variable notation
z_0 = line vortex position in first quadrant of z-plane
α = angle of attack
α_0 = angle of attack of body
β = $\sqrt{M^2 - 1}$
Γ = line vortex strength
ζ = transformed plane (see Fig. 7)
η = efficiency
λ = a/s, diameter-span ratio
λ_0 = a/x_0, diameter-line vortex span ratio
μ = $\text{ctn}^{-1}\sqrt{M^2 - 1}$, Mach angle measured from free-stream direction
φ = velocity potential in cross-flow plane
ψ = stream function in cross-flow plane

Subscripts

W = pertains to wing
T = pertains to tail

Received September 17, 1951.

* The author wishes to acknowledge the interest and subsequently helpful suggestions and criticisms received from R. H. Edwards, A. E. Puckett, and J. L. Fredrick, of the Research and Development Laboratories, Hughes Aircraft Company.

† Missile Aerodynamics Section, Research and Development Laboratories.

Introduction

THE *general* STUDY OF supersonic wing-body-tail interference is inherently one involving *nonlinear effects* even for relatively small angles of attack, say $\alpha < 10°$. For finite lifting systems, these effects are due primarily, directly or indirectly, to viscosity. Consider a typical lifting system like that shown in Fig. 1, consisting of a slender body, a forward lifting system (wing), and an aft lifting system (tail). For certain relative positions of body nose, wing, and tail, each component part of the total configuration can be studied separately, and the indications are that a satisfactory correspondence exists between experiment and linearized theory. However, in many cases, aerodynamic interference is unavoidable, and, hence, it is essential to minimize any adverse effects. From momentum considerations, it is evident that any finite lifting system will induce a flow field that will affect a lifting system placed downstream of it. Behind the sharp trailing edge of a wing, but in its vicinity, experiments indicate that a vortex sheet well represents the flow field, but farther downstream a continuous rolling-up of the sheet generally takes place. This is a nonlinear process that is difficult to describe; the most recent attempts, with due reference to previous work, are found in references 1 and 2. Even the description of the two-dimensional motion of line vortices (or fully rolled-up vortices) in the presence of a circular cylinder is difficult if more than two vortices, symmetrically placed with respect to the free-stream direction, are involved.

The present investigation avoids these difficulties by restricting the study to angle of attack α near zero, the analysis being pertinent then for in-line configurations, in which both wing and tail lie nominally in the same horizontal plane (within the validity of linearized theory) passing through the body axis. Then, with the possible exception of the viscous wake interference, stationary linearized theory is applicable.

Formulation of Problem

In order to make the aerodynamics of the configuration shown in Fig. 1 mathematically tenable, yet holding to reasonable assumptions, some essential simplifications can be made. The principal condition that is imposed is that the configuration and flow field can be separated into component parts and analyzed separately—a general procedure that is inherent in the analyses of practically all physical problems but which must

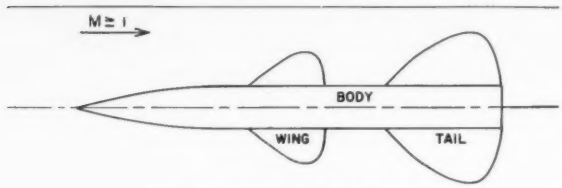

FIG. 1. Typical configuration.

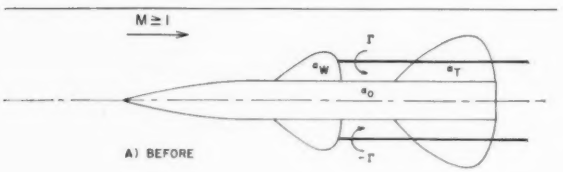

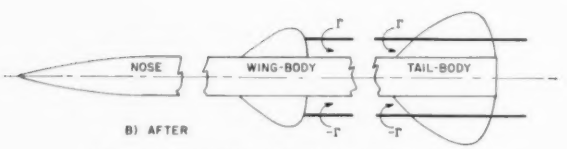

FIG. 2. Separation of typical configuration.

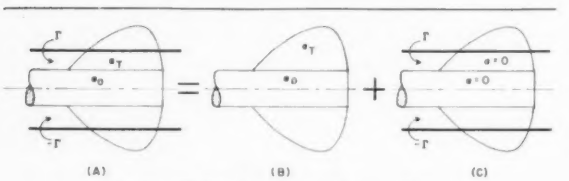

FIG. 3. Tail-body superposition scheme.

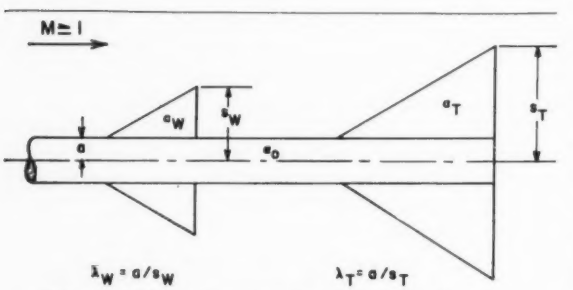

FIG. 4. Delta wing-body-delta tail configuration.

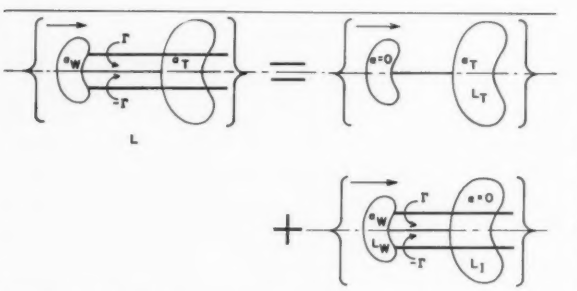

FIG. 5. Total lift superposition scheme, $L = L_W + L_T + L_I$.

always be performed with great care. The configuration to be studied is shown in Fig. 2a, where the line vortices schematically represent the flow disturbance created by the wing. Then, in many cases, the configuration can be separated into the components shown in Fig. 2b.

The separation of nose and wing-body is feasible only if the flow field itself can be separated in a simple manner—for example, if complete information is known in the cross-flow plane at the separation. Such is the case if the nose disturbance can reasonably be assumed to be at $-\infty$ with respect to the wing-body, so that the flow field in the cross-flow plane at the separation is that for flow past an infinitely long cylinder. Similarly, the wing-body and tail-body can be separated. The aerodynamics of the wing-body without afterbody is given in reference 3, and some progress has been made in the difficult analysis of the flow field around the afterbody in reference 2. In the present analysis for $\alpha \to 0$, the flow disturbance created by the wing is represented by *either* an unwarped vortex sheet *or* line (fully rolled-up) vortices that remain in the plane of the wing. Then the wing-body-tail interference problem is reduced to the study of the tail-body with given flow discontinuities. By linearization, this problem can be reduced further by superposition, as shown in Fig. 3. For the lifting problem—i.e., body angle of attack, $\alpha_0 = \alpha_T$ (tail angle of attack)—part (B) of Fig. 3 reduces to the problem given in reference 3; the wing-body-tail interference problem finally reduces to that given by part (C) of Fig. 3.

The present study is restricted to the aerodynamics of a configuration consisting of a semiinfinitely long circular cylinder, a delta wing, and a delta tail with no afterbody, although part of the analysis—namely, that given by slender body theory—is directly applicable to plan forms of arbitrary-shaped leading edges and straight trailing edges normal to the free-stream direction. The analysis can easily be generalized to cylindrical bodies of other shapes and wing and tail plan forms with straight edges in a manner similar to that described in reference 3.

DELTA TAIL-BODY LIFT DUE TO DELTA WING-BODY INTERFERENCE

(1) *Parametric Representation*

Taking the same general point of view as expressed in reference 3, certain limiting cases of the aerodynamic parameters are considered, from which some insight for the more difficult analysis over the entire range of the parameters is obtained. Consider the simplified configuration at angle of attack α_0, α_W, and α_T, as shown in Fig. 4. The basic parameters for this family of delta wing-, delta tail-body combinations are $\beta \equiv \text{ctn } \mu = \sqrt{M^2 - 1}$, λ_W, λ_T, m_W, and m_T, where μ is the Mach angle, $\lambda \equiv a/s$ is the diameter-span ratio, m is

TABLE 1
Limiting Cases

Case	I	II	III	IV
m_W	0	0	∞	∞
m_T	0	∞	0	∞

the ratio of the tangents of the leading edge angle to the Mach angle, and the subscripts correspond to wing and tail, respectively. Again, as in reference 3, the basic aerodynamic variable is taken as the *ratio* of specified lifts, so that there is no Mach Number dependence explicitly—i.e., β is eliminated. The limiting cases are given by the limiting values of the parameter $m = 0, \infty$, where $m = 0$ implies slender body theory and $m = \infty$ implies strip theory. Then there are four possible cases given by $m_W = 0$ with $m_T = 0, \infty$ and $m_W = \infty$ with $m_T = 0, \infty$. For a more familiar geometrical interpretation of the parameter m, note that, for a delta wing alone, $m = \beta$A.R./4; βA.R. is called the effective aspect ratio. Of the four limiting cases, the two cases given by $m_W = 0$ with $m_T = 0, \infty$ are of more interest, since (1) for $m_W = \infty$ with $m_T = 0$, the interference lift approaches zero like $1/m_W$ as $m_W \to \infty$, and (2) for $m_W = \infty$ with $m_T = \infty$, the interference lift approaches zero like $1/(m_W \cdot m_T)$ as $m_W, m_T \to \infty$. However, the last two cases are by no means trivial, and some remarks will be made about them later. Table 1 earmarks the four limiting cases.

(2) *Representation of Interference Lift*

The interference lift L_I can be presented in several different forms (lift ratios), each of which is useful in the various considerations necessary in the design analysis of efficient stable configurations. The lifts pertinent to a useful representation are easily visualized by the superposition scheme in Fig. 5, where the body is eliminated to simplify the discussion; L_W, L_T, and L_I generally include body lift. Then the interference lift L_I may be represented by the following lift ratios:

$$(-L_I/L_T) \equiv (1 - \eta_T) \tag{1a}$$

where η_T is defined as the tail efficiency;

$$(-L_I/L_W) \equiv (1 - \eta_W) \tag{1b}$$

where η_W is defined as the wing efficiency;

$$[-L_I/(L_W + L_T)] \equiv (1 - \eta) \tag{1c}$$

where η is defined as the total lifting surface efficiency; and

$$\left(-\frac{L_I}{L_W L_T}\right) \equiv \frac{(1 - \eta_W)}{L_T} = \frac{(1 - \eta_T)}{L_W} \tag{1d}$$

The lift ratio given by Eq. (1d) is usually made dimensionless by expressing either L_T or L_W as a lift coefficient based on the body cross-sectional area.* It is noted also that $(1 - \eta_W)$ given by Eq. (1b) is the only true efficiency ratio—i.e., $0 \leq (1 - \eta_W) \leq 1$—this is evident from momentum considerations. In addition, for the line vortex representation of the wing disturbance, $(1 - \eta_W)$ [and, hence, $(1 - \eta_W)/L_T$] can be expressed independent of the vortex strength—i.e., independent of the wing loading and geometry. Thus, these lift ratios afford a somewhat more general interpretation of interference lift.

* To the author's knowledge, A. E. Puckett and I. Naiman first introduced this ratio and have used it effectively in the design of high-speed configurations.

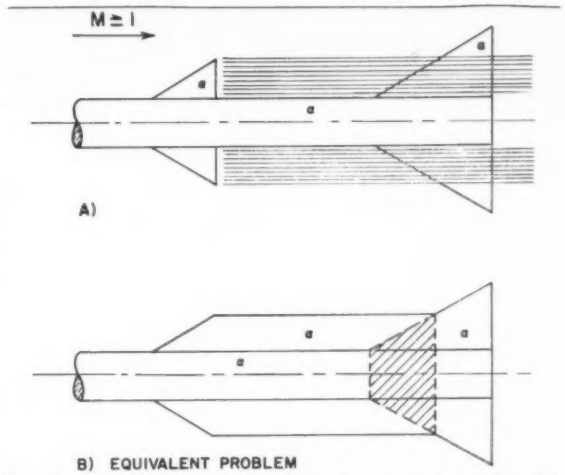

FIG. 6. Case I with vortex sheet and equivalent problem for $\lambda_T \leq \lambda_W$.

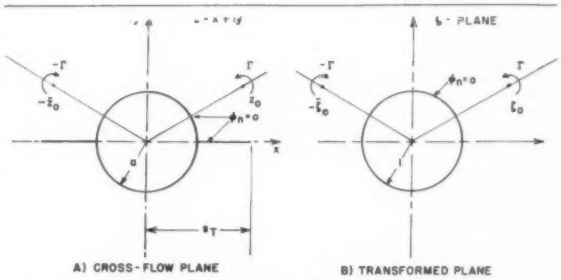

FIG. 7. Cross-flow plane for Case I with line vortices.

TABLE 2
Identically Zero Lift Ratios

Case	I	II	III	IV
$(1 - \eta_T)$	...	...	0	0
$(1 - \eta_W)$	...	0	...	0
$(1 - \eta)$	...	0	0	0
$\dfrac{(1 - \eta_W)}{L_T}$	...	...	...	...

Table 2 clearly shows that limiting Case I gives the maximum nonzero information for all lift ratios and that

$$(1 - \eta_W)/L_T \equiv (1 - \eta_T)/L_W$$

yields the maximum nonzero information in the com-

parison of the limiting cases. Most of the present analysis is presented in terms of $(1 - \eta_T)$ and $(1 - \eta_W)$, both having simple physical interpretations.

(3) *Case I* ($m_W = m_T = 0$) *with Vortex Sheet*

Unless otherwise stated, the lifting problem with $\alpha_0 = \alpha_W = \alpha_T$ is considered. Referring to Fig. 6, this limiting case, assuming an unwarped vortex sheet, has a particularly simple solution (slender body theory), and comparison with other limiting cases (in particular, Case I with line vortices) is especially instructive. For $\lambda_T \leq \lambda_W$ (tail span greater than wing span), the difference between the total lift of the equivalent problem, and the total lift *without interference* is clearly the lift on the cross-hatched area in Fig. 6b. Then the interference lift is exactly the wing lift L_W. Similarly for $\lambda_T \geq \lambda_W$, the interference lift is the tail lift L_T. Thus,

$$\left.\begin{aligned} \frac{L_I}{q\alpha} &= \frac{-L_W}{q\alpha} = -2\pi a^2 \left(\frac{1 - {\lambda_W}^2}{\lambda_W}\right)^2 \\ &\qquad (\text{for } \lambda_T \leq \lambda_W) \\ \frac{L_I}{q\alpha} &= \frac{-L_T}{q\alpha} = -2\pi a^2 \left(\frac{1 - {\lambda_T}^2}{\lambda_T}\right)^2 \\ &\qquad (\text{for } \lambda_T \geq \lambda_W) \end{aligned}\right\} \tag{2a}$$

and

$$\left.\begin{aligned} (1 - \eta_T) &= \left(\frac{\lambda_T}{1 - {\lambda_T}^2}\right)^2 \left(\frac{1 - {\lambda_W}^2}{\lambda_W}\right)^2 \\ &\qquad (\text{for } \lambda_T \leq \lambda_W) \\ &= 1 \qquad (\text{for } \lambda_T \geq \lambda_W) \end{aligned}\right\} \tag{2b}$$

The other lift ratios are obtained simply [cf. Eq. (1)].

(4) *Case I with Line Vortices*

Since slender-body theory is applicable for this case, the analysis is reduced to a two-dimensional potential problem in the cross-flow plane (cf. reference 4). Then the problem for interference lift given by Part (C) of Fig. 3 becomes that shown in Fig. 7a, where the usual complex variable notation is used—i.e., $z = x + iy$. The vortex strength is denoted by Γ (positive counterclockwise), and the boundary condition is that the velocity φ_n normal to the surface is zero on body and tail. Then, by symmetry about the y-axis, the problem for the right half-plane is analogous to that of finding a Green's function. This is most simply accomplished by transforming the tail-body into a circle, as shown in Fig. 7b, and using the known reflection properties on the circle in order to satisfy the boundary conditions. The transformation $z \rightarrow \zeta$ is easily seen to be

$$\left(z + \frac{a^2}{z}\right) = \frac{1}{2}\left(s + \frac{a^2}{s}\right)\left(\zeta + \frac{1}{\zeta}\right) \tag{3}$$

and the solution for the complex potential in the ζ-plane is

$$\varphi + i\psi = -\frac{i\Gamma}{2\pi} \ln \left\{\frac{(\zeta - \zeta_0)[\zeta + (1/\zeta_0)]}{[\zeta - (1/\zeta_0)](\zeta + \zeta_0)}\right\} \tag{4a}$$

Writing $A = [s + (a^2/s)]$ for convenience and transforming back to the cross-flowplane, the argument of the log becomes

$$\frac{(\zeta - \zeta_0)\left(\zeta + \frac{1}{\zeta_0}\right)}{\left(\zeta - \frac{1}{\zeta_0}\right)(\zeta + \zeta_0)} = \frac{\left(\zeta - \frac{1}{\zeta}\right) - \left(\zeta_0 - \frac{1}{\zeta_0}\right)}{\left(\zeta - \frac{1}{\zeta}\right) + \left(\zeta_0 - \frac{1}{\zeta_0}\right)} \tag{4b}$$

Then on the tail or body ($z = x$, $a \leq x \leq s$; or $z = ae^{i\theta}$), the denominator of the argument is the complex conjugate of the numerator, and the potential on the tail is

$$\varphi(x, 0; z_0) = \frac{\Gamma}{\pi} \tan^{-1} \left\{ \frac{Im \sqrt{1 - (1/A^2)[z_0 + (a^2/z_0)]^2}}{\sqrt{1 - \frac{1}{A^2}\left(x + \frac{a^2}{x} + Rl \sqrt{1 - \frac{1}{A^2}\left(z_0 + \frac{a^2}{z_0}\right)^2}\right.}} \right\} \tag{5a}$$

where Rl and Im denote the real and imaginary parts of the radical expression. If the vortices are in the plane of the wing ($z_0 = x_0$), then for $x_0 \leq s$ the imaginary part is identically zero and for $x_0 > s$ the real part is zero. Thus, in the λ notation,*

$$\left.\begin{aligned} \varphi(\lambda, \lambda_T; \lambda_0) &= 0 \qquad (\text{for } \lambda_T \leq \lambda_0) \\ &= \frac{\Gamma}{\pi} \tan^{-1} \left[\frac{\lambda}{\lambda_0} \sqrt{\frac{({\lambda_T}^2 - {\lambda_0}^2)(1 - {\lambda_0}^2{\lambda_T}^2)}{(\lambda^2 - {\lambda_T}^2)(1 - {\lambda_0}^2\lambda^2)}}\right] \qquad (\text{for } \lambda_T > \lambda_0) \end{aligned}\right\} \tag{5b}$$

Similarly, on the body ($z = a^{i\theta}$),

$$\left.\begin{aligned} \varphi(x, \lambda_T; \lambda_0) &= 0 \qquad (\text{for } \lambda_T \leq \lambda_0) \\ &= \frac{\Gamma}{\pi} \tan^{-1} \left[\frac{1}{\lambda_0} \sqrt{\frac{({\lambda_T}^2 - {\lambda_0}^2)(1 - {\lambda_0}^2{\lambda_T}^2)}{(1 + {\lambda_T}^2)^2 - {\lambda_T}^2(x^2/a^2)}}\right] \qquad (\text{for } \lambda_T > \lambda_0) \end{aligned}\right\} \tag{6}$$

* Note that here and in the integration [cf. Eq. (8a)] λ denotes the running variable a/x.

It should be noted that Eqs. (5b) and (6) state that the velocity potential φ is identically zero *downstream* of the cross-hatched area shown in Fig. 8 and thereby imply that the lift is nonzero only on the cross-hatched area when the line vortices lie in the plane of the tail.* Also a comparison with the results of Case I with the vortex sheet (cf. Fig. 6b) shows an analogous behavior. The interference lift can be expressed as an integral of the velocity potential, since

$$\frac{L}{q} = 2\int_a^s \left[\frac{l(x)}{q}\right] dx \equiv \frac{8}{W}\int_a^s \left(\int_{\text{t.e}}^{\text{t.e}} \varphi_z\, dz\right) dx = \frac{8}{W}\int_a^s [\varphi(\text{t.e.}) - \varphi(\text{l.e.})]\, dx \tag{7}$$

where (l.e.) and (t.e.) denote the leading and trailing edges, respectively, and W is the free-stream velocity.†

Then the wing portion of the interference lift, combining Eqs. (5b) and (7), is

$$\left.\begin{aligned} L_I^{(W)}/q &= -4(a\cdot\Gamma/W)[(1-\lambda_0)/\lambda_0] \qquad (\text{for } \lambda_T \le \lambda_0) \\ \frac{L_I^{(W)}}{q} &= -\frac{8}{\pi}\left(\frac{a\cdot\Gamma}{W}\right)\int_{\lambda_T}^1 \tan^{-1}\left[\frac{\lambda_0}{\lambda}\sqrt{\frac{(\lambda^2-\lambda_T^2)(1-\lambda_0^2\lambda^2)}{(\lambda_T^2-\lambda_0^2)(1-\lambda_0^2\lambda_T^2)}}\right]\frac{d\lambda}{\lambda^2} \\ &\qquad\qquad (\text{for } \lambda_T \ge \lambda_0) \end{aligned}\right\} \tag{8a}$$

and combining Eqs. (6) and (7), the body portion of the interference lift is

$$\left.\begin{aligned} \frac{L_I^{(B)}}{q} &= -\frac{8}{\pi}\left(\frac{a\cdot\Gamma}{W}\right)\int_0^a \tan^{-1}\left[\frac{1-\lambda_0^2}{2\lambda_0}\sqrt{\frac{1}{1-(x^2/a^2)}}\right]\frac{dx}{a} \quad (\text{for } \lambda_T \le \lambda_0) \\ &= +\frac{8}{\pi}\left(\frac{a\Gamma}{W}\right)\int_0^a \left\{\tan^{-1}\left[\frac{1}{\lambda_0}\sqrt{\frac{(\lambda_T^2-\lambda_0^2)(1-\lambda_0^2\lambda_T^2)}{(1+\lambda_T^2)^2-4\lambda_T^2(x^2/a^2)}}\right] - \right. \\ &\qquad \left. \tan^{-1}\left[\frac{1-\lambda_0^2}{2\lambda_0}\sqrt{\frac{1}{1-(x^2/a^2)}}\right]\right\}\frac{dx}{a} \quad (\text{for } \lambda_T \ge \lambda_0) \end{aligned}\right\} \tag{8b}$$

Integrating by parts, Eq. (8a) can be reduced to standard elliptic integrals.

Both integrals of Eq. (8b) are of the form

$$I = \int_0^1 \tan^{-1}(B/\sqrt{C^2-x^2})\, dx$$

where B and C are constants with respect to the integration. Integrating by parts,

$$I = \tan^{-1}\left(\frac{B}{\sqrt{C^2-1}}\right) + B\tan^{-1}\left(\frac{1}{\sqrt{C^2-1}}\right) - \frac{\sqrt{B^2+C^2}}{2}\tan^{-1}\left[\frac{2B\sqrt{(B^2+C^2)(C^2-1)}}{(B^2+C^2)(C^2-2)+C^2}\right] \tag{8c}$$

The simpler of the two integrals on the right side of Eq. (8b) has a particularly simple solution,

$$\frac{2}{\pi}\int_0^1 \tan^{-1}\left(\frac{1-\lambda_0^2}{2\lambda_0}\sqrt{\frac{1}{1-x^2}}\right)dx = (1-\lambda_0) \tag{8d}$$

The total interference lift, adding Eqs. (8a) and (8b), is

$$L_I/q = (L_I^{(W)} + L_I^{(B)})/q \tag{8e}$$

* This is easily visualized by considering a two-dimensional line vortex near a plane wall and evaluating the velocity potential in the limit as the distance between vortex and wall approaches zero.

† Note that the free-stream direction is here denoted by z; elsewhere it is the usual complex variable.

The interference lift is in relatively general form, since it is expressed in terms of vortex strength Γ and position λ_0. For the particular case of a delta wing with $m_W = 0$, the relationship between (1) wing loading and geometry and (2) Γ and λ_0 is necessary. Recalling the assumption (for $\alpha \to 0$) that the rolling-up process of the vortex sheet behind the wing is such that the fully rolled-up vortices (line vortices) remain in the plane of wing and tail, it is easily seen that the lateral center of gravity of the vortex sheet on either side of the body remains invariant in the downstream direction. This implies that each line vortex on either side of the body

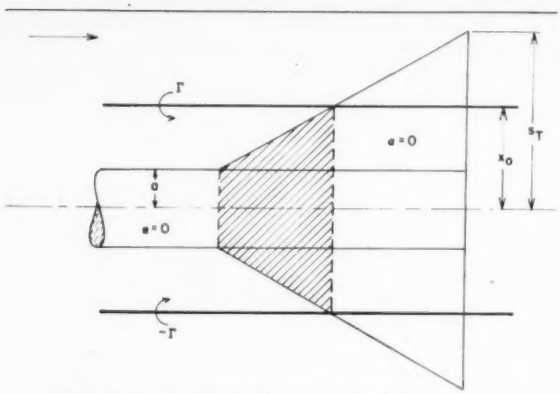

FIG. 8. Case I with line vortices in plane of tail.

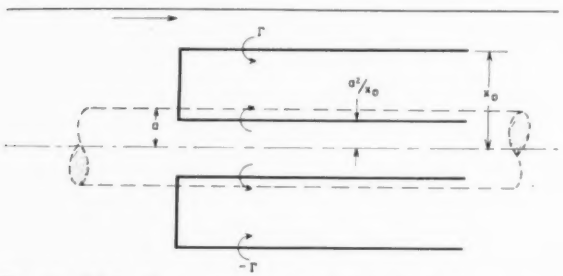

FIG. 9. Lifting line representation of wing-body for $m_W = 0$.

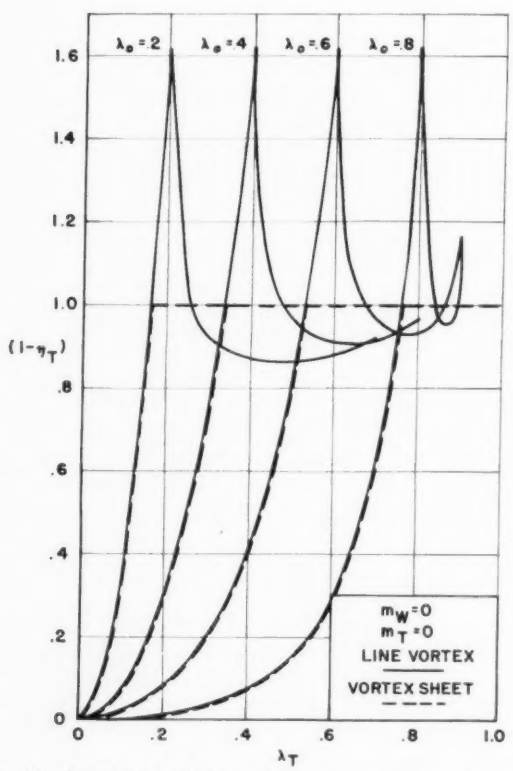

FIG. 10. Comparison of $(1 - \eta_T)$ for Case I with vortex sheet and Case I with line vortices.

is exactly at the center of gravity position of the vortex sheet. Thus, a relationship is found between the line vortex position x_0 and the spanwise vorticity distribution at the trailing edge of the wing, and the vortex strength is directly related to the spanwise lift evaluated at the root chord of the wing (Kutta-Joukowski law).

The reflected vortex inside the body is at the inverse point a^2/x_0. Then calculating the body portion of the total wing lift corresponding to this line vortex spacing indicates that a lifting-line representation of the wing-body, as shown in Fig. 9, yields a good approximation to the total lift and also gives a reasonable approximation to the wing disturbance some distance behind the trailing edge satisfying the body boundary conditions. Since the calculations are somewhat simpler, the vortex spacing given by the lifting-line representation is used. Then the total lift is given by

$$\left.\begin{aligned} L/q &= [2al(a)/q][(1 - \lambda_0^2)/\lambda_0] \\ &= (4a\Gamma/W)[(1 - \lambda_0^2)/\lambda_0] \end{aligned}\right\} \tag{9a}$$

since, by the Kutta-Joukowski law,

$$l(a)/q = 2\Gamma/W \tag{9b}$$

Since the spanwise lift at the root chord of the wing for $m_W = 0$ is

$$l(a)/q\alpha = 4a[(1 - \lambda_W^2)/\lambda_W] \tag{9c}$$

and the total lift for $m_W = 0$ is

$$\frac{L_W}{q\alpha} = 2\pi a^2[(1 - \lambda_W^2)/\lambda_W]^2 \tag{9d}$$

the relationship between wing span and vortex spacing is given by

$$[(1 - \lambda_W^2)/\lambda_W] = \frac{4}{\pi}[(1 - \lambda_0^2)/\lambda_0] \tag{9e}$$

Since the wing lift L_W and the tail lift (without interference) L_T for $m_T = 0$ is given by Eq. (9d) (using the proper subscript for the tail), the lift ratios given by Eq. (1) can be expressed in terms of λ_0 [or λ_W by Eq. (9e)] and λ_T. A comparison of $(1 - \eta_T)$ for Case I with vortex sheet and Case I with line vortices is shown in Fig. 10. A marked similarity between the two representations is shown. In fact, the two cases are identical for $\lambda_T \leq \lambda_W$. The difference is found for $\lambda_T \geq \lambda_W$ (tail span $\leq$ wing span), where for the vortex sheet representation the tail is completely ineffective—i.e. $(1 - \eta_T) = 1$—and for the line vortex representation the maximum interference* (more than 100 per cent ineffective) in the interior region, $0 < \lambda_T < 1$, occurs at $\lambda_T = \lambda_0$ and has a minimum $(1 - \eta_T)$ of about 0.8 (about 20 per cent effective).

* Actually, the maxium occurs at the limit $\lambda_T = 1$ (all body), where $(1 - \eta_T)$ is infinite.

(5) ***Case II*** ($m_W = 0$, $m_T = \infty$) ***with Line Vortex***

For $m_T = \infty$, the interference lift is easily obtained by a "strip theory" calculation over the tail plan form and the adjacent body carries no lift. Then, integrating over the tail area S_T,

$$\frac{L_I}{q} = \frac{4}{\beta}\int_{S_T}\int \alpha_I \, dS \tag{10a}$$

where α_I is equal to the inverse tangent of the ratio of the upwash due to the line vortices in the plane of the tail to the free-stream velocity W; for small angles,

$$\alpha_I = \left(\frac{\Gamma}{W}\right)\frac{x_0}{\pi}\left(\frac{1}{x^2 - x_0^2} - \frac{a^2}{x_0^2x^2 - a^4}\right) \tag{10b}$$

and

$$\frac{L_I}{q} = \frac{4a^2}{\pi m_T}\left(\frac{\Gamma}{W}\right)\left\{\frac{1}{\lambda_T}\ln\left|\frac{(\lambda_T - \lambda_0)(1 + \lambda_0\lambda_T)}{(\lambda_T + \lambda_0)(1 - \lambda_0\lambda_T)}\right| - \frac{1}{\lambda_0}\ln\left|\frac{(\lambda_T^2 - \lambda_0^2)}{\lambda_T^2(1 - \lambda_0)^2}\right| + \lambda_0\ln\left|\frac{(1 - \lambda_0^2\lambda_T^2)}{\lambda_T^2(1 - \lambda_0^2)}\right|\right\} \tag{10c}$$

For the calculation of the lift ratios, the wing lift L_W is given by Eq. (9d) and the tail lift with no interference L_T by reference 3,

$$\frac{L_T}{q\alpha} = \frac{4a^2}{m_T}\left[\left(\frac{1 - \lambda_T^2}{\lambda_T^2}\right) + 2\ln\lambda_T\right] \tag{11}$$

As pointed out in Table 2, the nonzero lift ratios as $m_T \to \infty$ are $(1 - \eta_T)$ and $(1 - \eta_W)/L_T$ for this case. A comparison of $(1 - \eta_T)$ for this case and Case I with line vortices is shown in Fig. 11. A marked similarity is seen between these two cases, which describe the bracketing limits of the tail parameter m_T—namely, $m_T = 0$ and $m_T = \infty$. The essential differences are (1) the maximum interference for $m_T = \infty$ occurs for $\lambda_W < \lambda_T < \lambda_0$—i.e., when the tail span is smaller than the wing span, but greater than the vortex span—and (2) $(1 - \eta_T) = 8/\pi^2$, a finite limit at $\lambda_T = 1$ for $m_T = \infty$.

(6) ***Case III*** ($m_W = \infty$, $m_T = 0$) ***and Case IV*** ($m_W = \infty$, $m_T = \infty$)

If the wing-body disturbance for these two cases is represented by line vortices, the nonzero lift ratios (cf. Table 2) are identical to the results for Cases I and II—i.e., the lift ratios $(1 - \eta_W)$ and $(1 - \eta_W)/L_T$ for Case III are identical to those for Case I, and $(1 - \eta_W)/L_T$ for Case IV is the same as that for Case II. These identities are immediately evident, since the two lift ratios are independent of m_W. The representation of the wing disturbance by a vortex sheet has not been carried out for these cases, but the comparison of results for Case I with vortex sheet and with line vortices is indicative of the expected difference between the two representations. Fig. 12 shows the similarity between the two representations of the lift ratio $(1 - \eta_W)$ for Case I.

Applications and Further Studies

From the few experimental results available, the indications are that for $\alpha \to 0$ the interference effects are well described at least qualitatively, and the viscous wake and other nonlinear effects modify the description in a quantitative way. It appears also that, once the geometry of the flow disturbance behind a wing-body (wing not necessarily in the horizontal plane) is sufficiently well understood, then the present analysis can be applied to tail-body configurations where the tail is not in the horizontal plane. Another important problem is that of obtaining the dependence (nonlinear) of the interference effect on the angle of attack α. Some progress in this direction has been made[5] with planar wing-tail configurations having no body. Further work beyond the present analysis for intermediate values of the parameter m_T does not appear warranted at the present time, until further experimental work indicates such a need. A reasonable ap-

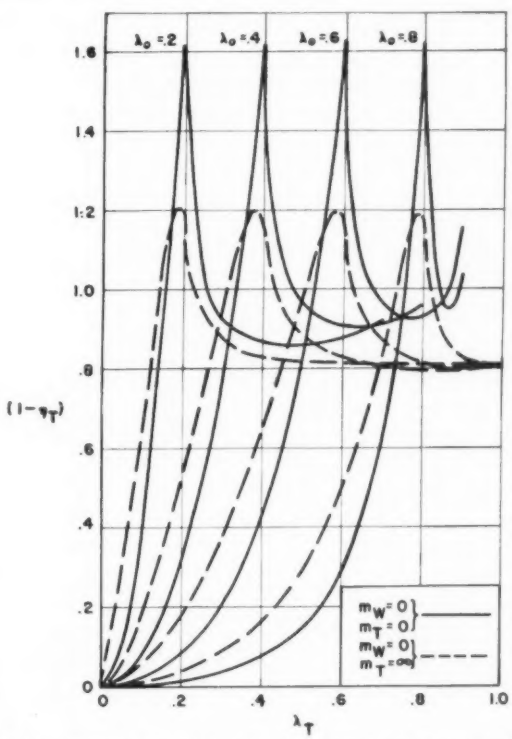

FIG. 11. Comparison of $(1 - \eta_T)$ for Case I and Case II with line vortices.

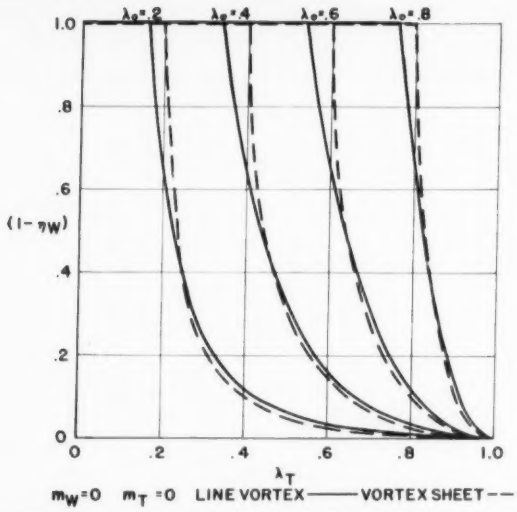

FIG. 12. Comparison of $(1 - \eta_W)$ for Case I with vortex sheet and Case I with line vortices.

proximate analysis for immediate values of m_W is essential and appears possible.

REFERENCES

[1] Spreiter, J. R., and Sacks, A. H., *The Rolling Up of the Trailing Vortex Sheet and Its Effect on the Downwash Behind Wings*, Journal of the Aeronautical Sciences, Vol. 18, No. 1, p. 21, January, 1951.

[2] Lagerstrom, P. A., and Graham, M. E., *Aerodynamic Interference in Supersonic Missiles*, Douglas Report No. SM-13743, Santa Monica, July, 1950.

[3] Morikawa, G. K., *Supersonic Wing-Body Lift*, Journal of the Aeronautical Sciences, Vol. 18, No. 4, p. 217, April, 1951.

[4] Spreiter, J. R., *Aerodynamic Properties of Slender Wing-Body Combinations at Subsonic, Transonic and Supersonic Speeds*, N.A.C.A. T.N. No. 1662, July, 1948.

[5] Graham, M. E., *Some Linearized Computations of Supersonic Wing-Tail Interference*, Douglas Report No. SM-13430, Santa Monica, December 23, 1948.

The Measurement of Downwash and Sidewash Behind a Rectangular Wing at a Mach Number of 1.6

(*Continued from page 332*)

vortex originating at the tip of the wing at angle of attack. The core of this vortex trails out behind the tip and bends slightly inward and downward. The resulting effect on the flow behind the wing is strongest directly behind the wing near the vortex core, and the disturbances show only a slight reduction in intensity as much as 1.5 chord lengths downstream of the wing. It has been demonstrated that these effects can be measured by the use of a conical probe having four static pressure orifices and a total head orifice in the tip.

REFERENCES

[1] Davis, T., *Experimental Investigation of Downwash and Sidewash Behind a Rectangular Wing at a Mach Number of 1.60*, U.A.C. Meteor Report UAC-45, January, 1950.

[2] Smith, C. B., *A Solution for the Downwash Behind a Supersonic Wing*, U.A.C. Meteor Report UAC-28, June, 1948.

[3] Schlichting, H., *Airfoil Theory at Supersonic Speed*, N.A.C.A. T.M. No. 897, June, 1939.

Heat Transfer to Constant-Property Laminar Boundary-Layer Flows with Power-Function Free-Stream Velocity and Wall-Temperature Variation*

SOLOMON LEVY†

University of California at Berkeley

ABSTRACT

Numerical computations have been performed for the boundary-layer form of the energy equation for incompressible flows with power-function variation of free-stream velocity ($u_1 = cx^m$) and of wall temperature ($T_0 = Ax^\gamma$), the pertinent solutions of the momentum equation in this case being those of Hartree. The numerical computations given herein are to some extent a repetition of those given by Schuh and by Chapman and Rubesin, the object of the present computations being the resolution of discrepancies appearing in the previous solutions and an extension of their range. IBM machine calculations were employed in the finite difference calculation presently utilized, the results thereof covering a range of wall-temperature function exponents γ from -2.5 to 4.0 and of Prandtl Numbers from 0.70 to 20.0 for four values of m(4, 1, 0, -0.0904). The accuracy of the numerical computations is examined in detail, and the accuracy of the computed functions at the wall, which determine the heat-transfer rate, is estimated to be within 2 per cent.

Examination of the results reveals that the results of Schuh for the flat plate are in error. For the range of the calculations, it was found that the local heat-transfer coefficient can, with the exception of large negative γ values, be expressed within ± 5 per cent as

$$(hx/k)/\sqrt{u_1 x/\nu} = B(m, \gamma)\sigma^\gamma$$

where the exponent λ of the Prandtl Number σ varies from 0.254 to 0.367 for $-0.0904 < m < 4$ and where the function $B(m, \gamma)$ can be approximated by the equation

$$B(m, \gamma) = \left(\frac{2\gamma}{m+1} + 1\right)^{0.37 + [0.12\, m/(m+1)]} \times \left[0.57\left(\frac{2m}{m+1} + 0.205\right)^{0.104}\right]$$

NOMENCLATURE

A, C, D	=	constant of proportionality unless otherwise defined
$B(m, \gamma)$	=	function of m and γ
a_n, b_n	=	coefficients defined by Eq. (14)
c_n, d_n	=	coefficients defined by Eq. (17)
C_p	=	specific heat at constant pressure, B.t.u./lb. °F.
e	=	step interval in the finite difference solution
$E_{n-1}^{(1)}$	=	extrapolation error defined by Eq. (24)
$E_{n-1}^{(2)}$	=	extrapolation error defined by Eq. (25)
$f(\eta)$	=	solution to Eq. (7) (Hartree profiles)
k	=	thermal conductivity, B.t.u. ft/hr. ft.² °F.
m	=	the exponent in the statement $u_1 = Cx^m$
N	=	total number of steps in the finite difference solution
p	=	the pressure in the boundary layer, lbs. per sq.ft.
q_0	=	the local heat rate, B.t.u./hr. ft.²
Q	=	the total heat rate, B.t.u./hr. ft.²
R	=	extrapolation error defined by Eq. (26)
r	=	the exponent controlling the heat rate at the surface
S	=	rounding-off error defined by Eq. (28)
T	=	temperature in boundary layer, °F.
T_1	=	temperature at the edge of the boundary layer, °F.
T_0	=	temperature of the surface, °F.
T_n	=	Rounding-off error defined by Eq. (27)
u	=	velocity component of flow in x direction, ft. per sec.
u_1	=	velocity at the edge of the boundary layer, ft. per sec.
v	=	velocity perpendicular to body surface, ft. per sec
x	=	distance along the body surface, ft.
y	=	distance normal to the body surface, ft.
β	=	velocity distribution parameter, $2m/(m+1)$
γ	=	the exponent controlling the temperature distribution along the surface ($T_0 = Ax^\gamma$)
η	=	independent variable occurring in the Hartree profiles
θ	=	the dimensionless temperature, T/T_0
λ	=	the exponent determining the effect of the Prandtl Number
μ	=	absolute viscosity, lb. sec./ft.²
ν	=	the kinematic viscosity, ft.²/sec.
ρ	=	density of the flowing fluid, lb. sec.²/ft.⁴
σ	=	the Prandtl Number, $\mu c_p/k$ dimensionless
ψ	=	the stream function

Received August 13, 1951.

* This work was carried out at the Boundary-Layer Project at the University of California under the guidance and supervision of Dr. R. A. Seban and Dr. R. M. Drake, Jr., and was sponsored by the Air Material Command under Air force Contract No. 33(038)-12941. Their help is gratefully acknowledged.

† Research Engineer.

INTRODUCTION

THE CALCULATION OF THE HEAT TRANSFER to the laminar boundary layer is of importance in many engineering applications. This type of flow occurs in the aerodynamic heating of bodies in flight, in the cooling of gas-turbine blades, along airfoil surfaces, and along rocket motor nozzles. In such instances, the character of the variation of the wall temperature often has an important influence upon the rate of heat trans-

fer, and, in consequence, solutions of the momentum and energy equation leading to an accounting of the effect of variable wall temperature are of significance. In certain circumstances, such as the stagnation point region, the solutions can be used directly for design calculations; for others in which an arbitrary variation of free-stream velocity and wall temperature or heat rate occur, approximate methods based on these solutions have been proposed.[1]

All boundary-layer solutions in which variation of the wall temperature can be accounted for deal with incompressible constant property flows with free-stream velocity a power function of the distance from the stagnation point. These are the "wedge flows" ($u_1 = cx^m$) for which the solution of the momentum equation has been given by Hartree.[2] Exact solutions of the corresponding energy equation are only possible for the case in which the wall temperature is a power function of distance from the stagnation point ($T_0 = Ax^7$).

Solutions of the energy equation as given in this report have already been presented by Schuh[3] and by Chapman and Rubesin.[4] Schuh considered the flat-plate flow and two wedge flows ($m = 1/2$, $m = 1$) and obtained his results by the method of successive approximation. Chapman and Rubesin considered flat-plate flow only but considered variation of properties to the extent that $\mu\rho$ = const., under which circumstances the solutions apply for the imcompressible case, as well as for the case of compressible flow. This solution was obtained by use of the Runge-Kutta integration method. Certain discrepancies exist within Schuh's results and between the results of Schuh and Chapman and Rubesin. The present solution was undertaken to resolve these discrepancies; to investigate further the effect of the Prandtl Number for this case, since the previously available solutions considered only Prandtl Numbers of about 0.70; and to present solutions for two additional "wedge flows" ($m = 4$ and $m = -0.0904$).

Analysis

Derivation of Equations

In the laminar boundary layer of a body in flow at high Reynolds Number, the velocity increases from zero at the wall to the free-stream velocity u_1. The boundary-layer forms of the continuity, momentum, and energy equations for an incompressible constant property two-dimensional flow are

$$(\partial u/\partial x) + (\partial v/\partial y) = 0 \tag{1}$$

$$\rho\left(u\frac{\partial u}{\partial x} + v\frac{\partial u}{\partial y}\right) + \frac{\partial p}{\partial x} = \mu\frac{\partial^2 u}{\partial y^2} \tag{2}$$

$$\rho C_p\left(u\frac{\partial T}{\partial x} + v\frac{\partial T}{\partial y}\right) = k\frac{\partial^2 T}{\partial y^2} \tag{3}$$

where x is measured along the surface of the body and

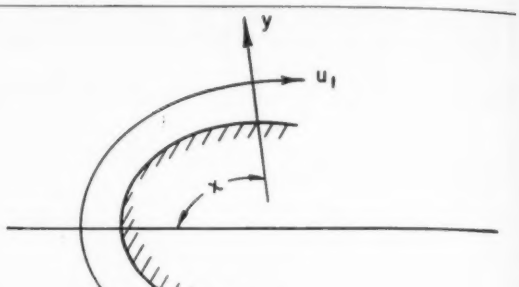

FIG. 1. Flow boundary layer about an arbitrary body.

where the y-axis is taken perpendicular to the surface (Fig. 1).

The dissipation term is omitted from the energy equation, Eq. (3). For use with flows in which frictional heating is significant, the solution of Eq. (3) is to be added to the appropriate adiabatic wall solution to satisfy the prevailing boundary conditions. The temperature T appearing in Eq. (3) represents a temperature difference between the local and free-stream temperature and, in consequence, partially accounts for the term, $u(dp/dx)$, which appears in that equation when the state temperature is the dependent variable.

The boundary conditions are

$$\begin{array}{lll} T = T_0(x) & u = v = 0 & y = 0 \\ T = 0 & u = u_1 & y \to \infty \end{array}$$
$$\text{with } u_1 = cx^m$$

Introduction of the Hartree variables,

$$\eta = \sqrt{[(1+m)/2](u_1/\nu x)}\; y \tag{4}$$

$$\psi = \sqrt{[2/(1+m)]\nu x u_1}\, f(\eta) \tag{5}$$

where ψ is the stream function defined by

$$u = \partial\psi/\partial y \qquad v = -\partial\psi/\partial x \tag{6}$$

yields the following form for Eqs. (2) and (3) through Eq. (1):

$$f'''^{*} + ff'' + \beta(1 - f'^2) = 0 \tag{7}$$

$$\frac{1}{\sigma}\frac{\partial^2 T}{\partial \eta^2} + f\frac{\partial T}{\partial \eta} - \frac{2}{1+m}f'x\frac{\partial T}{\partial x} = 0 \tag{8}$$

where $\beta = 2m/(m+1)$ and $\sigma = \mu C_p/k$ is the Prandtl Number.

Eq. (7) has been solved by Hartree for several values of β, and these solutions are employed for the solution of the energy equation. This equation is changed to an ordinary differential equation by introducing the temperature function $\theta = T/T_0$, where $\theta = \theta(\eta)$ and $T_0 = Ax^7$. Thus,

* The primes indicate the order of differentiation with respect to η.

$$\frac{d^2\theta}{d\eta^2} + f\sigma\frac{d\theta}{d\eta} - \sigma(2-\beta)\gamma f'\theta = 0 \qquad (9)$$

The boundary conditions are

$$\theta = 1 \qquad \eta = 0$$
$$\theta = 0 \qquad \eta \to \infty$$

Before the general method of solution of Eq. (9) is considered, a few particular cases that yield rather simple numerical solutions are discussed.

Eq. (9) has been solved by Pohlhausen[5] and by Eckert[6] for the case of an isothermal wall, so that $\gamma = 0$ and the solution can be obtained by quadratures. When γ is not zero, numerical solution of Eq. (9) is necessary except for the particular case in which the factor $(2-\beta)\gamma$ is equal to -1. In this case the equation is exact and solution by quadratures is possible. For this special case the solution is

$$\theta = e^{-\int_0^\eta \sigma f\, d\eta} \qquad (10)$$

For this case $(d\theta/d\eta)_{\eta=0} = 0$, and the temperature gradient at the wall, which is

$$\left(\frac{\partial T}{\partial y}\right)_{y=0} = Ax^\gamma \left(\frac{d\theta}{d\eta}\right)_{\eta=0} \frac{1}{\sqrt{2-\beta}}\sqrt{\frac{u_1}{\nu x}}$$

$$\left(\frac{\partial T}{\partial y}\right)_{y=0} = A\left(\frac{d\theta}{d\eta}\right)_{\eta=0} \frac{x^{-1}}{\sqrt{\nu(2-\beta)}}$$

is seen to be zero for all values except the indeterminate point at $x = 0$. At that point the temperature of the fluid immediately adjacent to the wall is infinite, and the heat introduced impulsively at this point can be determined from the heat flow in the boundary layer at any point x. This is

$$Q = \rho C_p u_1 T_0 \int_0^\infty \frac{T}{T_0}\frac{u}{u_1}\,dy = A\rho C_p \sqrt{\nu C(2-\beta)} \int_0^\infty \theta f'\,d\eta \qquad (11)$$

It can be shown that for $\gamma > -1/(2-\beta)$ the heat flow at the wall is always into the boundary layer, while for $\gamma < -1/2-\beta$ the heat flow is into the wall despite the fact that the wall temperature always exceeds the free-stream temperature.

For values of γ other than noted above, numerical solution of Eq. (9) is necessary, and this has been carried out by the method of differences. Reduction of that equation to finite difference form, with the increments in θ being distant e apart and subscript n denoting the number of the increment beginning with zero at the plate, produces the equation

$$\frac{\theta_n - 2\theta_{n-1} + \theta_{n-2}}{e^2} + \sigma f_{n-1}\frac{\theta_n - \theta_{n-1}}{e} - \gamma\sigma(2-\beta)f_{n-1}'\theta_{n-1} = 0 \qquad (12)$$

This yields, for the temperature at increment n,

$$\theta_n = \frac{2 + \sigma e f_{n-1} + \sigma\gamma e^2(2-\beta)f_{n-1}'}{1+\sigma e f_{n-1}}\theta_{n-1} - \frac{1}{1+\sigma e f_{n-1}}\theta_{n-2} \qquad (13)$$

If the factors of Eq. (13) are defined as

$$\left.\begin{aligned} a_{n-1} &= \frac{2 + \sigma e f_{n-1} + \sigma\gamma e^2(2-\beta)f_{n-1}'}{1+\sigma e f_{n-1}} \\ b_{n-1} &= 1/(1+\sigma e f_{n-1}) \end{aligned}\right\} \qquad (14)$$

then Eq. (13) acquires the form

$$\theta_n = a_{n-1}\theta_{n-1} - b_{n-1}\theta_{n-2} \qquad (15)$$

In virtue of the boundary conditions at the surface $\theta_0 = 1$,

$$\theta_2 = a_1\theta_1 - b_1$$
$$\theta_3 = a_2\theta_2 - b_2\theta_1, \text{ etc.}$$

so that all θ_n values are expressible in terms of θ_1. This may be expressed generally as

$$\theta_n = c_{n-1}\theta_1 - d_{n-1} \quad (n \geq 2) \qquad (16)$$

where

$$c_{n-1} = a_{n-1}c_{n-2} - b_{n-1}c_{n-3}$$
$$d_{n-1} = a_{n-1}d_{n-2} - b_{n-1}d_{n-3}$$

where

$$\begin{aligned} c_1 &= a_1 & d_1 &= b_1 \\ c_0 &= 1 & d_0 &= 0 \end{aligned} \qquad (17)$$

The calculations leading to θ_n for large n were accomplished on an electronic IBM computing machine, in which six decimals were carried in the machine and the results were rounded off to five decimals. The increment $e = \Delta\eta$ was taken in most instances as 0.1. In virtue of the boundary conditions, θ_n becomes zero for large n (i.e., $\eta \to \infty$). In this calculation, if the value of θ_1 was unaffected within the sixth decimal place by evaluation from Eq. (16) with $\theta_n = 0$ for two positions n and $n-1$, the number of increments was deemed sufficiently great. With this value of θ_1, the entire temperature field could be determined from Eq. (16).

The temperature gradient at the wall gives the heat flux and as such is the most important result. This is

$$(d\theta/d\eta)_{n=0} = -(1-\theta_1)/e \qquad (18)$$

and can be evaluated from the known value θ_1.

Appendix (A) contains a discussion of the accuracy of the method and the probable precision of the results.

Results

Calculations have been carried out for a sufficient number of cases to describe the combined effect on the heat transfer of free-stream velocity and wall-temperature variation and of changes in the Prandtl Number of the fluid. These cases are indicated in the following tabulation:

TABLE 1
Temperature Gradients at the Wall for Flat-Plate Flow ($\beta = 0$). Variable Wall Temperature

	Calculated				Schuh	Rubesin
γ/σ	0.70	2.0	10	20	0.70	0.715
−0.50	0	0	0	0	...	...
−0.25	...	−0.3789	−0.6257	−0.7668	...	...
0.00	−0.4065	−0.5822	−0.9863	−1.230	−0.414	−0.418
0.25	−0.4989	−0.7130	−1.210	−1.513	...	...
0.50	−0.5690	−0.8112	−1.377	−1.721	...	...
1.00	−0.6746	−0.9593	−1.625	−2.024	−0.576	−0.691
2.00	−0.8218	−1.165	−1.965	−2.445	...	−0.845
3.00	−0.9296	−1.316	−2.211	−2.741	...	−0.967
4.00	−1.017	−1.437	−2.406	−2.974	−0.828	−1.053

TABLE 2
Temperature Gradients at the Wall for Stagnation Flow ($\beta = 1.0$). Variable Wall Temperature

	Calculated				Schuh
γ/σ	0.7	1	5	10	0.7
−1.0	0	0	0	0	...
−0.75	−0.1755	−0.2001	...	−0.4062	...
−0.50	...	...	...	−0.8094	−0.318
−0.25	−0.4093	−0.4708	...	−1.081	...
0	−0.4879	−0.5603	−1.011	−1.286	−0.496
0.25	−0.5535	−0.6345	−1.141	−1.451	...
0.50	−0.6094	−0.6979	−1.251	−1.590	...
1.00	−0.7033	−0.8116	−1.432	−1.818	−0.707
2.00	−0.8461	−0.9647	...	−2.159	−0.854
2.40	...	...	−1.795	...	...
3.00	−0.9567	−1.089	−1.914	−2.418	...
4.00	−1.048	−1.192	−2.086	−2.630	−1.050

TABLE 3
Temperature Gradient at the Wall for Wedge Flow ($\beta = 1.6$) Variable Wall Temperature

	Calculated			
γ/σ	0.7	1.0	5.0	10.0
−2.50	0.0000	0.0000	0.0000	0.0000
−1.50	−0.2687	−0.3101	−0.5587	−0.7005
−0.50	−0.4413	−0.5085	−0.9303	−1.186
0.00	−0.5062	−0.5828	−1.064	−1.357
0.25	−0.5353	−0.6161	−1.122	−1.432
0.50	−0.5626	−0.6468	−1.176	−1.501
1.00	−0.6120	−0.7031	−1.275	−1.626
2.00	−0.6975	−0.7995	−1.442	−1.836
3.00	−0.7692	−0.8808	−1.581	−2.010
4.00	−0.8315	−0.9512	−1.701	−2.159

TABLE 4
Temperature Gradients at the Wall for Separation Flow ($\beta = -0.199$). Variable Wall Temperature

	Calculated			
γ/σ	0.7	1.0	5.0	10.0
−1/2.199	0.0000	0.0000	0.0000	0.0000
−0.25	−0.1955	−0.2168	−0.3290	−0.3894
0.00	−0.2930	−0.3227	−0.4884	−0.5806
0.25	−0.3476	−0.3820	−0.5760	−0.6848
0.50	−0.3861	−0.4237	−0.6375	−0.7581
1.00	−0.4412	−0.4835	−0.7257	−0.8629
2.00	−0.5134	−0.5622	−0.8424	−1.002
3.00	−0.5641	−0.6174	−0.9245	−1.099
4.00	−0.6041	−0.6608	−0.9890	−1.176

$$\begin{cases}\beta = 0 \text{ (flat-plate flow)}\\ \gamma = -0.5 \text{ to } 4.00\\ \sigma = 0.70, 2, 10, 20\end{cases}$$

$$\begin{cases}\beta = 1 \text{ (stagnation flow)}\\ \gamma = -1 \text{ to } 4\\ \sigma = 0.70, 1, 5, 10\end{cases}$$

$$\begin{cases}\beta = 1.6\\ \gamma = -2.5 \text{ to } 4\\ \sigma = 0.70, 1, 5, 10\end{cases}$$

$$\begin{cases}\beta = -0.199 \text{ (separation flow)}\\ \gamma = -0.455 \text{ to } 4\\ \sigma = 0.70, 1, 5, 10\end{cases}$$

The large number of cases considered prohibits complete presentation of the results for all. The most important result, the gradient of the temperature function at the wall, is presented for all cases in Tables 1, 2, 3, and 4. The knowledge of this magnitude enables the calculation of the heat rate at the wall as

$$q_0 = -kT_0 \left(\frac{d\theta}{d\eta}\right)_{\eta=0} \frac{1}{\sqrt{2-\beta}} \sqrt{\frac{u_1}{\nu x}} \qquad (19)$$

if the wall temperature $T_0 = Ax^\gamma$ is given. Should the wall heat rate, $q_0 = Dx^r$, be given instead, the wall temperature T_0 is determined by Eq. (19), with

$$\gamma = r + [(1-\beta)/(2-\beta)]$$

Distribution of the temperature within the boundary layer is illustrated by Figs. 4, 5, and 6, covering the following cases:

$$\begin{cases}\sigma = 0.70\\ \beta = 1.6, 1.0, 0, -0.199\end{cases}$$

$$\begin{cases}\beta = 1\\ \sigma = 1, 5, 10\end{cases}$$

All values given for the cases $\gamma = -1/(2-\beta)$ were obtained from Eq. (10) rather than from the finite difference calculation.

DISCUSSION

Examination of the results for the gradient of the temperature function at the wall reveals a check with the results of Chapman and Rubesin which is within the accuracy of the present calculations. There is also agreement with the results of Schuh for the stagnation flow, but his results for the flat-plate case are evidently in error.

The effect of the parameter β on the wall-temperature gradient as revealed in Fig. 2 is small in the region $0 < \beta < 1$ but becomes significant at higher or lower values of β. For interpolation over the entire range of values,

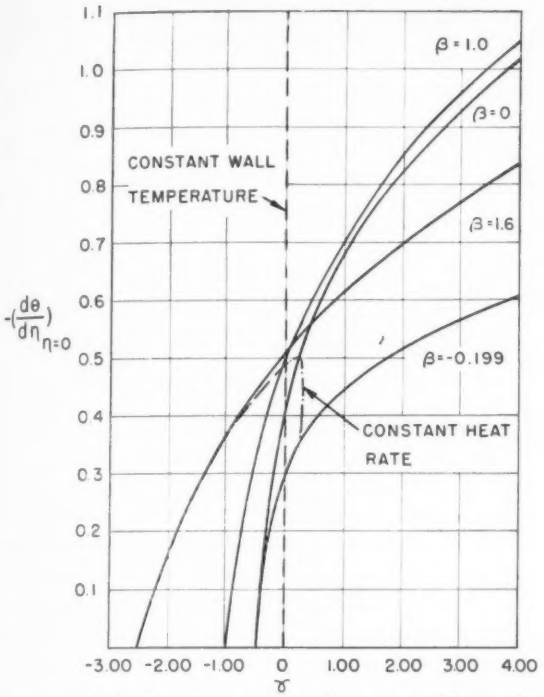

FIG. 2. Calculated temperature gradient at wall for wedge flow with variable wall temperature. Prandtl Number = 0.70.

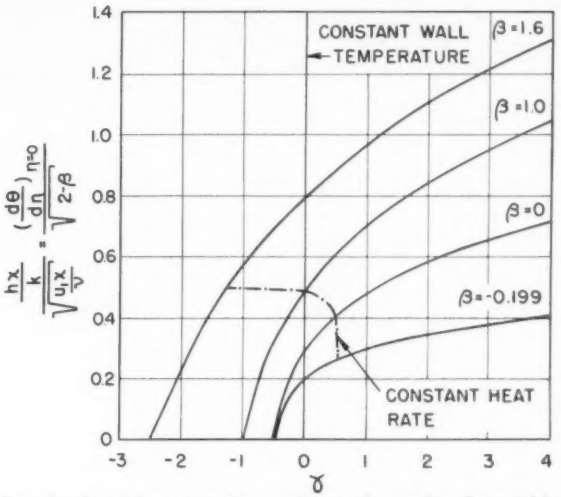

FIG. 3. Local heat-transfer coefficients for wedge flows with variable wall temperature. Prandtl Number = 0.70.

the representation of the quantity $(hx/k)/\sqrt{u_1 x/\nu}$ is more convenient, as indicated by Fig. 3. Figs. 2 and 3 contain a curve indicating the values of β and γ, which in combination produce a wall heat rate invariable in the direction of flow.

The effect of the Prandtl Number can be simply appraised by cross-plotting results for given β values as exemplified by the results for $\beta = 1$ of Fig. 7, which are represented on Fig. 8 within a narrow range by the use of a suitable factor, $\sigma^{0.355}$. Treatment of all the available results in this way yields the following factors:

β	1.6	1.0	0	−0.199
λ	0.367	0.355	0.327	0.254

Thus,

$$\frac{hx/k}{\sqrt{u_1 x/\nu}} = B(m, \gamma)\sigma^{\lambda}$$

where $B\sigma^{\lambda}$ is given by Fig. 3 for $\sigma = 0.70$.

The exponent of the Prandtl Number as obtained can be approximated on theoretical grounds. Any analysis that postulates a linear velocity distribution within the boundary layer, such as the analysis of Bond,[7] yields a factor $\sigma^{1/3}$. Analysis presuming a constant velocity within the boundary layer yields a value of $\sigma^{1/2}$ typical of all "heat conduction" solutions. Tifford,[8] approximating the velocity distribution for the separation flow by the parabola $u/u_1 = 0.10\eta^2$, obtained a factor $\sigma^{1/4}$. Approximations of this type become more valid as the

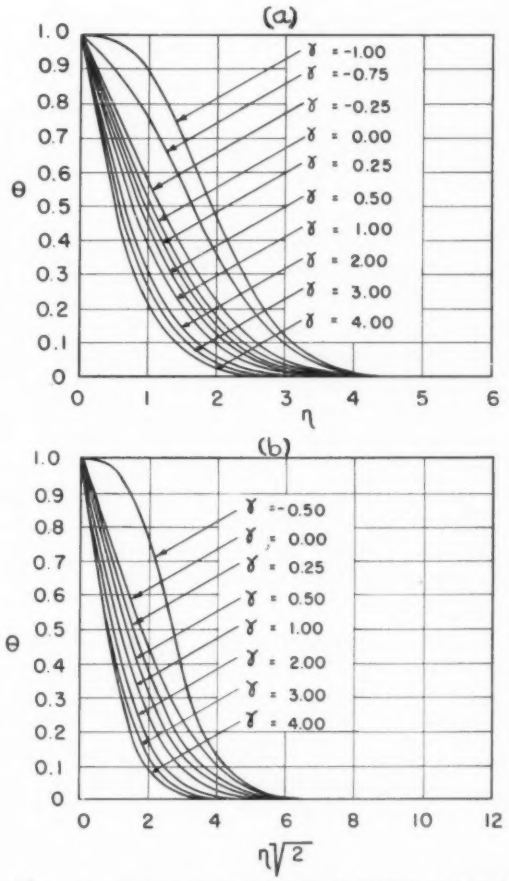

FIG. 4. (a) Temperature distribution for stagnation flow with variable surface temperature. Prandtl number = 0.70. (b) Temperature distribution for flat-plate flow with variable wall temperature. Prandtl Number = 0.70.

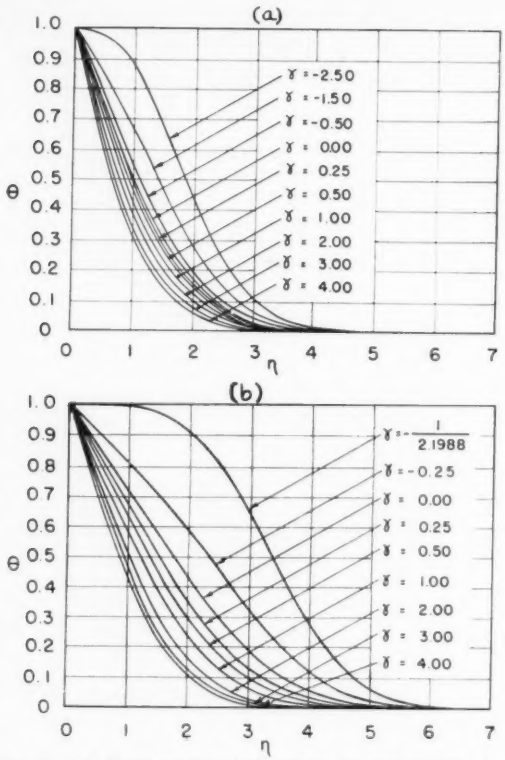

FIG. 5. (a) Temperature distribution for wedge flow ($\beta = 1.60$) with variable surface temperature. Prandtl Number = 0.70. (b) Temperature distribution for separation flow ($\beta = -0.1988$) with variable surface temperature. Prandtl Number = 0.70.

thickness of the thermal boundary layer is reduced, and this effect is produced by increasing the value of σ and also, as examination of the present results reveals in Figs. 4 and 5, by increasing the value of γ. Because of this effect, the exponents λ given for the present results are approximations relevant to the range of σ and γ considered in the calculations. They do, however, follow the trends predicted, being near $^1/_4$ for the separation flow and near $^1/_3$ in the range $0 < \beta < 1$ where the approximation of a linear velocity variation is justifiable and the value does increase as β increases beyond unity, where the velocity distribution within the boundary layer becomes increasingly more uniform.

Further investigation of the results reveals that, within the range of the calculations, the function $B(m, \gamma)$ can be approximated within ± 5 per cent by the equation

$$B(m, \gamma) = 0.57 \left(\frac{2m}{m+1} + 0.205 \right)^{0.104} \times \left(\frac{2\gamma}{m+1} + 1 \right)^{0.37 + [0.12m/(m+1)]}$$

This expression, however, fails at large negative γ values.

APPENDIX (A)—ACCURACY OF THE NUMERICAL SOLUTION

Numerical Solution

The use of punched-card machines for solving linear differential equations by means of a difference method was illustrated by Feinstein and Schwarzschild.[9] Proceeding in an identical manner, the constants a_{n-1}, b_{n-1}, c_{n-1}, and d_{n-1} were calculated on the electronic computer. The value of θ_1 was obtained by setting $\theta_{61} = 0$, thus giving, for $\beta = 0$ and $\gamma = 0$,

$$\theta_1 = 0.9296657$$

If one takes $\theta_{60} = 0$, the corresponding θ_1 is

$$\theta_1 = 0.9296657$$

Both values are seen to agree within the sixth decimal, which confirms the convergence of the temperature profile.

The use of the difference method for solving differential equations has been discussed in references 10 and 11. The size of the interval and the total number of steps N must be chosen to ensure negligible errors in

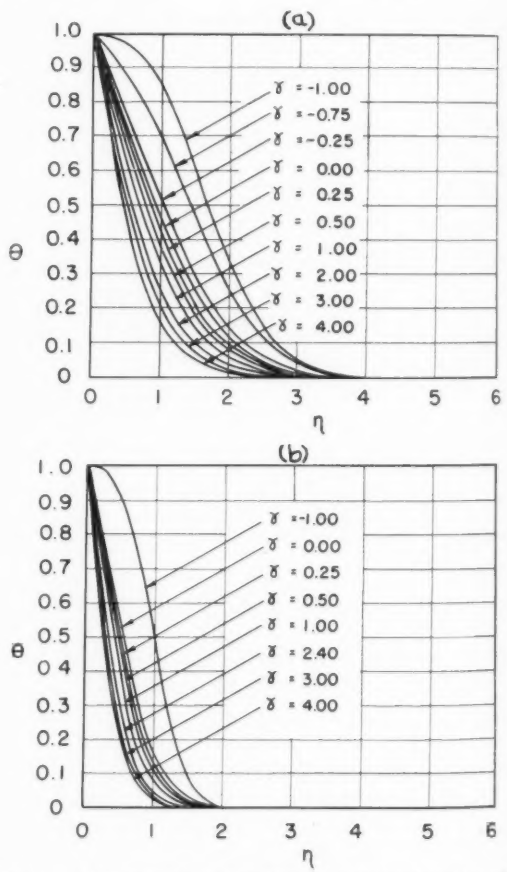

FIG. 6. (a) Temperature distribution for stagnation flow with variable surface temperature. Prandtl Number = 1.0. (b) Temperature distribution for stagnation flow with variable surface temperature. Prandtl Number = 5.0.

the final results. In this analysis the interval e was taken as 0.10 mainly because the Hartree functions are tabulated for each 0.10 value of the independent variable η. The interval was changed in one particular case from 0.10 to 0.05, and results of the same order of magnitude were obtained. This smaller interval, however, meant successive interpolations of the functions f and f'. The resulting error was considered too large and the interval e was taken as 0.10 for the remainder of the calculations.

Accuracy of the Solution

An absolute check of the accuracy of the calculated results can be obtained by means of an iterative method. A more accurate solution can be evaluated by taking the machine solution as the first approximation in the integral form of the energy equation. A more accurate temperature distribution thus follows. Such a calculation, however, was not accomplished. The possible error in the machine solution was estimated instead.

As pointed out by Feinstein and Schwarzschild, the total error made in one step consists of two parts—the error of the extrapolation formula and the rounding off error.

The energy equation, Eq. (9), for $\eta = (n-1)e$ can be written

$$\theta_{n-1}'' = \sigma(2-\beta)f_{n-1}'\theta_{n-1} - f\sigma\theta_{n-1}' \qquad (20)$$

By developing θ_n and θ_{n-2} into a Taylor series, one gets

$$\theta_n = \theta_{n-1} + e\theta_{n-1}' + \frac{e^2}{2!}\theta_{n-1}'' + \frac{e^3}{3!}\theta_{n-1}''' + \ldots \qquad (21)$$

$$\theta_{n-2} = \theta_{n-1} - e\theta_{n-1}' + \frac{e^2}{2!}\theta_{n-1}'' - \frac{e^3}{3!}\theta_{n-1}''' + \ldots \qquad (22)$$

Eliminating θ_{n-1}' and θ_{n-1}'' between Eqs. (20), (21), and (22), there results

$$\theta_n = a_{n-1}\theta_{n-1} - b_{n-1}\theta_{n-2} + \frac{f\sigma e^3}{2}\theta_{n-1}'' + \frac{f\sigma e^4}{6}\theta_{n-1}''' + \ldots \qquad (23)$$

where the fifth and higher values of the step value e have been neglected and where a_{n-1} and b_{n-1} are given by Eq. (14).

The dominant error in Eq. (23) is

$$E_{n-1}^{(1)} = (f\sigma e^3/2)\theta_{n-1}'' \qquad (24)$$

The next effective error is

$$E_{n-2}^{(2)} = (f\sigma e^4/6)\theta_{n-1}''' \qquad (25)$$

Every E_{n-1} produces errors in the following θ's, increasing roughly linearly with the number of subsequent steps. Hence, the error in the final θ produced by one E_{n-1} is $(N-n+1)E_{n-1}$, where N is the total number of steps.

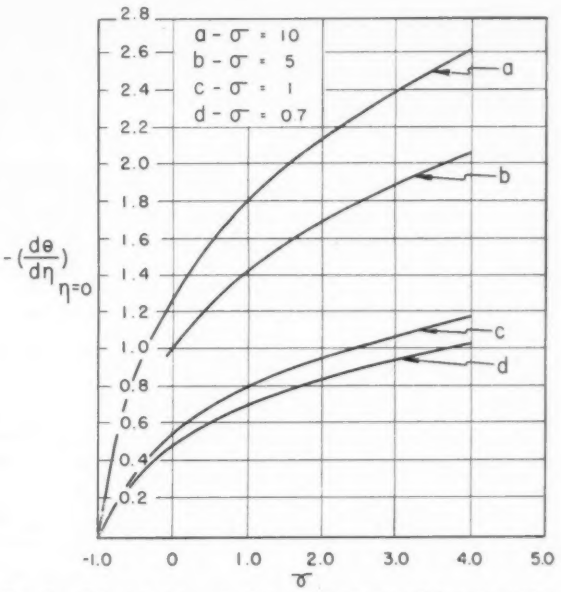

FIG. 7. Calculated temperature gradient at wall for stagnation flow ($\beta = 1$). Variable wall temperature.

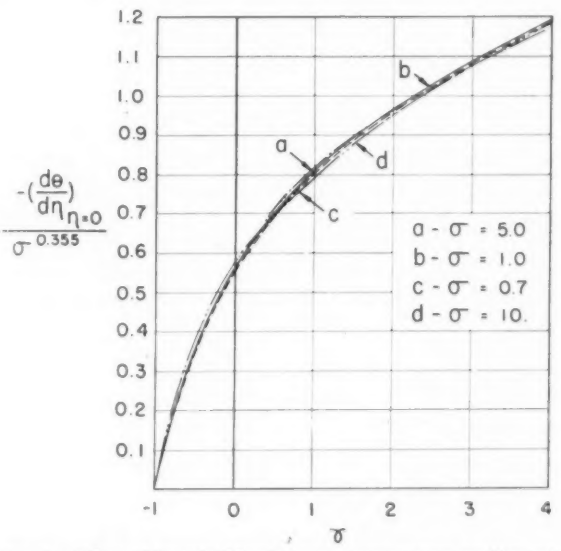

FIG. 8. Effect of Prandtl Number upon temperature gradient at wall for stagnation flow with variable wall temperature.

If one sets $E_{n-1} = (E_{n-1})_{\text{average}}$ these errors can be summed up by the square root of the sum of their squares. The summation over n gives, for the error in the final θ_{61} produced by all the E_{n-1}'s,

$$R = (E_{n-1})_{\text{average}}\,(N^{3/2}/3^{1/2}) \qquad (26)$$

The value of R was estimated for $\beta = 0$ and $\gamma = 0$. It was thus found that R is approximately equal to 0.011. This value was obtained by putting $N = 61$.

The temperature gradient at the wall, however, can easily be determined by stopping at $N = 50$. The extrapolating error in $(d\theta/d\eta)_{\eta=0}$ is thus of the order of 0.0095 or about 2 per cent.

The rounding-off error of θ_n is produced by the errors of a_{n-1}, b_{n-1}, θ_{n-1}, and θ_{n-2} appearing in Eq. (15). Since the calculations were carried to six decimals, each of these four terms has a rounding-off error of $(1/2) \times 10^{-6}$. The corresponding rounding-off error of θ_n becomes

$$T_n = (a_{n-1} + b_{n-1} + \theta_{n-1} + \theta_{n-2})(1/2)10^{-6} \quad (27)$$

Using $a_{n-1} \approx 2$, $b_{n-1} \approx 1$, $\theta_{n-1} \approx 1$, $\theta_{n-2} \approx 1$, one gets

$$T_n = 2.5 \times 10^{-6}$$

Proceeding in a manner similar to the one used for the extrapolating error, the final error in θ_{61} produced by all the rounding-off is

$$S = T_n(N^3/3)^{1/2} \quad (28)$$

For $\beta = 0$ and $\gamma = 0$, S is approximately equal to 7×10^{-4}. Thus the total error in θ_{61} is 0.0117, and the error in $(d\theta/d\eta)_{\eta=0}$ is about 0.010. This last estimate checks the discrepancy noted in $(d\theta/d\eta)_{\eta=0}$ for $\beta = 0$ and $\gamma = 0$. Indeed, the computed value of -0.488 is 0.008 higher than the value -0.496 derived by Eckert.

It is seen that the extrapolation error is by far the larger one of the two. This extrapolation error increases as N increases or as θ converges slowly to zero. For $\gamma \geq 0$, the error in $(d\theta/d\eta)_{\eta=0}$ must be less than 2 per cent, while for $\gamma < 0$ this error may reach 3 to 4 per cent as θ converges rather slowly for negative values of γ. Higher values of Prandtl Number will tend to decrease the error in the temperature gradient at the wall.

References

[1] Seban, R. A., *Calculation Method for Two-Dimensional Laminar Boundary Layers with Arbitrary Free Stream Velocity Variation and Arbitrary Wall Temperature Variation*, Institute of Engineering Research, Report 12, Series 2, University of California, Berkeley, 1950.

[2] Hartree, D. R., *On an Equation Occurring in Falkner and Skan's Approximate Treatment of the Equation of the Boundary Layer*, Proc. Camb. Phil. Soc., Vol. 33, pp. 223–239, 1937.

[3] Schuh, H., *Laminarer Waermeuebergang in Grenzschichten bei Hohen Geschwindigkeiten*, ZWB Forschungsbericht 2019, "Heat Transfer in Laminar Boundary Layers at High Velocities."

[4] Chapman, D. R., and Rubesin, M. W., *Temperature and Velocity Profiles in the Compressible Laminar Boundary Layer with Arbitrary Distribution of Surface Temperature*, Journal of the Aeronautical Sciences, Vol. 16, No. 9, pp. 547–565, September, 1949.

[5] Pohlhausen, E., *Der Waermeaustausch zwischen festen Koerpen and Flussigkeiten mit kleiner Reibung und Kleiner Waermeleitung*, Z.f.a.N.M., Bd. I, S. 115, 1921.

[6] Eckert, E., *The Computation of the Heat Transfer in the Laminar Boundary Layer of Bodies in Flow*, V.D.I.-Forschungsheft No. 416, Berlin, 1942.

[7] Bond, R., *Heat Transfer to a Laminar Boundary Layer with Non-Uniform Free Stream Velocity and Non-Uniform Wall Temperature*, Institute of Engineering Research, Report 10, Series 2, University of California, Berkeley, 1950.

[8] Tifford, A. N., *Some Prandtl Number Effects on the Transfer of Heat*, Engineering Experiment Station News, The Ohio State University, February, 1950.

[9] Feinstein, L., and Schwarzschild, M., *Automatic Integration of Linear Second Order Differential Equations by Means of Punched Card Machines*, The Review of Scientific Instruments, Vol. 12, No. 8, p. 405, August, 1941.

[10] Boole, G., *Treatise on the Calculus of Finite Differences*, New York, Stechert (1946 reprint of 1872 edition).

[11] Jordon, C., *Calculus of Finite Differences*, New York, Chelsea (1947).

Changes of Address

Since the Post Office Department does not as a rule forward magazines to forwarding addresses, it is important that the Institute be notified of changes in address 30 days in advance of publishing date to ensure receipt of every issue of the JOURNAL and REVIEW.

Notices should be printed legibly and sent directly to:

Institute of the Aeronautical Sciences, Inc.

2 East 64th Street, New York 21, New York

Readers' Forum

BRIEF REPORTS of investigations in the aeronautical sciences and discussions of papers published in the JOURNAL are presented in this special department. The publication will be completed approximately 8 to 10 weeks after receipt of the material. The Editorial Committee does not hold itself responsible for the opinions expressed by the correspondents. Contributions should not exceed 800 words in length.

Extension of "The Dynamic Effects in Rotor Blade Bending"

Robert A. Rogers
Aeroproducts Division, General Motors Corporation, Vandalia, Ohio
January 9, 1952

CONSIDERING THE PAPER by A. H. Flax and L. Goland appearing in the JOURNAL OF THE AERONAUTICAL SCIENCES, December, 1951, it is interesting to extend this analysis to the case of a rotating propeller where the blades may be near resonance with the periodic aerodynamic forcing function caused by the air stream entering the propeller disc at an angle to the direction of thrust. Results are identical to those obtained by Flax and Goland, although the boundary conditions of the problem are different.

The fundamental equation of blade bending may be derived from consideration of Fig. 1, where t_0 represents the blade resultant transverse load per unit length and where the axial centrifugal load is represented by p. The equation is, after differentiating twice with respect to r,

$$\frac{\partial^2}{\partial r^2}\left(EI\frac{d^2y}{dr^2}\right) = t_0 - p\frac{\partial y}{\partial r} + \frac{\partial^2 y}{\partial r^2}\int_r^R p\,dr_1 \qquad (1)$$

where the transverse loading is composed of three parts: t_1, the aerodynamic loading considering a rigid blade; t_2, the loading due to the weight and inertia forces; and t_3, the increment of aerodynamic loading caused by deflection of the blade. For propeller blades, the weight term is negligible in comparison with the aerodynamic and inertia loadings. The increment of aerodynamic loading may easily be derived by consideration of the increment of transverse velocity of the air relative to the blade, ΔV_y, produced by the bending motion of the blade. Considering Fig. 2,

$$U^2 = (r\Omega)^2 + V^2 \qquad (2)$$

$$\Delta\alpha = \Delta V_y/U \qquad (3)$$

where $\Delta\alpha$ is the incremental angle of attack caused by bending deflection of the blade. The increment of aerodynamic loading is

$$t_3 = -a_0 c\rho/2U^2\Delta\alpha \qquad (4)$$

$$= -a_0 c\rho/2U\Delta V_y \qquad (5)$$

Since $\Delta V_y = \partial y/\partial t$, then

$$t_3 = -a_0 c\rho/2U\partial_y/\partial t \qquad (6)$$

Letting

$$-\alpha = -a_0 c\rho/2[(r\Omega)^2 + V^2]^{1/2} \qquad (7)$$

Then

$$t_3 = -\alpha(r)\,\partial y/\partial t \qquad (8)$$

Letting

$$F(r) = \int_r^R p\,dr_1$$

we arrive at the basic equation of blade bending which is the same as Eq. (5) in Flax and Goland's paper.

$$\frac{\partial^2}{\partial r^2}\left(EI\frac{d^2y}{dr^2}\right) - F(r)\frac{\partial^2 y}{\partial r^2} + m\frac{\partial^2 y}{\partial t^2} + p\frac{\partial y}{\partial r} + \alpha\frac{\partial y}{\partial t} = t_1 \qquad (9)$$

They have solved this equation utilizing the boundary conditions of a rotor blade hinged at the root. Considering a propeller blade, the equivalent boundary conditions are

$$\left.\begin{array}{ll} \phi_s = \partial\phi_s/\partial r = 0 & (r = 0) \\ \partial/\partial r[EI(\partial^2\phi_s/\partial r^2)] = 0 & (r = R) \\ \partial^2\phi_s/\partial r^2 = 0 & (r = R) \\ F(r) = 0 & (r = R) \end{array}\right\} \qquad (10)$$

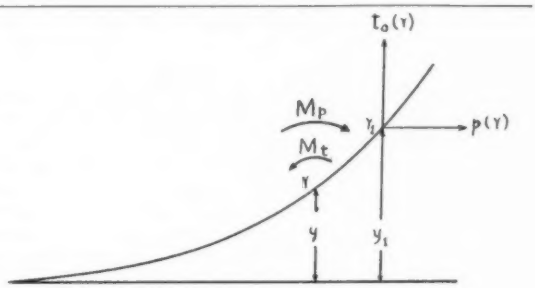

FIG. 1. Loads acting on deflected propeller blade.

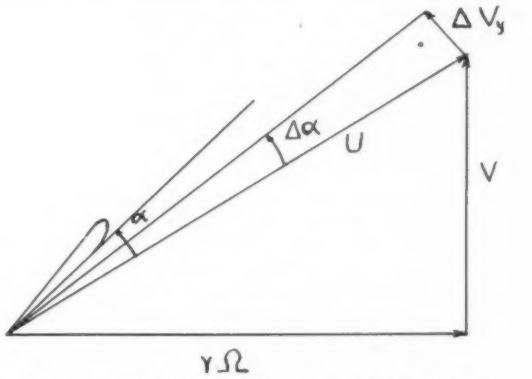

FIG 2. Velocity diagram of oscillating airfoil section.

and these are used in integrating Eq. (18) of Flax and Goland's paper which is

$$q_s \int_0^R \left[\frac{\partial^2}{\partial r^2}\left(EI \frac{\partial^2 \phi_s}{\partial r^2} \right) \phi_s - F(r) \frac{\partial^2 \phi_s}{\partial r^2} \phi_s + p \frac{\partial \phi_s}{\partial r} \phi_s + \phi_s{}^2 (-k^2\Omega^2 m + ik\Omega\alpha) \right] dr = \int_0^R t_k \phi_s l e^{ik\Omega t} \, dr \tag{11}$$

Integrating the first term in Eq. (11) by parts twice, the first two terms again vanish so that

$$\int_0^R \frac{\partial^2}{\partial r^2}\left(EI \frac{\partial^2 \phi_s}{\partial r^2} \right) \phi_s \, dr = \int_0^R EI \left(\frac{\partial^2 \phi_s}{\partial r^2} \right)^2 dr \tag{12}$$

Similarly, the second and third terms of Eq. (11) are combined and integrated by parts so that, considering the boundary conditions of Eq. (10),

$$\int_0^R \left[- F(r) \frac{\partial^2 \phi_s}{\partial r^2} \phi_s + p \frac{\partial \phi_s}{\partial r} \phi_s \right] dr = \int_0^R F(r) \left(\frac{\partial \phi_s}{\partial r} \right)^2 dr \tag{13}$$

Eqs. (12) and (13) are substituted into Eq. (11), and the result is identical to that of Eq. (24) determined by the authors. Thus, for propeller blades, the complete expression for deflection under load t_k is

$$y_k = \sum_{n=1}^{\infty} \left[\frac{\displaystyle\int_0^R t_k \phi_n \, dr}{\displaystyle\int_0^R EI \left(\frac{\partial^2 \phi_n}{\partial r^2} \right)^2 dr + \int_0^R F(r) \left(\frac{\partial^2 \phi_n}{\partial r^2} \right) dr} \right] \frac{e^{i(k\Omega t - \delta_n)} \phi_n(r)}{\sqrt{\left(1 - \dfrac{k^2\Omega^2}{\omega_n{}^2} \right)^2 + \dfrac{k^2\Omega^2 \sigma_n{}^2}{\omega_n{}^4}}} \tag{14}$$

and the static deflection or bending moment may be multiplied by an amplification factor

$$\text{A.F.} = 1/\sqrt{[1 - (k^2\Omega^2/\omega_n{}^2)]^2 + (k^2\Omega^2\sigma_n{}^2/\omega_n{}^4)} \tag{15}$$

to obtain the dynamic deflection or bending moment, respectively.

Attachment of Rotor Blades by Laminated Elastic Straps

Kurt H. Hohenemser
Chief of Aerodynamics, Helicopter Engineering Division, McDonnell Aircraft Corporation, St. Louis
January 23, 1952

THE ATTACHMENT OF A ROTOR BLADE by two laminated elastic straps offset from the blade feathering axis in the plane of rotation was first used in Doblhoff's experimental pressure jet helicopter WN 342 and is also incorporated in the French pressure jet helicopter "Ariel." The straps are a substitute for a flapping hinge and for a thrust bearing otherwise necessary to transfer the centrifugal force of the blade to the hub. In combination with a floating hub the straps are a convenient, simple, and trouble-free means of blade attachment which also allows the vertical blade hinge and its damper to be eliminated.

When designing the strap attachment, care has to be taken to avoid mechanical instability of the chordwise blade oscillations in flight and on the ground, and the spacing, length, and cross section of the straps are powerful parameters for influencing the natural frequency ν_b of the lowest chordwise blade bending mode.

Reference 1 gives a description and analysis of the strap attachment for the French helicopter "Ariel II." The following criterion for avoiding chordwise self-excited mechanical oscillations of rotor blades is used:

$$2 > \omega/\nu_b > 1 \tag{1}$$

where ω is the rotor speed. This criterion was taken from reference 2, but it is, unfortunately, in error. Reference 2 is based on reference 3, which gives a correct analysis of the problems of self-excited chordwise rotor-blade oscillations including blade damping using the frequency response method. The results of reference 3 are in agreement with those of reference 4. In reference 2, however, an erroneous transition was made from the case with finite blade damping to the limiting case of infinitely small blade damping. Actually, the center of the instability range in the case of undamped chordwise blade oscillations is given by the relation

$$\nu_p + \nu_b = \omega$$

where ν_p is the frequency of a horizontal pylon mode. In flight, this frequency is identical with the so-called pendulum frequency of the rotor craft and is quite low. Therefore the center of mechanical instability is avoided if

$$\omega_{max.} < \nu_b \tag{2}$$

for the highest rotor speed obtainable in flight. This is certainly a safe design criterion for the strap attachment of rotor blades. In case of the French helicopter "Ariel II," this criterion is obviously not fulfilled. In this case the landing gear has to be sufficiently stiff, so that on the ground

$$\omega_{max.} < \nu_b + \nu_L \tag{3}$$

where ν_L is the lowest frequency of a landing gear mode with a horizontal component at the location of the rotor. In the air the rotor speed must never drop below

$$\omega_{min.} > \nu_p + \nu_b \tag{4}$$

where ν_p is the frequency of the pendulum mode, otherwise mechanical instability of the chordwise blade mode will occur in flight. When designing the strap attachment the erroneous criterion (1) must be replaced by the criterion (2) or by the criteria (3) and (4) for the center of the instability range, and an adequate margin of $\omega_{max.}$ and $\omega_{min.}$ must be kept with respect to this center in order to avoid mechanical instability.

REFERENCES

[1] Laufer, Th., *Attache par Faisceaux de Lames Elastiques des Pales D'Appareils a Voilures Tournantes*, presented at the Congrès Internationale de Giraviation, Paris, June, 1951. (Technique de Science Aeronautique, 1951.)

[2] Hohenemser, K., *Theory of Oscillations of Blades in the Plane of Rotation*, A.M.C. Translation No. F-TS-1005-RE, 1946.

[3] Hohenemser, K., *Zur Dynamik von umlaufenden, gelenkig an die Nabe angeschlossenen und in der Umlaufebene schwingenden Staeben*, Ingenieur Archiv, Vol. 14, February, 1943.

[4] Coleman, P., *Theory of Self-Excited Mechanical Oscillations of Hinged Rotor Blades*, A.R.R. No. 3G29, July, 1943.

The Shock Strength in a Two-Dimensional Nonsteady Flow

Lu Ting
Daniel Guggenheim School of Aeronautics, New York University
December 28, 1951

ASSUME THAT A SMALL DISTURBANCE starts at origin ($r = 0$); when $t = 0$, the linearized theory will give a good approximation to the flow in and outside the Mach cone, $r = C_0 t$ (sonic velocity of the undisturbed fluid), with apex at $r = 0$, $t = 0$. In order to obtain an approximate solution uniformly valid on the Mach cone, Lighthill's technique[1, 2] is applied.

Expanding both the independent variable $r - C_0 t$, and the velocity potential φ into power series of a small parameter ϵ,

$$r - C_0 t = R + \epsilon r^{(1)}(r, \theta) + \epsilon^2 r^{(2)}(r, \theta) + \dots \quad (1)$$

$$\varphi(r, \theta, t) = \epsilon \varphi^{(1)}(r, \theta, R) + \epsilon^2 \varphi^{(2)}(r, \theta, R) + \dots \quad (2)$$

and substituting them into the basic equations (in polar coordinates) for unsteady two-dimensional potential motion, we have

$$\left(\frac{\partial^2}{\partial r^2} + \frac{\partial}{r\partial r} + \frac{\partial^2}{r^2\partial\theta^2} + 2\frac{\partial^2}{\partial r \partial R} + \frac{\partial}{r\partial R}\right)(\epsilon\varphi^{(1)} + \epsilon^2\varphi^{(2)} + \epsilon^3\varphi^{(3)} + \dots) = \epsilon^2\{[2r_r^{(1)} - (\gamma+1)\varphi_R^{(1)}/C_0 - 2\varphi_r^{(1)}/C_0] \times (\varphi_{RR}^{(1)} + \epsilon\varphi_{RR}^{(2)} + \dots) + \epsilon[2r_r^{(2)} - (\gamma+1)\varphi_R^{(2)}/C_0 - 2\varphi_r^{(2)}/C_0 + \text{a quadratic form in } \varphi_r^{(1)}, \varphi_\theta^{(1)}, r_r^{(1)}, \text{ and } r_\theta^{(1)}]\varphi_{RR}^{(2)} + o(\epsilon^2) + \text{additional terms with at most first derivative with respect to } R\}. \quad (3)$$

The first order equation is a simple wave equation for $\varphi^{(1)}$, which is exactly the same as the linearized solution of $\varphi(t, r, \theta)$ with t replaced by $(r - R)/C_0$. Near the Mach cone ($R \to 0$), $\varphi^{(1)}$ and its first derivative behave in general as

$$\left.\begin{aligned} \varphi^{(1)} &= D(r, \theta) + E(r, \theta)R + 0(R^{3/2}) && (R \lesseqgtr 0) \\ \varphi_R^{(1)} &= E(r, \theta) + A(r, \theta)(-R)^{1/2} + 0(R) && (R < 0) \\ \varphi_R^{(1)} &= E(r, \theta) + B(r, \theta)R^{1/2} + 0(R) && (R > 0) \end{aligned}\right\} \quad (4)$$

Since $\varphi_{RR}^{(1)}$ tends to infinity as $R \to 0$, it is necessary that the coefficient of $\varphi_{RR}^{(1)}, \varphi_{RR}^{(2)}, \dots$ in Eq. (3) vanishes at $R = 0$ in order to have finite $\varphi_R^{(2)}$, $\varphi_R^{(3)}$. This condition together with the initial condition $\Delta\varphi_R^{(2)} = r^{(1)} = r^{(2)} = 0$ at $t = 0$, and the result $\Delta\varphi^{(2)}(R = 0) = 0$, to be verified later, leads to

$$\left.\begin{aligned} r^{(1)} &= \frac{\gamma+1}{2C_0}\int_0^r E(z, \theta)\,dz + \frac{D(r, \theta)}{C_0} \\ \Delta\varphi_R^{(2)} &= \frac{\gamma+1}{4C_0 r^{1/2}}\int_0^r z^{1/2}[A^2(z, \theta) + B^2(z, \theta)]\,dz \\ \Delta r^{(2)} &= [(\gamma+1)^2/4C_0^2](\bar{A}^2 + \bar{B}^2) \end{aligned}\right\} \quad (5)$$

where

$$\bar{A}^2 = \frac{1}{2}\int_0^r Z^{-1/2}\,dZ \int_0^Z z^{1/2}A^2\,dz$$

and $\bar{B}^2$ is related to B in a similar manner, and where $\Delta(\ )$ indicates the change of a quantity from $R > 0$ to $R < 0$.

The last equation in Eqs. (5) indicates that $\Delta r^{(2)}$ is positive. Following Lighthill's argument,[2] the shock front can be represented by the equation

$$S(t, r, \theta) = C_0 t - r + \epsilon s^{(1)}(r, \theta) + \epsilon^2 s^{(2)} + 0(\epsilon^3) = 0 \quad (6)$$

with $s^{(1)} = r^{(1)}$ and $r^{(2)}(R < 0) \geq s^{(2)} \geq r^{(2)}(R > 0)$. For convenience, an unknown function $F(r, \theta)$ is introduced as defined by

$$\left.\begin{aligned} s^{(2)} - r^{(2)} &= \frac{(\gamma+1)^2}{4C_0^2}(F + \bar{B}^2) \quad (R > 0) \\ r^{(2)} - s^{(2)} &= \frac{(\gamma+1)^2}{4C_0^2}(\bar{A}^2 - F) \quad (R < 0) \end{aligned}\right\} \quad (7)$$

The shock conditions are $\Delta q_t = 0$ and $\Delta q_n = [2/(\gamma+1)] \times [(C^2/q_n) - q_n]$ where

$$C^2 = C_0^2 - (2\varphi_t + \varphi_r^2 + \varphi_\theta^2 r^{-2})(\gamma - 1)/2$$

$$q_t = (\varphi_r S_\theta - \varphi_\theta S_r)/(r\sqrt{S_r^2 + S_\theta^2 r^{-2}})$$

$$q_n = (\varphi_t + \varphi_r S_r + \varphi_\theta S_\theta r^{-2})/\sqrt{S_r^2 + S_\theta^2 r^{-2}}$$

Substituting Eqs. (1) and (2) into the first shock condition, we have $\Delta\varphi^{(1)} = 0$ and $\Delta\varphi^{(2)} = 0$, which was used in deriving Eqs. (5). With Eqs. (1), (2) (3), (5), (6), and (7), the second shock condition leads to

$$A\sqrt{\bar{A}^2 - F} + B\sqrt{\bar{B}^2 + F} + \frac{2C_0}{\gamma+1}\Delta\varphi_R^{(2)} = 2(F_r + \bar{B}_r^2) \quad (8)$$

The shock strength is given by

$$\frac{\Delta p}{\rho_0 C_0^2} = \frac{1}{C_0}\left(A\sqrt{\bar{A}^2 - F} - B\sqrt{\bar{B}^2 + F} + \frac{2C_0}{\gamma+1}\Delta\varphi_R^{(2)}\right) \quad (9)$$

where F is the solution of Eq. (8) satisfying the initial condition $F = 0$ at $r = 0$.

The result is applied to study the reflected shock in a Mach reflection raised when a plane shock wave, traveling parallel to a

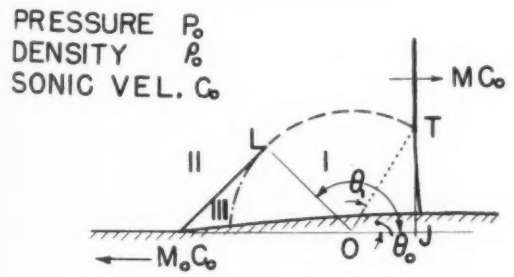

FIG. 1.

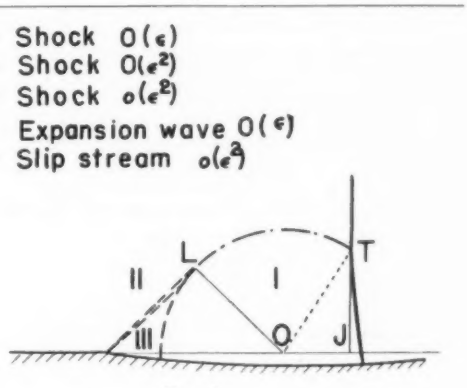

FIG. 2.

plane wall, meets a shallow bump, $y = \epsilon f(x)$, in it. With ϵ, the maximum slope of the bump, as expansion parameter, the first order solution[3] for "supersonic flow" (the wall is moving with supersonic velocity M_0C_0 relative to the undisturbed flow behind the shock) gives

$$\lim_{r \to C_0 t} \frac{p^{(1)}}{\rho_0 C_0^2} = \frac{M - \cos\theta}{1 + M_0 \cos\theta} f'(0^+) H(\theta) r^{-1/2} (Re\sqrt{C_0 t - r})$$

$$= W(\theta) r^{-1/2} (Re\sqrt{C_0 t - r}) \qquad (10)$$

for $\theta > \theta_1 = \pi - \text{arcsec } M_0$, and for $\theta < \theta_1$, the right side of Eq. (10) will have an additional term $M_0^2 \beta^{-1} f'[rv(\theta)]$ where $\beta = \sqrt{M_0^2 - 1}$, $v(\theta) = \cos\theta - \beta \sin\theta + M_0$, and $H(\theta)$ remains positive for the entire range of θ and M_0.

Since the flow is irrotational outside the triangle OTJ, a potential function φ can be introduced to describe the flow near the Mach circle including the triple point T ($\theta = \arccos M$), where both $p^{(1)}$ and its first derivatives are zero. Comparing Eqs. (10) and (4), we have $A = W(\theta) r^{-1/2}$, $B = 0$, $E = C_0 M_0^2 \beta^{-1} f'[rv(\theta)]$, $D = -M_0 C \beta^{-1} f[rv(\theta)]$ for $\theta < \theta_1$ and $A = W(\theta) r^{-1/2}$, $B = E = D = 0$ for $\theta > \theta_1$.

Solving Eqs. (8) and (9), we have the strength of the reflected shock

$$\left.\begin{aligned} \frac{\Delta p}{P_0} = \frac{\Delta p}{\rho C_0^2} &= \frac{3(\gamma+1)\gamma}{16} W(\theta)^2 \quad \text{if } W > 0 \\ &= 0 \qquad\qquad\qquad\quad \text{if } W < 0 \end{aligned}\right\} \qquad (11)$$

The shock front is represented by the equation

$$r - C_0 t = \left[\frac{(\gamma+1)M_0}{2v(\theta)} - 1\right] \epsilon f[rv(\theta)] + 0(\epsilon^2) \quad (\text{for } \theta < \theta_1) \qquad (12)$$

$$r - C_0 t = \epsilon^2 (\gamma+1)^2 W^2(\theta) r/4 + 0(\epsilon^3) \qquad (\text{for } \theta > \theta_1) \qquad (13)$$

The possible shock patterns at an instant $t > 0$ for $f'(0^+)$ greater and smaller than zero are shown in Figs. 1 and 2, respectively.

At point L, $\theta = \theta_1$, where the Mach circle is intersected by a first-order shock or expansion wave, the theory fails.[2]

When the flow is "subsonic," region III vanishes and Eqs. (11) and (13) are true for the entire range of θ. The result agrees with Tan's.[4]

For all cases, at the triple point, $W = 0$, so the strength of reflected shock is $0(\epsilon^2)$. As a consequence, a three-shock configuration with a slipstream does not exist there up to the second order—i.e., the strength of the slipstream is $0(\epsilon^2)$. This statement can be proved more rigorously by using the second-order adiabatic equation and the shock equations across the refracted shock. TJ.

References

[1] Lighthill, M. J., *A Technique for Rendering Approximate Solutions to Physical Problems Uniformly Valid*, Phil. Mag., Series 7, Vol. 40, pp. 1179–1201, November, 1949.

[2] Lighthill, M. J., *The Shock Strength in Supersonic Conical Fields*, Phil. Mag., Series 7, Vol. 40, pp 1202–1221, November 1949.

[3] Ting, L., and Ludloff, H. F., *Aerodynamics of Blasts*, Readers' Forum, Journal of the Aeronautical Sciences, Vol. 18, No. 2, p. 143, February, 1951.

[4] Tan, H. S., *Strength of Reflected Shock in Mach Reflection*, Readers' Forum, Journal of the Aeronautical Sciences, Vol. 18, No. 11, p. 768, November, 1951.

The Reverse-Flow Theorem for Nonstationary Flows

A. H. Flax
Cornell Aeronautical Laboratory, Inc., Buffalo, N.Y.

January 24, 1952

FOR STEADY FLOWS, reverse-flow theorems valid within the limits of linearized theory have been presented in various forms and for various cases by von Kármán,[1] Hayes,[2] Munk,[3] Harmon,[5] Brown,[6] and the writer.[3] The most general forms of these theorems have been given by Ursell and Ward[7] and independently by the writer[8] using different methods of attack. Further work on the subject has disclosed that there is a reverse-flow theorem for nonsteady flows as well. The theorem may be stated (for harmonic oscillation) as

$$\int\int \bar{p}(x, y, t) w(x, y, t)\, ds = \int\int p(x, y, t) \bar{w}(x, y, t)\, ds$$

where p is the instantaneous value of lifting pressure and w is the instantaneous value of prescribed vertical velocity at any point on the wing plan form. $\bar{p}$ and $\bar{w}$ are the same quantities for a flow around the same plan form with the direction of the free-stream velocity, u_0, reversed. p and $\bar{p}$ and w and $\bar{w}$ are so defined as to have the same sense—i.e., p and $\bar{p}$ are both positive for lift upward and w and $\bar{w}$ are both negative when the local angles of attack with respect to respective free-stream directions are positive.

This result can be obtained formally from simple basic considerations. Consider a thin wing of any plan form harmonically oscillating in an incompressible flow. The boundary of the wing is described by a function

$$z = z_1(x, y, t) = z_0(x, y) e^{i\omega t}$$

The velocity potential for such a wing satisfies the equation $\nabla^2\phi = 0$ except on the wing itself and on the vortex sheet trailing behind the wing. The boundary conditions are

$$w_0 = \partial\phi_0/\partial z = U_0(\partial z_0/\partial x) + i\omega z_0 \qquad (1)$$

where $\phi = \phi_0 e^{i\omega t}$ and $w = w_0 e^{i\omega t}$. The pressure at any point (to within an arbitrary additive function of time), according to the linearized Bernoulli equation, is given by

$$\pi = p/\rho = u_0 u + (\partial\phi/\partial t) = u_0 u + i\omega\phi \qquad (2)$$

Here the velocity perturbation components are given by

$$u = \frac{\partial\phi}{\partial x}, \qquad v = \frac{\partial\phi}{\partial x}, \qquad w = \frac{\partial\phi}{\partial z} \qquad (3)$$

The flow is irrotational, and, in particular, $(\partial u/\partial z) - (\partial w/\partial x) = 0$. u_0 is the unperturbed free-stream velocity in the x direction. Over that part of the plane $z = 0$ occupied by the wing, there is a pressure discontinuity $\Delta\pi$ between π on the upper and lower sides of the plane, but everywhere else in the fluid $\Delta\pi$ must be zero. At the trailing edge, the Kutta condition requires that $\Delta\pi = 0$, in order that π go smoothly into its value in the wake. Since u and ϕ satisfy Laplace's equation, π satisfies Laplace's equation as well.

Now, if there be a flow over the same plan form with the direction of the free-stream velocity reversed, there are associated with this flow functions $\bar{\phi}$ and $\bar{\pi}$, which have properties and imposed conditions similar to those of ϕ and π. For the reverse flow case, however, the wake trails from what was in the first case the leading edge, the Kutta condition being applied there. It should be noted in each case that across the plane $z = 0$, $\Delta\phi$ and Δu differ from zero only on the wing and in the wake. In each case, there is a singularity in u and π of the type $1/\sqrt{d}$ at the leading edge, d being the distance from the edge.[6–8]

The volume integral

$$\int\int\int_V (\bar{\pi}\nabla^2\phi - \phi\nabla^2\bar{\pi})\, dv$$

may be written, where V, the volume of integration, is taken over all space outside the wing. It is to be noted that $\nabla^2\phi = 0$ and $\nabla^2\bar{\phi} = 0$ everywhere outside the wing except in the wake; as x approaches $+\infty$ in the wake of the direct flow, $\bar{\phi}$ and $\bar{\pi}$ go to zero; while, as x approaches $-\infty$ in the wake of the reverse flow, ϕ and π go to zero. Further, at the leading edge, where the derivatives of ϕ are singular, $\bar{\pi}$ is zero as required by the Kutta condition in the reverse flow, and similarly for π and $\bar{\phi}$. Thus, Green's theorem may be applied to this volume integral, using as the boundary of the fluid the plane $z = 0$, from $x = -\infty$ to $x = +\infty$. Then,

$$\int\int\int_V (\bar{\pi}\nabla^2\phi - \phi\nabla^2\bar{\pi})\, dv = \int\int_{A_+,\, A_-} \bar{\pi}\frac{\partial\phi}{\partial n}\, ds - \int\int_{A_+,\, A_-} \phi\frac{\partial\bar{\pi}}{\partial n}\, ds = 0 \quad (4)$$

where the area of integration, A, is the entire plane $z = 0$ from $x = -\infty$ to $x = +\infty$. The subscript $+$ denotes the positive side of the plane, while the subscript $-$ denotes the negative side. The n direction is positive for the outward normal of the bounding plane, $z = 0$. Further,

$$\left(\frac{\partial\phi}{\partial n}\right)_+ = \frac{\partial\phi}{\partial z}; \qquad \frac{\partial\phi}{\partial n} = -\frac{\partial\phi}{\partial z}$$

$$\phi_+ = -\phi_-; \qquad \pi_+ = -\pi_-$$

because of the antisymmetry of the lift problem. Thus,

$$\int\int_A \bar{\pi}\frac{\partial\phi}{\partial z}\, ds - \int\int_A \phi\frac{\partial\bar{\pi}}{\partial z}\, ds = 0 \quad (5)$$

where only values on the $+$ side of the plane $z = 0$ need now be considered.

$$\frac{\partial\bar{\pi}}{\partial z} = -u_0\frac{\partial\bar{u}}{\partial z} + i\omega\frac{\partial\bar{\phi}}{\partial z} \quad (6)$$

It should be noted here that the sign of the first term is negative because, with x defined as positive in the direction of the unreversed flow, $u = \partial\bar{\phi}/\partial x$ has a sign convention opposite to the usual one. If the senses of π and w are kept the same for the two flow directions, the signs must be chosen as in this note. By the irrotationality condition

$$\partial\bar{u}/\partial z = \partial\bar{w}/\partial x$$

Also,

$$\partial\bar{\phi}/\partial z = \bar{w}$$

so that

$$(\partial\bar{\pi}/\partial z) = -u_0(\partial\bar{w}/\partial x) + i\omega\bar{w} \quad (7)$$

Thus,

$$\int\int\bar{\pi}\frac{\partial\phi}{\partial z}\, ds - \int\int_A \phi\left[-u_0\left(\frac{\partial\bar{w}}{\partial x}\right) + i\mu\omega\bar{w}\right] ds = 0 \quad (8)$$

The integral

$$u_0\int\int_A \phi\,(\partial\bar{w}/\partial x)\, ds$$

may be integrated by parts on x; since at $x = -\infty$, $\phi = 0$, while at $x = +\infty$, $\bar{w} = 0$, there results

$$u_0\int\int_A \phi\frac{\partial\bar{w}}{\partial x}\, ds = -u_0\int\int_A \frac{\partial\phi}{\partial x}\bar{w}\, ds = -u_0\int\int_A u\bar{w}\, ds \quad (9)$$

Substituting this result in Eq. (8),

$$\int\int_A \bar{\pi}\frac{\partial\phi}{\partial z}\, ds - \int\int (u_0 u + i\omega\phi)\,\bar{w}\, ds = 0 \quad (10)$$

But according to Eq. (2), the term in brackets in the second integral is simply π, so that

$$\int\int\bar{\pi}w\, ds = \int\int\pi\bar{w}\, ds \quad (11)$$

where the integrations are over the wing plan form only, since π and $\bar{\pi}$ are both zero except on the wing. This is the desired result that reduces to the theorems of Ursell and Ward[7] and the writer[8] for steady flows,

$$\int\int\bar{u}\, w\, ds = \int\int u\bar{w}\, ds \quad (12)$$

The present result is also true for compressible nonsteady flows. The extension of the proof will be given in a later paper. For the special case of two-dimensional incompressible nonsteady flows, Schwartz[9] has given formulas for the lift and moment explicitly in terms of $w(x, t)$. His results are exactly those obtained by the direct application of Eq. (11) to the case he considered.

An adjoint variational principle of the type discussed by the writer for steady flows[8] may also be derived for unsteady flows by methods entirely analogous to those for the steady-flow case.

References

[1] von Kármán, Th., *Supersonic Aerodynamics—Principles and Applications*, Journal of the Aeronautical Sciences, Vol. 14, No. 7, pp. 373–409, July, 1947.

[2] Hayes, W. D., *Linearized Supersonic Flow*, North American Aviation, Inc., Report AL-222, June 18, 1947.

[3] Flax, A. H., *Relations Between the Characteristics of a Wing and Its Reverse in Supersonic Flow*, Journal of the Aeronautical Sciences, Vol. 16, No. 8, pp. 496–504, August, 1949.

[4] Munk, M. M., *The Reversal Theorem of Linearized Supersonic Airfoil Theory*, Journal of Applied Physics, Vol. 21, No. 2, pp. 159–161, February, 1950.

[5] Harmon, S., *Theoretical Relations Between the Stability Derivatives of a Wing in Direct and in Reverse Supersonic Flow*, N.A.C.A. T.N. No. 1943, September, 1949.

[6] Brown, C. E., *The Reversibility Theorem for Thin Airfoils in Subsonic and Supersonic Flow*, N.A.C.A. T.N. No. 1944, September, 1949.

[7] Ursell, F., and Ward, G. N., *On Some General Theorems in the Linearized Theory of Compressible Flow*, Quarterly Journal of Mechanics and Applied Mathematics, Vol. III, Part 3, pp. 326–348, September, 1950.

[8] Flax, A. H., *General Reverse Flow and Variational Theorems in Lifting-Surface Theory*, C.A.L. Report No. 34, May, 1951. (To be published in the Journal of the Aeronautical Sciences.)

[9] Schwartz, L., *Berechnung der Druckverteilung einer harmonisch sich verformenden Tragfläche in ebener Strömung*, Luftfahrtforschung, Vol. 17, pp. 379–386, 1940.

Comments on "Aerodynamic Coefficients of an Oscillating Airfoil in Two-Dimensional Subsonic Flow"

Henry E. Fettis

Mathematician, Flight Research Laboratory, Wright Air Development Center, Wright-Patterson A.F. Base, Dayton, Ohio

January 7, 1952

In the subject paper,[1] the authors give values for lift and moment coefficients for a two-dimensional oscillating airfoil moving at subsonic velocity. A cursory examination of the values presented indicates that they are subject to considerable question, particularly at higher values of the reduced frequency, ω. The authors themselves have noted that the values agree poorly with those previously computed by the Dietze method, and it is difficult to believe that the latter results are greatly in error, since they have been derived independently[2] by a different method, the results agreeing except for differences that are clearly of second order in magnitude. Since the publication of reference 2, additional calculations have been made[4] which further confirm the correctness of the Dietze values.

In Figs. 1a, and 1b, a plot is shown of the lift coefficient L_h as defined in reference 3, which is related to the quantities k_a' and k_a'' in reference 1 according to the equation

$$L_h = (1/\omega^2)\,(k_a' + ik_a'') \quad (1)$$

Fig. 1a indicates fairly good agreement with Dietze down to a value of $(1/\omega)$ equal to approximately 1.5. For $1/\omega < 1.5$, a marked deviation in the real part takes place which is difficult to account for in view of the fact that the Dietze values for this quantity approach the known value of 1 as $1/\omega \to 0$.

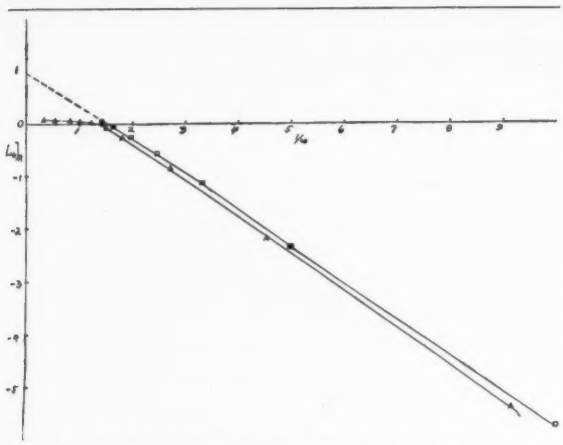

FIG. 1a. Real part of L_A vs. $1/\omega$; $\beta = 0.7$. □—Dietze; △—Timman

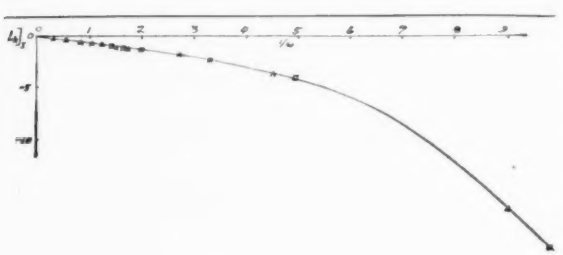

FIG. 1b. Imaginary part of L_A vs. $1/\omega$; $\beta = 0.7$. [—Dietze; —Timman.

A further difficulty lies in the fact that the various coefficients are not mutually in agreement. This may be demonstrated with the aid of the following recently demonstrated relation:[5]

$$k_a = i\omega(m_a + k_b) \tag{2}$$

A spot check of the values in Table 1 of reference 1 indicates that for the first few values of ω at each Mach Number, the above relation is satisfied with a reasonable degree of accuracy, the differences being possibly due to rounding-off errors. As ω and M increase, values on the right-hand side and left-hand side of Eq. (2) become widely separated. On the other hand, the values of Dietze check reasonably well by Eq. (2), with discrepancies in only the third or fourth significant figure. The values computed in reference 5 satisfy Eq. (2) to the fourth or fifth digit, in general.

REFERENCES

[1] Timman, R., van de Vooren, A. I., and Greidanus, J. H., *Aerodynamic Coefficients of an Oscillating Airfoil in Two-Dimensional Subsonic Flow*, Journal of the Aeronautical Sciences, Vol. 18, No. 12, pp. 797–802, December, 1951.

[2] Fettis, Henry E., *Calculation of Non-Stationary Air Forces at Subsonic Speeds*, O.A.R. Technical Report No. 5, March, 1951.

[3] Smilg, Ben, and Wasserman, Lee S., *Application of Three-Dimensional Flutter Theory to Aircraft Structures*, A. F. Technical Report No. 4798, July 9, 1942.

[4] Fettis, Henry E., *Tables of Lift and Moments Coefficients for an Oscillating Wing-Aileron Combination in Two-Dimensional Subsonic Flow*, A.F. Technical Report No. 6688, November, 1951.

[5] Fettis, Henry E., *Reciprocal Theorems in the Theory of Linearized Unsteady Flow Over Thin Airfoil Sections* (paper to be presented at 2nd Midwest Conference on Fluid Mechanics, Columbus, Ohio, March 17, 18, 19, 1952).

Comments on "Uniformly Loaded Semi-Infinite Wedge-Shaped Plates"

M. L. Williams, Jr.

Assistant Professor, Guggenheim Aeronautical Laboratory, California Institute of Technology, Pasadena, Calif.

February 11, 1952

IN A. J. A. MORGAN'S RECENT NOTE (Readers' Forum, JOURNAL OF THE AERONAUTICAL SCIENCES, Vol. 18, No. 12, p. 845, December, 1951), it is stated that "the deflections of a uniformly loaded semi-infinite wedge-shaped plate of constant thickness are explicitly determined for the case where one edge is free and the other is clamped." Then, in one of the concluding paragraphs, it is stated that, for the boundary conditions considered, "no stress singularity occurs at the corner for any wedge angle $0 < 2\beta < \pi$."

While both statements are correct, it is believed that the manner of presentation leaves an impression that the stresses at the corner are *always* nonsingular. The problem is discussed in references 1 and 2, where it is shown that any attempt to prescribe arbitrary boundary conditions other than those compatible with Eq. (17) of Morgan's Readers' Forum item will indeed give rise to a mathematically infinite stress at the corner for certain opening angles. In particular, while Eq. (17) is the same form of solution given in reference 1, it may be shown that, if a free edge is desired along a circumferential boundary, for example, the stresses at the vertex are unbounded for opening angles greater than approximately 90°.

It should be emphasized then that the corner stresses for this uniformly loaded cantilever plate (and actually even under more general loadings) will only be nonsingular in certain cases. The special solution, Eq. (17), is therefore thought to have somewhat limited practical applicability.

REFERENCES

[1] Williams, M. L., *The Plate Problem for a Cantilever Sector of Uniform Thickness*, Air Force Technical Report No. 5761, Part 6, November, 1950.

[2] Williams, M. L., *Surface Stress Singularities Resulting from Various Boundary Conditions in Angular Corners of Plates Under Bending*, First Natl. Cong. of Appl. Mech., Illinois Institute of Technology, June, 1951.

The Superposition of High-Intensity Periodic Waves on a Steady Flow

J. C. Truman and N. J. Lipstein

General Engineering Laboratory, General Electric Company, Schenectady, N. Y.

January 24, 1952

INTEREST IN OSCILLATORY FLOW PHENOMENA has prompted an investigation of experimental methods for superposing high-intensity audiofrequency pressure oscillations on a steady flow. Pressure oscillations that are treated in the field of acoustics are usually assumed to be periodic and to have small amplitude, permitting the use of the linearized wave equation. Shock waves, on the other hand, may involve large pressure ratios but are in the usual case nonperiodic. Finite amplitude effects, which are found to change the shape of periodic waves of high intensity, are discussed in the present note.

It is readily seen[1] that a wave of finite amplitude cannot be propagated in a gaseous medium without change in wave shape. From a consideration of the exact equation of motion, Fay[2] has shown that a transfer of energy from components of lower frequency to those of higher frequency takes place due to the nonlinearity of the system and the interaction of harmonics. The effect of this transfer is counteracted by that of viscosity, which

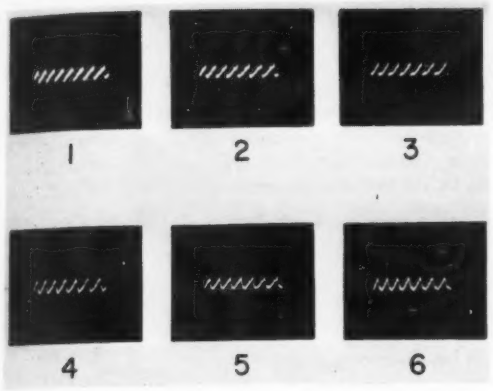

FIG. 1.

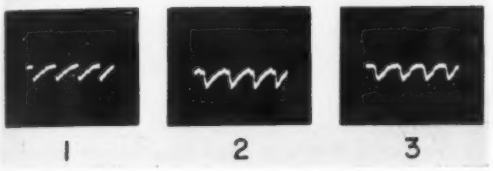

FIG. 2.

attenuates higher frequency components more than those of lower frequency. Hence, for any arbitrary intensity and frequency, there must exist an equilibrium wave form, having harmonic content in such relationship that the decrease in amplitude of any component due to viscosity is exactly compensated by the increase due to nonlinearity. Any wave approaches this equilibrium form as it progresses. Conditions for stability are found to depend on intensity, however, so that the equilibrium form is not permanent but changes as intensity decreases. Experimental evidence of finite amplitude effects, substantiating Fay's theoretical analysis, has been reported by Allen and Rudnick.[3] Data obtained by the present authors for high-intensity waves superposed on a steady flow also indicate the presence of such effects.[4]

Two different "flow-chopping" devices were used to modulate the airflow in a smooth pipe $3^3/_4$ in. in inside diameter. A gate modulator, consisting of a rotating wheel with slots equally spaced around its periphery, was mounted so that the flow exit from the pipe was alternately opened and closed. A sleeve modulator was formed by two coaxial cylinders having aligning port configurations in their walls. As the outer cylinder was rotated about the inner one, which formed a section of the pipe containing the air stream, the ports were alternately opened and closed. Both modulators were belt-driven by electric motors. A Massa microphone was used to obtain pressure responses at six stations along the pipe.

Fig. 1 shows oscillograph traces obtained at stations 1 through 6, located at distances upstream from the gate modulator equal to 65, 57, 50, 31, 24, and 16 in., respectively. The change in wave shape from a triangular wave near the modulator to a sharp sawtooth at station 1 is clearly seen. Here the velocity of the air stream was 315 ft. per sec., and the signal frequency was 275 cycles per sec. The average sound intensity was 167 db., corresponding to a pressure amplitude slightly less than 1 lb. per sq. in. Fig. 2 illustrates the wave shapes at stations 1, 2, and 3 located 24, 16, and 9 in., respectively, upstream from the sleeve modulator. Air velocity was 380 ft. per sec., signal frequency was 340 cycles per sec., and average intensity was 166 db. Here also, the change to the sawtooth wave form is noted.

This work was part of an investigation performed at the request of the Propulsion Group, Flight Research Laboratory, Research Division of the Wright Air Development Center.

REFERENCES

[1] Liepmann, H. W., and Puckett, A. E., *Introduction to Aerodynamics of a Compressible Fluid*, pp. 45–47; John Wiley & Sons, Inc., New York, 1947.

[2] Fay, R. D., *Plane Sound Waves of Finite Amplitude*, The Journal of the Acoustical Society of America, Vol. 3 No. 2, pp. 222–241, October, 1931.

[3] Allen, C. H., and Rudnick, I., *A Powerful High Frequency Siren*, The Journal of the Acoustical Society of America, Vol. 19, No. 5, pp. 857–865, September, 1947.

[4] Truman, J. C., and Lipstein, N. J., General Electric Technical Information Series Report No. R51GL-127, Part 1.

Recovery Factors for the Laminar "Separation" and Stagnation Flows*

S. Levy and R. A. Seban

Research Engineer and Associate Professor, respectively, Institute of Engineering Research, University of California at Berkeley

January 30, 1952

INTRODUCTION

ADIABATIC WALL TEMPERATURES for the two-dimensional incompressible "wedge flows" corresponding to the Hartree[1] solution of the momentum equation have been computed by Eckert and Drewitz[2] and Schuh[3] and can be inferred from certain calculations of Tifford.[4] Some of these results are shown in Table 1 in terms of the recovery factor

$$r = 1 - [(T_s - T_{aw})/(U_1^2/2GJc_p)]$$

TABLE 1

Recovery Factors for "Wedge Flows" at a Prandtl Number of 0.70

β	1.0	0	−0.14	−0.20
Eckert-Drewitz	0.791	0.833	0.838	...
Schuh	0.840	0.840	...	...
Tifford	0.830	0.835	...	...
Present results	0.815	...	...	0.762

The theoretical results now reported were obtained to establish the value of the recovery factor for the velocity profile in the boundary layer corresponding to the value $\beta = -0.20$, which yields zero shear at the wall and, in consequence, corresponds to conditions at separation of the boundary layer. In connection with this work, the recovery factor for the case $\beta = 1.0$ (stagnation flow) was also determined.

NOMENCLATURE

$b(\eta)$	=	function defined by Eq. (7)
B_n	=	coefficient obtained from Eq. (9)
$c(\eta)$	=	function defined by Eq. (7)
C	=	proportionality constant ($U_1 = Cx^m$)
C_n	=	coefficient obtained from Eq. (9)
e	=	step interval in the finite difference solution
E_n	=	extrapolation error
$f(\eta)$	=	solution to Eq. (3) (Hartree profiles)
$g(\eta)$	=	function defined by Eq. (5)
G	=	gravitational constant (32.2 ft./sec.^{2})
J	=	conversion factor (778 ft.lbs. per B.t.u.)

* This work was carried out at the University of California under the sponsorship of the the Air Materiel Command (Air Force Contract No. 33-038-12941).

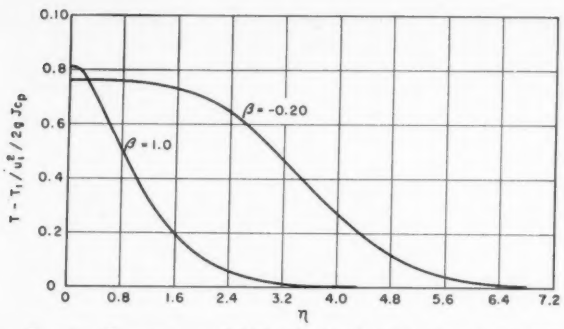

FIG. 1. Temperature field in the insulated laminar boundary layer for "separation" and stagnation flows with Prandtl Number of 0.70.

k = thermal conductivity (B.t.u./hr. ft.² °F./ft.)
m = exponent in the statement ($U_1 = Cx^m$)
M_1 = local free-stream Mach Number
p = pressure in the boundary layer (lbs. per sq.ft.)
p_n, q_n = coefficients defined by Eq. (13)
r = recovery factor
T = temperature in the boundary layer (°F.)
T_{aw} = temperature of the insulated surface (°F.)
T_s = stagnation temperature (°F.)
T_1 = temperature at the edge of the boundary layer (°F.)
u = velocity component of flow in x direction (ft. per sec.)
U_1 = velocity at the edge of the boundary layer (ft. per sec.)
v = velocity perpendicular to body surface (ft. per sec.)
x = distance along the body surface (ft.)
y = distance normal to the body surface (ft.)
β = velocity distribution parameter
η = independent variable occurring in the Hartree profiles
θ = dimensionless temperature $[(T - T_1)/(U_1^2/2GJc_p)]$
μ = absolute viscosity (lbs. sec./ft.²)
ν = kinematic viscosity (ft.²/sec.)
σ = Prandtl Number, $\mu c_p/k$, dimensionless
ψ = the stream function

ANALYSIS

The momentum and energy equations upon which the solutions considered here are based are written in the following form:

$$\rho\left(u\frac{\partial u}{\partial x} + v\frac{\partial u}{\partial y}\right) + \frac{\partial p}{\partial x} = \mu\frac{\partial^2 u}{\partial y^2} \tag{1}$$

$$\rho\left(u\frac{\partial T}{\partial x} + v\frac{\partial T}{\partial y}\right) = \frac{k}{c_p}\frac{\partial^2 T}{\partial y^2} + \frac{\mu}{c_p}\left(\frac{\partial u}{\partial y}\right)^2 \tag{2}$$

Eckert and Drewitz have presented a consideration that indicates that compressible flows may be defined by these forms of the equations for Mach Numbers in the range $0 < M_1 < 0.9$.

Transformation of Eqs. (1) and (2) through Hartree variables

$$\eta = \sqrt{[(1 + m)/2](U_1/\nu x)}\,y$$

$$\psi = \sqrt{[2/(1 + m)]\nu x U_1}\,f(\eta)$$

gives, for $U_1 = Cx^m$ and $\beta = 2m/(m + 1)$,

$$f'''^* + ff'' + \beta(1 - f'^2) = 0 \tag{3}$$

$$\theta'' + f\sigma\theta' - 2\beta\sigma f'\theta + 2\sigma f''^2 = 0 \tag{4}$$

with $u/U_1 = f'(\eta)$ and $\theta(\eta) = (T - T_1)/(U_1^2/2GJc_p)$.

* The primes indicate the order of differentiation with respect to η.

The boundary conditions are

$$f' = 0 \qquad \theta' = 0 \qquad \eta = y = 0$$
$$f' = 1 \qquad \theta = 0 \qquad \eta = y \to \infty$$

Introduction of the function of $g(\eta)$ defined from

$$\theta = ge^{-(1/2)\int_0^\eta \sigma f\,d\eta} \tag{5}$$

yields, for the energy equation,

$$g'' = b(\eta)g + c(\eta) \tag{6}$$

where

$$b(\eta) = 2\beta\sigma f' + (1/2)\sigma f' + (1/4)\sigma^2 f^2 \tag{7}$$
$$c(\eta) = -2\sigma f'^2 e^{(1/2)\int_0^\eta \sigma f\,d\eta}$$

The boundary conditions become

$$g'(0) = 0; \qquad g(\eta \to \infty) = 0$$

Reduction of Eq. (6) to finite difference form, with the increments in g being distant e apart and subscript n denoting the number of the increment beginning with zero at the plate, produces the equation

$$g_{n+1} = B_n g_n - g_{n-1} + C_n \tag{8}$$

where

$$B_n = 2 + e^2 b(\eta) \tag{9}$$
$$C_n = e^2 c(\eta)$$

The calculations leading to g_n for large n were accomplished on a calculator in which five decimals were carried. The increment $e = \Delta\eta$ was taken as 0.1.

The boundary condition $g'(0) = 0$ is approximated by a parabolic curve in the same manner as by Eckert and Drewitz. Thus,

$$g_2 = 4g_1 - 3g_0 \tag{10}$$

Eq. (10) combined with the corresponding Eq. (8) yields

$$g_1 = \frac{2}{4 - B_1}g_0 - \frac{C_1}{4 - B_1} \tag{11}$$

Thus g_2 and all other g_n can be expressed in terms of g_0 or

$$g_n = p_n g_0 - q_n \tag{12}$$

where

$$p_n = B_{n-1}p_{n-1} - p_{n-2} \tag{13}$$
$$q_n = B_{n-1}q_{n-1} - q_{n-2} + C_{n-1}$$

with $p_1 = 2/(4 - B_1)$, $p_0 = 1$, $q_1 = C_1/(4 - B_1)$, and $q_0 = 0$.

In virtue of the boundary condition as $\eta \to \infty$, g_n becomes zero for extremely large n. In the calculation if the value of g_0 was unaffected within the fifth decimal by evaluation from Eq. (12) and with $g_n = 0$ for two positions n and $n - 1$, the number of increments was deemed sufficient.

The recovery factor is obtained as

$$r = \theta(0) = g(0) = g_0 \tag{14}$$

and can be evaluated from the known value of g_0.

RESULTS

Calculations have been carried out for the following cases:

$\beta = \quad 1.0$ (stagnation flow)
$\beta = -0.20$ (separation flow)

for a Prandtl Number σ of 0.7.

The distribution of the temperature within the boundary layer is shown in Fig. 1, and the computed values of the recovery factor are shown in Table 1: $r = 0.815$ for $\beta = 1.0$; $r = 0.762$ for $\beta = -0.20$.

Discussion

The present result for the stagnation flow as revealed from Table 1 lies between the value of Eckert and Drewitz and that inferred from Tifford. The uniform trend of the recovery factor from the stagnation and flat plate flows would by the present result involve an increase of only 2 per cent in the recovery factor. Small increases in the recovery factor in this range are indicated by some experimental results and not by others, but the small increase may account for a masking of the effect by experimental error.

The decrease in the recovery factor for the separation flow is expected in terms of the movement of the region of maximum dissipation away from the wall. The reduction is apparently rapid and is not reflected in a contrast of the Eckert and Drewitz results for $\beta = -0.14$ and $\beta = 0$. Such a rapid decrease suggests the utilization of the effect for the indication of flow separation, and low values of the recovery factor have been observed in the separation region in experimental results for air flow over a 1:3 elliptic cylinder.

The accuracy of the solution here presented has been examined in detail, by the methods indicated in reference 5. By developing g_{n+1} and g_n into a Taylor series, the interpolation error can be determined

$$E_n = (e^4/12)\,(d^4g/d\eta^4)$$

This error is much smaller than the corresponding one in the Eckert-Drewitz solution and partially explains the different value obtained for $\beta = 1.0$. The overall error of the present solution is estimated to be below $^1/_2$ per cent.

References

[1] Hartree, D. R., *On an Equation Occurring in Falkner and Skan's Approximate Treatment of the Equation of the Boundary Layer*, Proc. Camb. Phil. Soc., Vol. 33, pp. 223–239, 1937.

[2] Eckert, E., and Drewitz, O., *Calculation of the Temperature Distribution in the Laminar Boundary Layer of Unheated Bodies in a Flow at High Velocity*, Luftf. Forsch., Vol. 19, 1942.

[3] Schuh, H., *Laminar Heat Transfer in Boundary Layers at High Velocities*, FB 2019 (1944); ZWB, R. and T. 810 (1947); MAP Volkenrode.

[4] Tifford, A. N., *Some Prandtl Number Effects on the Transfer of Heat*, Engineering Experiment Station News, The Ohio State University, February, 1950.

[5] Levy, S., *Heat Transfer to Constant Property Laminar Boundary Layer Flows with Power Function Free Stream Velocity and Wall Temperature Variation*, University of California, Institute of Engineering Research, Series 41, Issue 5, 1951.

Comments on "Turbulent Boundary-Layer Characteristics . . ."

Marvin L. Luther

Research Department, U.S. Naval Ordnance Test Station, Inyokern, China Lake, Calif.

January 23, 1952

In the paper "Turbulent Boundary-Layer Characteristics at Supersonic Speeds—Theory and Experiment" (Journal of the Aeronautical Sciences, Vol. 17, No. 9, p. 585, September, 1950), R. E. Wilson obtains the equation [Eq. (32), p. 588]

$$\frac{\sin^{-1}\sqrt{\sigma}}{\sqrt{\sigma}}\left(1 + C_\theta\frac{\gamma-1}{2}M_1^2\right)^{-1/2}\frac{0.242}{\sqrt{C_F}} = \log_{10}(C_F R) - 0.768\log_{10}\left(1 + C_\theta\frac{\gamma-1}{2}M_1^2\right)$$

where

$$\sigma = [(\gamma-1)/2]M_1^2/\{1 + [(\gamma-1)/2]M_1^2\}$$

which relates skin friction, C_F, to free-stream Mach Number M_1, Reynolds Number R, specific-heat ratio γ, and Hilton's temperature recovery coefficient C_θ.

In order to obviate the use of a method of successive approximations for the determination of C_F and thus reduce the time required for computation, an equation was sought which would present C_F as an explicit function of M_1 and R. Assuming the fluid to be air with $\gamma = 1.40$ and $C_\theta = 0.88$, the equation

$$C_F = 0.0631\,e^{-0.172\,M_1}\,R^{-0.182}$$

yields values for C_F which agree with those obtained by the parent equation within 4 per cent in the ranges $1 \leq M_1 \leq 3$, $4(10^6) \leq R \leq 10^8$.

Correction for Aspect Ratio of the Indicial Lift Functions of Wagner and Küssner

R. H. Scanlan

National Research Fellow, Ecole Nationale Supérieure de l'Aéronautique, Paris, France

February 8, 1952

Reissner[1] has established the correction $\sigma(k)$ to be added to Theodorsen's two-dimensional circulation function $C(k)$ when the transition is made from a two- to a three-dimensional sinusoidal flutter study. Recently, Ashley[2] has produced a similar correction term $\sigma_\beta(k)$ to be used in the case of a swept wing, where Reissner's correction is inapplicable.

With either of these corrections σ, we have the basis for the correction of the well-known indicial lift functions $k_1(s)$ of Wagner and $k_2(s)$ of Küssner for aspect ratio. It must be understood that, for use in correcting these latter functions, the functions σ, which are valid only for harmonic motion, must be prepared separately for each component (flexion, torsion, etc.) of each mode of wing response envisaged and, with each mode, for a complete range of reduced frequency $k = b\omega/v$: $0 \leq k \leq \infty$. Account must, of course, be taken of the geometry of the specific wing studied.

Let the complex σ be written

$$\sigma(k) = \sigma_R(k) + i\sigma_I(k) \tag{1}$$

whence the corrected $C(k)$ is

$$C(k) + \sigma(k) = F(k) + \sigma_R(k) + i[G(k) + \sigma_I(k)] \tag{2}$$

Now Garrick,[3] for example, has established the relations

$$\left.\begin{aligned} k_1(s) &= \frac{2}{\pi}\int_0^\infty \frac{F(k)}{k}\sin ks\,dk \\ &= 1 + \frac{2}{\pi}\int_0^\infty \frac{G(k)}{k}\cos ks\,dk \end{aligned}\right\} \tag{3}$$

which relate $k_1(s)$ to $C(k) = F(k) + iG(k)$. Garrick[4] has also pointed out the relation that must hold between $k_2(s)$ and $k_1(s)$:

$$\left.\begin{aligned} k_2(s) &= \frac{1}{\pi}\int_0^s k_1(s_1)\sqrt{\frac{s-s_1}{2-s+s_1}}\,ds_1 + \frac{1}{\pi}\sqrt{s(2-s)} \qquad (0 < s < 2) \\ &= \frac{1}{\pi}\int_{s-2}^s k_1(s_1)\sqrt{\frac{s-s_1}{2-s+s_1}}\,ds_1 \qquad (s > 2) \end{aligned}\right\} \tag{4}$$

The linearity of the entire theory permits the following simple generalizations, which define $[k_1(s)]_{A.R.}$ and $[k_2(s)]_{A.R.}$ as modified for aspect ratio for a particular wing and specified mode of that wing:

$$[k_1(s)]_{A.R.} = \frac{2}{\pi}\int_0^\infty \frac{F(k) + \sigma(k)}{k}\sin ks\,dk \tag{5}$$

$$[k_2(s)]_{A.R.} = \frac{1}{\pi}\int_0^s [k_1(s)]_{A.R.}\sqrt{\frac{s-s_1}{2-s+s_1}}\,ds_1 + \frac{1}{\pi}\sqrt{s(2-s)} \quad (0<s<2)$$
$$= \frac{1}{\pi}\int_{s-2}^s [k_1(s)]_{A.R.}\sqrt{\frac{s-s_1}{2-s+s_1}}\,ds_1 \quad (s>2) \qquad (6)$$

The above aspect-ratio corrections are made in the same sense as those of Reissner—that is, for wake effects only, not accounting for changes in apparent mass effects. Such apparent mass effects are represented, for example, in the uncorrected term $(1/\pi)\sqrt{s(2-s)}$ above. The resulting corrected terms may be employed for general unsteady three-dimensional analysis in the manner suggested, for example, by Baird and Kelley[5] for two dimensions, the usual Theodorsen lift circulation terms now being replaced by the following terms containing superposition integrals of the indicial lift functions:

(1) Lift P for an arbitrary vertical movement of the wing defined by a vertical velocity function $w(s)$ at the three-quarter chord point:

$$\frac{P}{2\pi\rho v b} = w(0)\,[k_1(s)]_{A.R.} + \int_0^s [k_1(s-s_1)]_{A.R.}\frac{d}{ds_1}w(s_1)\,ds_1 \qquad (7)$$

(2) Lift P resulting from the penetration of a gust of arbitrary vertical velocity distribution $\bar{w}(s)$:

$$\frac{P}{2\pi\rho v b} = \bar{w}(0)\,[k_2(s)]_{A.R.} + \int_0^s [k_2'(s-s_1)]_{A.R.}\,\bar{w}(s_1)\,ds_1 \qquad (8)$$

where $k_2'(s) = dk_2(s)/ds$.

Bisplinghoff, Isakson, and O'Brien[6] have already pointed out the application of Eq. (3) in the case of the generalization to their indicial counterparts of functions of harmonic oscillatory lift at high subsonic speeds in two-dimensional flow.

References

[1] Reissner, E., N.A.C.A. T.N. No. 1194, 1947.

[2] Ashley, H., *Some Unsteady Aerodynamic Problems Affecting the Dynamic Stability of Aircraft*, Doctoral thesis, M.I.T., January, 1951.

[3] Garrick, I. E., N.A.C.A. T.R. No. 629, 1938.

[4] Garrick, I. E., *On Some Fourier Transforms in the Theory of Nonstationary Flows*, Proc. Fifth Intl. Congr. Appl. Mech., pp. 590–593, 1938.

[5] Baird, E. F., and Kelley, H. J., *Formulation of the Flutter Problem for Solution on an Electronic Analog Computer*, Readers' Forum, Journal of the Aeronautical Sciences, Vol. 17, No. 3, p. 189, March, 1950.

[6] Bisplinghoff, R. L., Isakson, G., and O'Brien, T. F., *Gust Loads on Rigid Airplanes with Pitching Neglected*, Journal of the Aeronautical Sciences, Vol. 18, No. 1, p. 33, January, 1951.

Design of Nozzles Having Continuous Wall Curvature

J. C. Crown

Hyperballistics Division, Naval Ordnance Laboratory, White Oak, Silver Spring, Md.

February 1, 1952

MANY NOZZLES FOR SUPERSONIC WIND TUNNELS are now designed using the Foelsch method[1] with a cubic initial curve.[2] Nozzle contours obtained from the Foelsch method have inherently a discontinuity in curvature at the "inflexion" point. Since a flexible plate cannot be bent to follow a nozzle contour having a discontinuity in curvature, it seemed desirable to develop a method for designing nozzles having continuous wall curvature at all points. The basic formulas for designing such a nozzle are presented herein.*

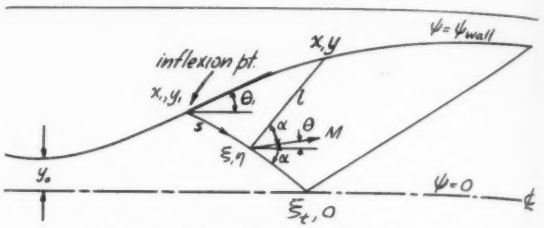

FIG. 1. Schematic illustrating notation.

Symbols not shown in Fig. 1 are as follows:

ν = expansion angle
c = local velocity of sound
ρ = density

Along the Mach line from the inflexion point we have the characteristic condition

$$\theta = \nu_i - \nu \qquad (1)$$

where ν_i is the value of ν in the test rhombus. Furthermore,

$$d\psi/ds = -\rho c \qquad (2)$$
$$d\xi/ds = \cos(\theta-\alpha) \qquad (3)$$
$$d\eta/ds = \sin(\theta-\alpha) \qquad (4)$$

Eliminating s and integrating, we have

$$\xi_t - \xi = \int_0^{\psi}\frac{\cos(\alpha-\theta)}{\rho c}\,d\psi = y_0\int_0^{\bar{\psi}} F\cos(\alpha-\theta)\,d\bar{\psi} \qquad (5)$$

and

$$\eta = \int_0^{\psi}\frac{\sin(\alpha-\theta)}{\rho c}\,d\psi = y_0\int_0^{\bar{\psi}} F\sin(\alpha-\theta)\,d\bar{\psi} \qquad (6)$$

where

$$F = \left\{\frac{1+[(\gamma-1)/2]\,M^2}{(\gamma+1)/2}\right\}^{(1/2)(\gamma+1)/(\gamma-1)}$$

and $\bar{\psi} = \psi/\psi_{wall}$; $\bar{\psi} = 0$ at centerline, $\bar{\psi} = 1$ at wall. The coordinates ξ, η of said Mach line as functions of $\bar{\psi}$ can now be found if $\theta = \theta(\bar{\psi})$ were known. This θ distribution will be further discussed below.

Knowing the coordinates of the inflexion-point Mach line, we can find the coordinates of the downstream nozzle contour. Since Mach lines of one family are straight downstream from the inflexion-point Mach line, it follows that

$$x = \xi + l\cos(\theta+\alpha) \qquad (7)$$
$$y = \eta + l\sin(\theta+\alpha) \qquad (8)$$

where l follows from the equation of continuity

$$l = \frac{\psi_{wall}-\psi}{\rho c} = y_0 F(1-\bar{\psi}) \qquad (9)$$

From the preceding equations it can be shown that for the wall curvature to be continuous, $d\theta/d\psi$ must vanish at the inflexion point $\xi = x_1$ and $\xi = \xi_t$. Furthermore, for the gradient of curvature to be finite, $d^2\theta/d\psi^2 < \infty$ at these points. These conditions are satisfied by adopting a distribution along the inflexion-point Mach line

$$\theta = \theta_1\sin^2(\pi/2)\bar{\psi} \qquad (10)$$

for example. The integrals (5) and (6) can now be evaluated with the aid of Eq. (1) and the usual expressions for ν and α.

* After the completion of this analysis, the writer became acquainted through private channels with another method, developed by A. E. Puckett, to achieve continuous wall curvature.

The inflexion point is thus now a true one with zero curvature. It seems logical, as indicated in the remark to follow, that the nozzle throat should also have zero curvature. This can best be seen, perhaps, by starting with a distribution such as Eq. (10) and working backwards using the method of characteristics. The simplest upstream contour satisfying the imposed conditions of ordinate, slope, and curvature is then a quartic given by

$$y = y_0 + x_1 \tan \theta_1 \left(\frac{x}{x_1}\right)^3 \left(1 - \frac{x}{2x_1}\right) \tag{11}$$

where

$$x_1 = 2(y_1 - y_0) \cot \theta_1 \tag{12}$$

In short, the method is then as follows:

(1) Start with a $\theta(\bar{\psi})$ distribution along inflexion-point Mach line—e.g., Eq. (10).

(2) Integrate to obtain ξ, η (coordinates of said Mach line).

(3) Coordinates of inflexion point are found taking $\bar{\psi} = 1$ as upper limits of integrals.

(4) Calculate x, y (coordinates of downstream nozzle contour).

(5) Calculate upstream nozzle contour using either a quartic or by working backwards using method of characteristics.

References

[1] Foelsch, Kuno, *A New Method of Designing Two-Dimensional Nozzles for a Parallel and Uniform Jet*, North American Aviation Report No. NA-46-235, March, 1946.

[2] Crown, J. C., *Supersonic Nozzle Design*, N.A.C.A. T.N. No. 1651, June, 1948.

Further Comments on "The Effect of Surface Cooling on Laminar Boundary-Layer Stability"

Martin Bloom

Instructor, Department of Aeronautical Engineering and Applied Mechanics, Polytechnic Institute of Brooklyn

January 24, 1952

THE WRITER, IN A RECENT NOTE,[1] gave two reasons for the errors in the stability calculations with heat transfer presented by Lees.[2] One of these, the presence of numerical errors, has been acknowledged by Lees[3] and also seems to be implied by Van Driest,[4] who lists differences in Prandtl Number and viscosity law as possible reasons for the discrepancy between his results and the results of Lees. However, the second reason given by the writer, and not mentioned by Lees or Van Driest, is probably more important from the standpoint of the convenient practical application of Lees' analysis in cases involving large amounts of cooling at high Mach Numbers—that is, Lees's assumption that λ [defined in Eq. (15), reference 2] is much smaller than 1. This device for approximately satisfying Eqs. (19) and (20) of reference 2 bears further discussion. As the writer indicates in work to be published by the N.A.C.A., the above assumption is unnecessary and in some instances is incorrect. As an alternative, Eqs. (19) and (20) of reference 2 may be combined to give the following expression:

$$v[1 - (2\Phi_r - 1)\lambda + (\Phi_r^2 + \Phi_i^2)\lambda^2/(1 + \lambda)] = \Phi_i \tag{1}$$

With the values $\Phi_i = 0.580$ and $\Phi_r = 1.48$, corresponding to the minimum critical Reynolds Number, Eq. (1) assumes the form

$$v[1 - 1.96\lambda + 2.53\lambda^2/(1 + \lambda)] = 0.580 \tag{2}$$

This equation replaces Eq. (64) of reference 2 with no further complication and holds for all values of λ. For $\lambda \ll 1$, it is equivalent to Eq. (64) of reference 2. The iteration procedure suggested in connection with Eqs. (28) and (29) of reference 2 is thereby obviated. This iteration, moreover, is often inconvenient when $\lambda \gtrsim 1$, since the second approximation for Φ_i often exceeds 0.580 and, hence, one cannot proceed. Trial-and-error methods may, of course, be applied in this event. Van Driest did not indicate how he dealt with this problem.

The values of λ which will be encountered when large amounts of cooling are required at high Mach Numbers can be judged from the following expression of Appendix C, reference 2:

$$\lambda = (0.332/T_1)(\eta/c) - 1$$

For significant amounts of stabilization, the factor η/c will not vary greatly and is of order one. However, the nondimensionalized surface temperature T_1 may be small in these instances, so that λ may be large.

Some values of λ encountered by the writer are given in Table 1. These values are based on the assumption of a Prandtl Number of 1 and a linear viscosity law.

TABLE 1

Free-Stream Mach number	Ratio of Surface to Free-Stream Absolute Temperature (T_1)		λ
3.1	1.4	Complete stabilization	0.29
4.4	0.93		1.1
5.6	0.11		18
5.7	0.008		240
6	1.0		1.8
6	0.05		43

It may be remarked, in addition, that Figs. 7 and 8 and the tabulations in Appendix C and E (right-hand column) of reference 2 must be corrected. Moreover, in view of Lin's recent observations[5] that the stability theory developed in references 6 and 2 is applicable, in a strict sense, only to cases involving moderately low Mach Numbers, results obtained by using the theory in its present form for higher Mach Numbers should be considered only for possible qualitative trends.

References

[1] Bloom, M., *The Effect of Surface Cooling on Laminar Boundary-Layer Stability*, Readers' Forum, Journal of the Aeronautical Sciences, Vol. 18, No. 9, p. 635, September, 1951.

[2] Lees, L., *The Stability of the Laminar Boundary Layer in a Compressible Fluid*, N.A.C.A. Report No. 876, 1947.

[3] Lees, L., *Comments on the "Effect of Surface Cooling on Laminar Boundary-Layer Stability,"* Readers' Forum, Journal of the Aeronautical Sciences, Vol. 18, No. 12, p. 844, December, 1951.

[4] Van Driest, E. R., *Cooling Required to Stabilize the Laminar Boundary Layer on a Flat Plate*, Readers' Forum, Journal of the Aeronautical Sciences, Vol. 18, No. 10, p. 698, October, 1951.

[5] Lin, C. C., *On the Stability of the Boundary Layer with Respect to Disturbances of Large Wave Velocity*, Readers' Forum, Journal of the Aeronautical Sciences, Vol. 19, No. 2, p. 138, February, 1952.

[6] Lees, L., and Lin, C. C., *Investigation of the Stability of the Laminar Boundary Layer in a Compressible Fluid*, N.A.C.A. T.N. No. 1115, September, 1946.

Services of the Libraries of the Institute of the Aeronautical Sciences

The services of the Libraries are available to all members of the Institute, to Corporate Members, to advertisers in the AERONAUTICAL ENGINEERING REVIEW and AERONAUTICAL ENGINEERING CATALOG, and, under usual library limitations, to the public. Four specialized services are available.

The Paul Kollsman Lending Library

This lending library service makes available, *without charge*, the latest and more important aeronautical books.

Members may request the loan of any aeronautical or technical book they wish to borrow. Through an exchange agreement with the Engineering Societies Library, any book on general engineering may be borrowed from its great collection of over 160,000 volumes.

A photostating service is available at usual library rates.

Applications for membership in the library and further information will be sent on request.

The W. A. M. Burden Reference Library

This reference library contains over 12,000 aeronautical books, magazines, pamphlets, and reports gathered from world-wide sources and is one of the most complete aeronautical libraries in the world. Material from this library is not available for loan but may be used for reference purposes.

The Pacific Aeronautical Library

7660 Beverly Boulevard
Los Angeles 36, California

Established in cooperation with the aircraft companies the library serves. The leading aircraft companies in or near Los Angeles participate in its support and operation.

This service library for aeronautical research is available to the public for reading privileges. Source material includes aerodynamic and structural research reports, as well as books on drafting, production methods, history, and allied sciences. It furnishes books, periodicals, and pamphlet material to the participating aircraft companies to supplement their engineering libraries.

Technical Information Service

This service has experienced personnel under the supervision of trained aeronautical engineers to compile any information desired. The services range from listing specialized reference books to the preparation of exhaustive bibliographies, digesting of reports, and general surveys of any aeronautical subject. Some of the available services are:

Bibliographies on any aeronautical subject.
Reports on any aeronautical subject.
Digests of aeronautical books, papers, periodicals, and references.
Translations.
Engineering investigations of special aeronautical subjects.
Biographies of individuals engaged in aeronautics.
Photostats of any aeronautical or general engineering material.
Microfilms made on special order.
Photographs made from the Institute's photographic collection.
Drawings and tracings made.

In addition to the services mentioned any commission which comes within the scope of the Service will be accepted. Special arrangements may be made for work requiring several weeks or months.

Translators are available for accurate transcriptions of all foreign language data. Translations are carefully edited by trained engineers.

Reproductions of any material in the collections of the Institute may be ordered at standard photostat rates.

INSTITUTE OF THE AERONAUTICAL SCIENCES, INC.

2 EAST 64th STREET, NEW YORK 21, N.Y.